การสังเคราะห์และสมบัติของเพอรอฟสไกด์ $Pr_2Ni_{1-x}M_xO_4$, $Pr_2Ni_{1-x}M_xGa_{0.05}O_4$ และ

$Pr_2Ni_{1-x-0.05}M_xGa_{0.05}O_4$ (M = Cu, Co, Mg, Zn, In และ x = 0.1-0.3)

นางสาวศิรประภา ไทยถาวร

SYNTHESIS AND PROPERTIES OF PEROVSKITE $Pr_2Ni_{1-x}M_xO_4$,

$Pr_2Ni_{1-x}M_xGa_{0.05}O_4$, $Pr_2Ni_{1-x-0.05}M_xGa_{0.05}O_4$ (M = Cu, Co, Mg, Zn, In and x = 0.1-0.3)

Miss Siraprapa Thaitaworn

A Thesis Submitted in Partial Fulfillment of the Requirements

for the Degree of Master of Science Program in Petrochemistry and Polymer Science

Faculty of Science

Chulalongkorn University

Academic Year 2007

501874

Thesis Title	**SYNTHESIS AND PROPERTIES OF PEROVSKITE**
	$Pr_2Ni_{1-x}M_xO_4$, $Pr_2Ni_{1-x}M_xGa_{0.05}O_4$ AND
	$Pr_2Ni_{1-x-0.05}M_xGa_{0.05}O_4$
	(M = Cu, Co, Mg, Zn, In and x = 0.1-0.3)
By	**Miss Siraprapa Thaitaworn**
Field of Study	**Petrochemistry and Polymer Science**
Thesis Advisor	**Assistant Professor Oravan Sanguanruang, Ph.D.**

Accepted by the Faculty of Science, Chulalongkorn University in Partial Fulfillment of the Requirements for the Master's Degree

………………………………………Dean of the Faculty of Science

(Professor Supot Hannongbua, Ph.D.)

THESIS COMMITTEE
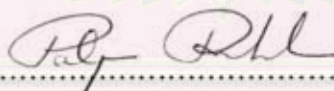
………………………………………Chairman

(Professor Pattarapan Prasassarakich, Ph.D.)

………………………………………Thesis Advisor

(Assistant Professor Oravan Sanguanruang, Ph.D.)

………………………………………Member

(Assistant Professor Soamwadee Chaianansutcharit, Ph.D.)

………………………………………Member

(Assistant Professor Warinthorn Chavasiri, Ph.D.)

ศิรประภา ไทยถาวร : การสังเคราะห์และสมบัติของเพอรอฟสไกต์ $Pr_2Ni_{1-x}M_xO_4$, $Pr_2Ni_{1-x}M_xGa_{0.05}O_4$ และ $Pr_2Ni_{1-x-0.05}M_xGa_{0.05}O_4$ (M = Cu, Co, Mg, Zn, In และ x = 0.1-0.3). (SYNTHESIS AND PROPERTIES OF PEROVSKITES $Pr_2Ni_{1-x}M_xO_4$, $Pr_2Ni_{1-x}M_xGa_{0.05}O_4$ AND $Pr_2Ni_{1-x-0.05}M_xGa_{0.05}O_4$ (M = Cu, Co, Mg, Zn, In and x = 0.1-0.3) อ. ที่ปรึกษา: ผู้ช่วยศาสตราจารย์ ดร. อรวรรณ สงวนเรือง, 126 หน้า.

ศึกษาโครงสร้าง, สัณฐาน ค่าการซึมผ่านออกซิเจนและค่าการนำไฟฟ้าของ $Pr_2Ni_{1-x}M_x$-O_4, $Pr_2Ni_{1-x}M_xGa_{0.05}O_4$ และ $Pr_2Ni_{1-x-0.05}M_xGa_{0.05}O_4$ (M = Cu, Co, Mg, Zn, In และ x = 0.1-0.3) เพื่อหาวัสดุที่มีสมบัติเป็นตัวนำอิเล็กตรอนและไอออนออกไซด์ชนิดใหม่สำหรับประยุกต์ใช้ในเซลล์เชื้อเพลิงของแข็ง ได้สังเคราะห์สารประกอบด้วยวิธีซิเทรตประยุกต์ และตรวจสอบเอกลักษณ์ด้วยเทคนิค XRD และ SEM สารเพอรอฟสไกต์แสดงโครงสร้างเป็นชนิด K_2NiF_4 แบบออโทรอมบิคเพอรอฟสไกต์ มีความเป็นเนื้อเดียวกัน และมีความหนาแน่นสูง ยกเว้น $Pr_2Ni_{1-x}Mg_xO_4$ (x = 0.2, 0.3) และ $Pr_2Ni_{1-x}Co_xGa_{0.05}O_4$, $Pr_2Ni_{1-x-0.05}Co_xGa_{0.05}O_4$ (x = 0.2, 0.3) สมบัติการซึมผ่านของออกซิเจนตรวจสอบโดยใช้เทคนิค TGA และ O_2-TPD พบว่าเมื่อเพิ่มปริมาณโลหะที่เติมตำแหน่ง B แทนที่ Ni มีผลทำให้ค่าการซึมผ่านของออกซิเจนมากขึ้น ยกเว้น $Pr_2Ni_{1-x}In_xO_4$ และค่าซึมผ่านของออกซิเจนสูงมากที่สุดเมื่อเติม Ga แบบสัดส่วนคงที่ ค่าการนำไฟฟ้าได้รับการปรับปรุงเมื่อเติมโลหะ Cu และ Zn โดยเฉพาะอย่างยิ่งเมื่อเติม 15% Cu โดย $Pr_2Ni_{0.85}Cu_{0.15}O_4$ แสดงค่าการนำไฟฟ้า 123.7 $S^{-1}cm^{-1}$ ที่อุณหภูมิ 550°C ซึ่งสูงมากกว่า Pr_2NiO_4(82.5 $S^{-1}cm^{-1}$ at 550°C) ถึง 50% อย่างไรก็ตาม การเติม Ga ที่ตำแหน่ง B ลดค่าการนำไฟฟ้าของเพอรอฟสไกต์

สาขาวิชา ปิโตรเคมีและวิทยาศาสตร์พอลิเมอร์ ลายมือชื่อนิสิต ศิรประภา ไทยถาวร

ปีการศึกษา 2550 ลายมือชื่ออาจารย์ที่ปรึกษา อรวรรณ สงวนเรือง

4872480223: MAJOR PETROCHEMISTRY AND POLYMER SCIENCE
KEY WORD: PEROVSKITE OXIDE/ CATHODE MATERIAL/ OXYGEN PERMEATION/ ELECTRICAL CONDUCTIVITY

SIRAPRAPA THAITAWORN: SYNTHESIS AND PROPERTIES OF PEROVSKITES $Pr_2Ni_{1-x}M_xO_4$, $Pr_2Ni_{1-x}M_xGa_{0.05}O_4$ AND $Pr_2Ni_{1-x-0.05}M_xGa_{0.05}O_4$ (M = Cu, Co, Mg, Zn, In and x = 0.1-0.3). THESIS ADVISOR: ASST. PROF. ORAVAN SANGUANRUANG, Ph.D., 126 pp.

The structure, surface morphology, oxygen property and electrical conductivity of the $Pr_2Ni_{1-x}M_xO_4$, $Pr_2Ni_{1-x}M_xGa_{0.05}O_4$ and $Pr_2Ni_{1-x-0.05}M_xGa_{0.05}O_4$ (M = Cu, Co, In, Mg, Zn and x = 0.1-0.3) were investigated as a new mixed electronic and oxide ionic conductor for materials in Solid Oxide Fuel Cell (SOFC). The compounds were synthesized by modified citrate method and characterized by XRD and SEM. All perovskite showed K_2NiF_4–type with orthorhombic perovskite structure, homogeneous and dense microstructure, except $Pr_2Ni_{1-x}Mg_xO_4$ (x=0.2, 0.3) and $Pr_2Ni_{1-x}Co_xGa_{0.05}O_4$, $Pr_2Ni_{1-x-0.05}Co_xGa_{0.05}O_4$ (x=0.2, 0.3). The effects of Ni-site dopant on oxygen property and electrical properties were studied. Oxygen property was determined by thermogravimetric analysis (TGA) and oxygen temperature-programmed desorption (O_2-TPD). The result showed that the amounts of the oxygen permeation increased with the increasing amount of metal doped at Ni site, except $Pr_2Ni_{1-x}In_xO_4$. Ga–doped $Pr_2Ni_{1-x}M_xO_4$ stoichiometric compositions revealed the highest value of oxygen permeation. The conductivity was improved by doping Cu and Zn. Especially, doping 15% Cu is the most effective for enhancing the electrical conductivity of Pr_2NiO_4. The $Pr_2Ni_{0.85}Cu_{0.15}O_4$ ceramic exhibited an electrical conductivity of 123.7 $S^{-1}cm^{-1}$ at 550°C, which was about 50% higher than that of Pr_2NiO_4 (82.5 $S^{-1}cm^{-1}$ at 550°C). However, Ga–doped at the B site ions decreased the electrical conductivity.

Field of Study: Petrochemistry and Polymer Science Student's Signature: Siraprapa Thaitaworn

Academic year: 2007 Advisor's Signature: Oravan Sanguanruang

ACKNOWLEDGEMENTS

CONTENTS

ศูนย์วิทยทรัพยากร

จุฬาลงกรณ์มหาวิทยาลัย

LIST OF FIGURES

Figure   **Page**

Figure   **Page**

Figure   **Page**

Figure Page

ศูนย์วิทยทรัพยากร
จุฬาลงกรณ์มหาวิทยาลัย

LIST OF SCHEMES

LIST OF TABLES

Table   Page

LIST OF ABBREVIATIONS

SOFC	Solid Oxide Fuel Cell
DMFC	Direct Methanol Fuel Cell
PEMFC	Proton Exchange Membrane Fuel Cell
AFC	Alkaline Fuel Cell
PAFC	Phosphoric Acid Fuel Cell
MCFC	Molten Carbonate Fuel Cell
MIEC	Mixed Ionic Electronic Conductor
EDTA	Ethylene Diamine Tetraacetic Acid
Cit	Citric acid
TEC	Thermal Expansion Coefficients
XRD	X-ray diffractometry
SEM	Scanning Electron Microscopy
TGA	Thermogravimetric analysis
TPD	Temperature-Programmed Desorption
$°C$	degree Celsius
ml	milliliter (s)
g	gram (s)
h	hour (s)
mg	milligram (s)
min	minute (s)
$Å$	Angstrom
%	percent
r	Ionic radius
t	Tolerance factor
σ	Specific conductivity

CHAPTER I

INTRODUCTION

1.1 Background

The efficient and environmentally friendly production of energy and chemicals is a long sought goal for the development of energy technologies and chemical reactors that will contribute to a sustainable development. At the forefront of these technologies is the solid oxide fuel cells (SOFC) which is hoped to find widespread application in the direct conversion of chemical energy into electricity with high thermodynamic efficiency and minimal environmental pollution [1]. Solid oxide fuel cells (SOFC) have been targeted for both mobile and stationary power-generation systems. Solid oxide fuel cells (SOFC) are promising candidates' for high efficiency energy production in the near future. Indeed, the advantages of SOFC are as consequence of: (i) the high operating temperature (600–900 °C), allowing the use of non-precious metal electrocatalysts, heat recovery and the superior ionic conductivity of the different components; (ii) the fact that the cell consists of assembled solid ceramic components; (iii) high energy conversion efficiency (iv) no emission of pollutant by CO (v) high stability (vi) flexibility in fuel [2]. Solid oxide fuel cells have so far been operated on methane, propane, butane, fermentation gas, gasified biomass and paint fumes. Nevertheless, the current SOFC technology suffers from two main drawbacks that must be overcome before up-scaling and launch to the market: (i) the high price of the produced kWh due to the manufacturing costs; and (ii) the high operating temperature (>750 °C), which increases the costs of construction materials and the starting-up time, shortens the operating life of the fuel cell stack, and therefore decreases the scope for domestic and vehicle power generation applications [2] However, selection of the optimal electrode, electrolyte, interconnect, and contact materials for SOFC remains open [3].

1.1.1 Fuel cells

Fuel cells are electrochemical devices that convert the chemical energy stored in a fuel directly into electrical power. The basic physical structure or building block of a fuel cell consists of an electrolyte layer in contact with a porous anode and a cathode on either side. The main attractive features of fuel cell systems are also flexibility in sizing, quiet operation and near zero emissions. These benign features render the fuel cells as prime candidates for providing local or national wide power systems for a sustainable economy while maintaining a clean environment. Fuel cells promise to replace the internal combustion engine in transportation due to their higher efficiency, low emissions depending on fuel cell types, and to replace batteries for portable electronics due to their higher energy density and zero recharge time [1]. The most common classification of fuel cells is by the type of electrolyte used in the cells, operating temperatures, and the mechanism by which charge is conducted in it:

(1) Direct methanol fuel cell (DMFC), ~60 °C;

(2) Proton exchange membrane fuel cell (PEMFC), ~80 °C;

(3) Alkaline fuel cell (AFC), ~100 °C;

(4) Phosphoric acid fuel cell (PAFC), ~200 °C;

(5) Molten carbonate fuel cell (MCFC), ~650 °C;

(6) Solid oxide fuel cell (SOFC), ~650-1000 °C.

A schematic diagram of a planar SOFC single cell structure is shown in Figure 1.1.
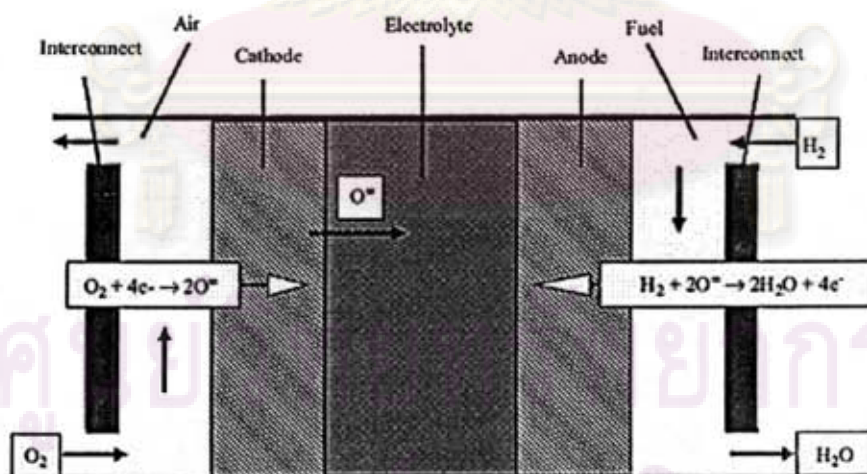
Figure 1.1 Planar SOFC single structures.

1.1.2 SOFC materials

The electrolyte of SOFC is a solid, nonporous ceramic, usually Y_2O_3-stabilized ZrO_2 (YSZ). The SOFC operates at 600–1000 °C where the ceramic electrolyte becomes conductive to oxygen ions, O^{2-}, but nonconductive to electrons. In 1899, Nernst discovered the solid oxide electrolyte when using stabilized zirconia in making filaments for electric glowers. Nernst is the first scientist describing zirconia (ZrO_2) as an oxygen ion conductor. Until lately, SOFC have all been developed based on an electrolyte of zirconia stabilized with the addition of a small percentage of yttria (Y_2O_3). The range of the operating temperature of the SOFC is the highest operating temperature range of all fuel cells, which presents both challenges for the construction of durable SOFC, and advantages. The high operating temperature permits rapid kinetics and allows production of high quality heat as by-product suitable for co-generation.

SOFC cathodes are now made primarily from electronically conducting oxides or mixed electronically conducting and ion-conducting ceramics. Typically, the anode is made of nickel/yttria-stabilized zirconia (Ni/YSZ) cermet and the cathode is Sr-doped $LaMnO_3$. Until recently, nickel is used as an internal reforming catalyst and it is possible to carry out internal reforming in the SOFC directly on the Ni anode. At high temperatures, the ceramic electrolyte ionic conductivity increases and the electrochemical reactions are accelerated. The SOFC can be operated with simpler concepts because there are only two phases, gas and solid, are involved. Ceramic materials are inorganic, nonmetallic materials which consist of metallic and nonmetallic elements bonded together primarily by ionic and/or covalent bonds. Ceramic materials properties vary greatly due to differences in nature of intermolecular bonding. Most oxides are ceramics. Metal oxide structures are formed on the basis of nearly close-packed oxygen ions, and cations placed in available interstices. Because ceramic materials are vulnerable to mechanical impacts and thermal shocks, there are significant restrictions on the cell designs. Thermal expansion mismatch between different ceramic components and sealing difficulties are major concerns of SOFC design and fabrication. Modeling of SOFC will help optimize the design and mitigate the problems [1].

Table 1.1 Properties of perovskites in components

components	properties
Cathode	(1) High ionic-electronic conductivity
	(2) High catalytic activity for oxygen molecule dissociation and oxygen reduction
	(3) Thermal expansion compatible with SOFC electrolyte
Electrolyte	(1) High ion conductivity (O_2^- ions)
	(2) Good chemical compatibility
	(3) Excellent mechanical properties
Anode	(1) High electronic conductivity
	(2) High catalytic activity of Ni promotes cracking of hydrocarbon

1.1.3 Operation of SOFC
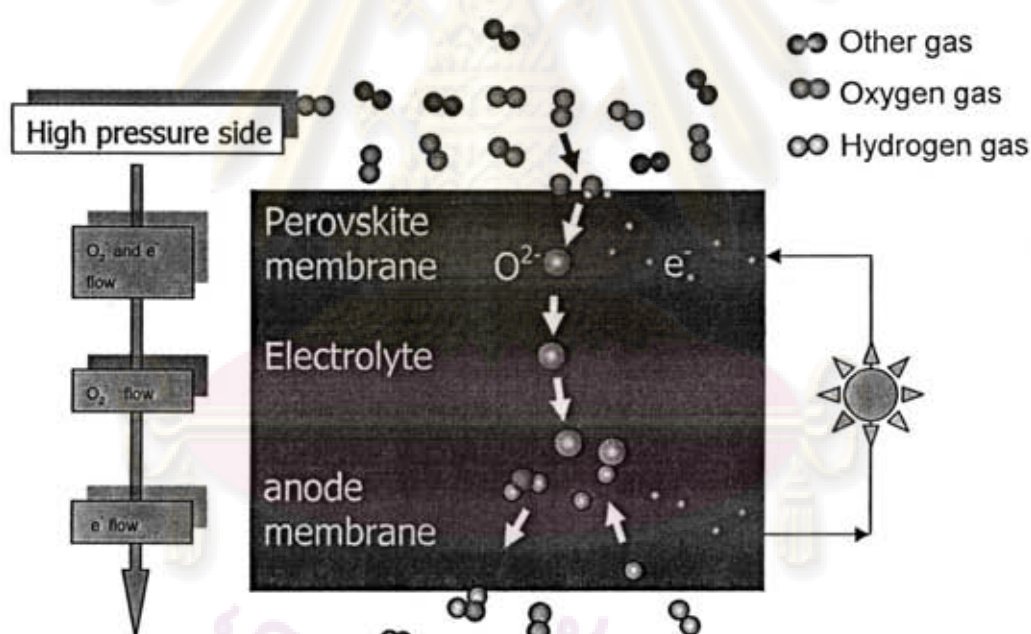
Figure 1.2 operation of SOFC

At the cathode, the oxygen molecules from the air are split into oxygen ions with the addition of four electrons. The oxygen ions are conducted through the electrolyte and

combine with hydrogen at the anode, releasing four electrons. The electrons travel an external circuit providing electric power and producing by–product heat.

Anode Reaction:	$2 H_2 + 2 O^{2-} \Rightarrow 2 H_2O + 4 e^-$
Cathode Reaction:	$O_2 + 4 e^- \Rightarrow 2 O_2^-$
Overall Cell Reaction:	$2 H_2 + O_2 \Rightarrow 2 H_2O$

The operating efficiency in generating electricity is among the highest of the fuel cells at about 60%. Furthermore, the high operating temperature allows cogeneration applications to create high-pressure steam that can be used in many applications. Combining a high–temperature fuel cell with a turbine into a hybrid fuel cell further increases the overall efficiency of generating electricity with a potential of an efficiency of more than 70%.

1.1.4 Fuel flexibility of SOFC

SOFC are more flexible for the use of fuels than low temperature fuel cells. In the SOFC, not only hydrogen but also several hydrocarbons and carbon monoxide (CO) can be used as fuels. When using hydrogen fuel, the electrochemical reactions of the SOFC:

At the anode of SOFC

$$H_2 + 2O_2^- \rightarrow 2H_2O + 4e^- \tag{1.1}$$

At the cathode

$$O_2 + 4e^- \rightarrow 2O_2^- \tag{1.2}$$

The overall cell reaction is

$$O_2 + 2H_2 \rightarrow 2H_2O \tag{1.3}$$

When using carbon monoxide fuel, the electrochemical reactions of the SOFC:

At the anode of SOFC

$$CO + 2O_2- \rightarrow 2CO_2 + 4e^- \tag{1.4}$$

At the cathode

$$O_2 + 4e^- \rightarrow 2O_2^- \tag{1.2}$$

The overall cell reaction is

$$CO + O_2 \rightarrow 2CO_2 \tag{1.5}$$

At high temperature, carbon monoxide can be oxidized with water to form carbon dioxide and hydrogen gas as the water–gas shift reaction

$$CO + H_2O \rightarrow CO_2 + H_2 \qquad (1.6)$$

When using methane as fuel, the electrochemical reactions of the SOFC:

At the anode of SOFC

$$CH_4 + 4O_2^- \rightarrow CO_2 + 2H_2O + 8e^- \qquad (1.7)$$

At the cathode

$$2O_2 + 8e^- \rightarrow 4O_2^- \qquad (1.8)$$

The overall cell reaction is

$$CH_4 + 2O_2 \rightarrow CO_2 + 2H_2O \qquad (1.9)$$
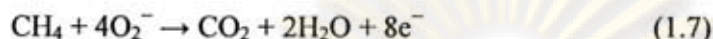
In practice, the methane-reforming reaction is normally used instead of the direct electrochemical methane-combusting reaction Eq. (1.9). The methane-reforming reaction usually considered as

$$CH_4 + H_2O \rightarrow 3H_2 + CO \qquad (1.10)$$

When using hydrocarbon ($C_nH_mO_p$) as fuels, the electrochemical reactions of the SOFC:

At the anode of SOFC

$$C_nH_m + (2n + 0.5m)O_2^- \rightarrow nCO_2 + (0.5m)H_2O + (4n + m)e^- \; ; p = 2n + 0.5m \qquad (1.11)$$

At the cathode:

$$(n + 0.25m)O_2 + (4n + m)e^- \rightarrow (2n + 0.5m)O_2^- \qquad (1.12)$$

The overall cell reaction is

$$C_nH_m + (n + 0.25m)O_2 \rightarrow nCO_2 + (0.5m)H_2O \qquad (1.13)$$
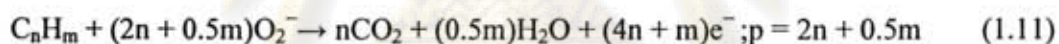
The hydrocarbon-reforming reaction can be described as

$$C_nH_m + nH_2O \rightarrow (n + 0.5m)H_2 + nCO \qquad (1.14)$$
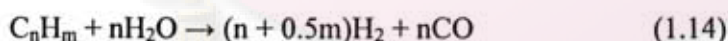
Perovskite–like oxides have been the most widely studied as cathodes for SOFC applications, however these materials do not fulfill all the technological requirements for the adequate performance of SOFC systems. This has led to an increasing interest in the search for new mixed conductors, where K_2NiF_4 structures have called considerable attention [4].

1.1.5 Perovskite

Mixed ionic electronic conductors (MIEC) exhibiting both electronic and ionic conductivities have a wide range of utilization such as fuel cells. Some perovskite oxides are found to be good mixed-conducting materials. Perovskites are a large family of crystalline ceramics that derive their name from a specific mineral known as perovskite. They are the most abundant minerals on earth and have been of continuing interest to geologists for the clues they hold to the planet's history. The parent material, perovskite, was first described in the 1830's by the geologist Gustav Rose, who named it after the famous Russian mineralogist Count Lev Aleksevich von Perovski. There are many perovskite compound types, each have various properties that are used in different applications such as insulators, dielectrics, magnetic materials, ionic conductors, mixed conductors, and superconductors. This study is focused on the use of mixed conducting perovskites as SOFC. The Ruddlesden–Popper-type phase, $R_2NiO_{4+\delta}$ (R=Pr), as a mixed electronic and oxide-ion conductor (MIEC) in an oxidizing atmosphere, is explored as the SOFC cathode material in this thesis [3].

1.1.6 Crystal structure

M. Al Daroukh and et al. studied the structural of A_2MO_{4-x} oxides compared with the characteristics of perovskite-type oxides AMO_{3-x} containing the same cations [5]. In ABO_3 perovskite structure, where A is the larger cation in a twelvefold coordination, and B is the smaller cation in the sixfold coordination with oxygen ions. The B ions can take a mixed-valence state such as transition metals.
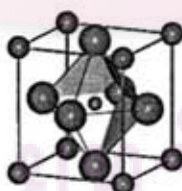
Figure 1.3 ABO_3 perovskite structure.

The partial substitution of cations in the ABO_3 perovskite structure by cations with a lower valence either leads to formation of oxygen vacancies or to charge

compensation by electronic charge carriers. The ratio of the ionic to electronic conductivity may vary markedly and in a complex manner with temperature, oxygen activity and dopants. The nature and extent of oxygen nonstoichiometry greatly affects the level of ionic conductivity, requiring judicious choice of the substituting ions. Large numbers of disordered oxygen vacancies at elevated temperatures may lead to the onset of high ionic conductivity. There are many investigations on the composition–property relationship of AMO_3-type oxides with A= Ln (lanthanides), Ca, Sr, Ba; M= Cr, Mn, Fe, Co, Ni, Ga, In, with mixed occupation of the A- and M-sublattices.

The structure of the Ruddlesden–Popper-type phase $A_2MO_{4+\delta}$ is shown in Figure 1.4.
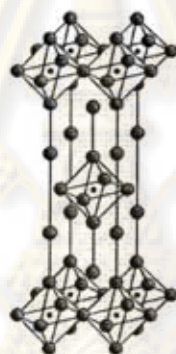
Figure 1.4 A_2BO_4 perovskite structure.

A_2BO_4 oxides with the perovskite-related K_2NiF_4- type structure are less intensively investigated. Recent results on lanthanum cobaltites and nickelates indicated enhanced chemical stability and moderate thermal expansion. Compounds with formula A_2BO_4 generally have the tetragonal K_2NiF_4 structure when the radius of the A cation is $1.0 < r_A < 1.9$ A°, the radius of the B cation is $0.5 < r_B < 1.2$ A°. The larger A cation has nine-fold coordination and the smaller B cation has octahedral coordination. This structure can be described as containing alternate layering of perovskite (ABO_3) and rock-salt (AO) units [6]. It contains δ excess interstitial oxygen defects (O_i'' ions) per formula unit located between the paired AO rocksalt bilayers that alternate with the ABO_3 layers [3]. These oxides (A_2BO_4), as well as perovskite (ABO_3), have a well-defined bulk structure and the composition of cations at both A and B sites can be variously changed without destroying the matrix

structure, they therefore can be very useful as model systems to investigate the relationships between solid-state properties and catalytic performance of catalyst.

Corresponding to the thermodynamic stabilities of the oxides within the range of phase stability, the oxide AMO_3 undergoes a partial reduction/oxidation reaction resulting in the well-known oxygen vacancy and electron hole-type defect structure, which determines the electrical transport properties of the oxides.

$$AMO_3 = AMO_{3-x} + x/2O_2 \qquad (1.15)$$

At higher temperatures and lower oxygen partial pressures, the AMO_3 phase becomes unstable and reacts to form A_2MO_4:

$$2AMO_3 = A_2MO_4 + MO + 1/2O_2 \qquad (1.16)$$
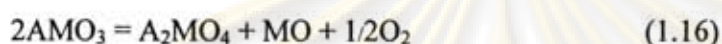
Reaction (1.16) can be assumed as a proof of the higher thermochemical stability of the A_2MO_4-type compounds compared with the AMO_3-type oxides. A_2MO_4-type oxides undergo partial reduction/oxidation reactions as well, corresponding to their thermodynamic stabilities within the range of existence of the phase.

$$A_2MO_4 = A_2MO_{4\pm x} \pm x/2O_2 \qquad (1.17)$$

The regular oxygen sites within the K_2NiF_4-type structure are completely occupied at an oxygen stoichiometry of 4.0. In compositions with A+A'>1 excess oxygen ions may occupy interstitial oxygen sites as demonstrated by structure investigations. The perovskite and the K_2NiF_4-type oxide phases are characterized by a range of existence expressed by the O/M stoichiometry range (3-x) and (4-x), respectively. Therefore, one fixed value for the free energy, $\Delta G°$, does not exist. Within the range of existence of the phases, the value x of reversible oxygen exchange according to reactions (1.15) and (1.17) is used as an expression for the thermodynamic stability.

$$x = f(T, pO_2) \qquad (1.18)$$
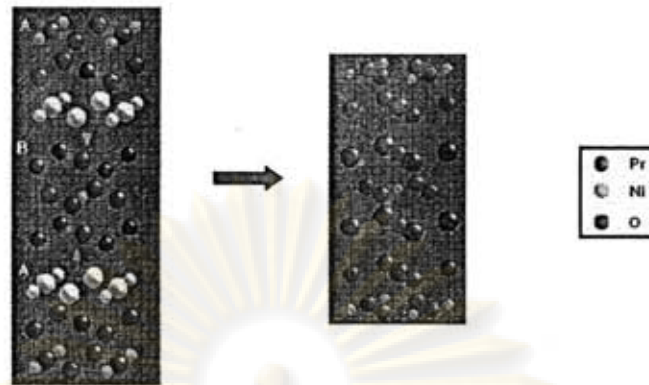
Figure 1.5 show AMO$_3$ phase reacts to A$_2$MO$_4$

1.1.7 Tolerance factors in perovskites

The formation of perovskite-oxides with high oxygen ionic conductivity requires high oxygen vacancy concentrations created by dopants, and best conditions for oxygen mobility. The ionic radii of the dopants must be fitted to the lattice, while is expressed by the Goldschmidt tolerance factor: Besides the stability of the perovskite structure has often been rationalized in terms of a parameter, termed Goldschmidt tolerance factor, t, which is based on the ionic radii of the ions comprising the unit cell defined as [7]:

$$t = \frac{(r_A + r_O)}{\sqrt{2}(r_B + r_O)}$$

Where, r_A, r_B, and r_O are the ionic radii of A, B and O ions, respectively. Where the atoms are touching one another, the B-O distance is equal to a/2 (a is the cubic unit cell parameter) while the A-O distance is (a/$\sqrt{2}$) and the following relationship between the ionic radius (r) holds: $r_A + r_O = \sqrt{2}$ ($r_B + r_O$).

ศูนย์วิทยทรัพยากร

จุฬาลงกรณ์มหาวิทยาลัย
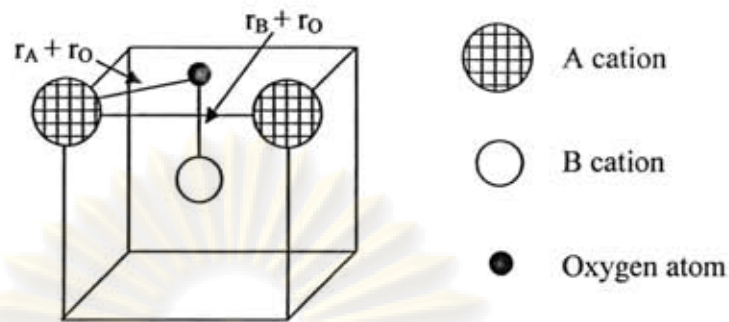
Figure 1.6 The relationship between symmetry and ionic radii in the perovskite.

The ideal perovskite is the cubic structure with the tolerance factor close to 1.0 at high temperature. The perovskite structure is stable in the range $0.75 < t < 1.0$, and is cubic in the range $t > 0.95$. However, it seems that $t = 0.75$-1.00 is a necessary but not a sufficient condition for the formation of the perovskite structure. Even in the range of $t = 0.8$-0.9 which is the most favourable value for perovskites. Deviations from the ideal structure are well known as orthorhombic, rhombohedral, tetragonal, monoclinic and triclinic symmetry. The closer the t is to unity, the greater is the stability of the perovskite structure, whereas greater declinations from unity give distorted unit cells. Yokokawa [8-9] observed a strong correlation between the formation of perovskite phases from oxides and the Goldschmidt numbers. Thermodynamic stability increases with increasing Goldschmidt number. This correlation helps to establish doping strategies, calculating with mean ionic radii in the case of doping. For example, $BaTiO_3$ has a tolerance factor over 0.97 and it is stable over a wide temperature range. $BaCeO_3$, on the other hand, has a tolerance factor of ~0.89, and is unstable at low temperatures [7]. The distorted structure may exist at room temperature but it transforms to the cubic structure at ambient temperature.

Wan et al [3]. studied the performance of $Nd_{2-x}La_xNiO_{4+\delta}$ as a cathode material for solid oxide fuel cell (SOFC). Because of $La_2NiO_{4+\delta}$ started to lose interstitial oxygen above 430 °C. This loss introduced unacceptable volume changes and a reduction of the oxygen- ion conductivity, which is clearly a problem for applications such as the cathode of SOFC operating at about 800 °C. The introduction of the O_i'' ions is driven by a mismatch in the equilibrium (R–O) and (Ni–O) bond lengths, i.e. by a geometric tolerance factor $t \equiv (R–O)/\sqrt{2}(Ni–O) < 1$. The interstitial ions

O_i'' are expected to relieve the compressive stress on the NiO_2 layers. By increasing this mismatch (i.e. lowering t) via substitution of a smaller Nd^{3+} ion for La^{3+}, it might be possible to retain the interstitial oxygen to higher temperatures in $Nd_2NiO_{4+\delta}$. Substitution of smaller Nd^{3+} ion for La^{3+} in $La_2NiO_{4+\delta}$ increased the retention of mobile interstitial oxygen defects (O_i'' ions). The concentration of the O_i'' ions in $Nd_2NiO_{4+\delta}$ was stabilized at $\delta\approx0.12$ at 800 °C in air after thermal cycling. Deposition of $Nd_2NiO_{4+\delta}$ directly onto an LSGM electrolyte gave poor performance presumably due to the interdiffusion of La^{3+} and Nd^{3+} ions across the electrolyte/cathode interface and subsequent formation of ion-blocking phases at the interface. Insertion of an LDC interlayer between $Nd_2NiO_{4+\delta}$ and LSGM and/or Pt sputtering on the $Nd_2NiO_{4+\delta}$ surface significantly decreased the cathode overpotential. $La_{1.2}Nd_{0.8}NiO_{4+\delta}$ on LSGM provided isoactivity of the La^{3+} ions at the interface, and this cathode composition gave a remarkable improvement in the cell performance.

1.1.8 Nonstoichiometry in perovskites

It is intended to explore the relevant properties for application as SOFC cathodes with A_2BO_4 structure and with or without A– and B–site cation nonstoichiometry in respect of electrical conductivity, thermal expansion and stability, ionic compatibility with other cell components. It is well known that cationic nonstoichiometry has effects on defect structure, transport properties, and catalytic activity of perovskites with ABO_3 structure; hence it can be assumed that the cation nonstochiometry of A_2BO_4 materials may also play an important role.

Nonstoichiometry in perovskites can arise from cation deficiency (in the A or B site), anion deficiency, or anion excess. For the cation deficiency, A–site cations can be missing without collapse of the perovskite network because of the stability of the BO_3 group. On the contrary, B–site vacancies are not energetically favored because of the large formal charge and the small size of the B cations in perovskites. Nevertheless, an oxygen vacancy in perovskites is more common than a cation deficiency.

Many oxygen–deficient perovskites can be described on the basis of complex perovskite–related super–structures of general formula $A_nB_nO_{3n-1}$, in which the stacking manner depends on the size, electronic configurations, and coordination

numbers of A and B cations. Oxygen vacancies are accomplished by substituting ions of similar size but different valence. For example, some of the La^{3+} ions in $LaBO_3$ are replaced by Sr^{2+} to form $La_{1-x}Sr_xBO_{3-\delta}$, and therefore, oxygen vacancies are formed. The former composition can be considered as an anion-deficient perovskite with one-sixth of the oxygen ions being vacant. Oxygen vacancies are ordered in alternate [001] BO_2 planes of the cubic structure such that alternate [110] rows of oxide anions are missing.

1.1.8.1 Physical properties

The perovskite structure class is one of the most commonly occurring and important in all of materials science. Physical properties of interest among perovskites include superconductivity, colossal magnetoresistance, ionic conductivity, and a multitude of dielectric properties, which are of great importance in microelectronics and telecommunication. Because of the great flexibility inherent in the perovskite structure there are many different types of distortions which can occur from the ideal structure. These include tilting of the octahedra, displacements of the cations out of the centers of their coordination polyhedra, and distortions of the octahedra driven by electronic factors (i.e. Jahn-Teller distortions). Many of the physical properties of perovskites depend crucially on the details of these distortions, particularly the electronic, magnetic and dielectric properties which are so important for many of the applications of perovskite materials.

1.1.8.2 Magnetic properties

In the ideal cubic perovskite structure, each atom of oxygen is shared by two B^{3+} ions, forming a B-O-B angle of $180°$. Such a configuration is favorable for super exchange interactions between magnetic B^{3+} cations. This exchange usually results in anti-parallel coupling of nearest-neighbor magnetic moments. When the B^{3+} ions are in two sub lattices ($A_2BB'O_6$) the other spin arrangements are possible. If B' is a diamagnetic ion, the B^{3+} ions are aligned anti-ferromagnetic, and the most important exchange mechanism is believed to be a longer range super exchange interaction through two oxygens of the type B-O-B'-O-B. The B-B separation is now considerably longer than the 0.4 nm separation found in the ideal perovskite. The

LnFeO$_3$ (Ln = lanthanide) perovskites are those that have attracted the most attention because of their possible applications as technological magnetic materials [10]. These compounds show a weak spontaneous magnetic moment, which is attributed to a slight canting of the iron moments, which are otherwise anti-ferromagnetic aligned. Similarly, LnMnO$_3$ shows very interesting magnetic properties. These manganites containing mostly Mn^{3+} or Mn^{4+} ions show anti-ferromagnetic behavior. However, ferromagnetic behavior is observed in the range from 25 to 35% Mn^{4+}. A weak magnetic interaction was found between Mn^{3+} ions, together with a negative interaction between Mn^{4+} ions and a strong positive interaction between Mn^{3+} and Mn^{4+}. A similar kind of behavior was found for the combination of Co^{3+} and Co^{4+}, but the Cr and Fe compounds were found to be anti-ferromagnetic.

1.1.8.3 Mixed ionic-electronic conductors

Perovskite oxide exhibits both ionic and electronic conductivity. It may show both high oxygen ion conductivity due to the high oxygen vacancy concentration, and a high electronic conductivity due to the mixed-valence state [11]. The B ions can take a mixed-valence state, charge neutrality is maintained by both the formations of oxygen vacancies and a change in the valence state of the B ions. The B-site ion substitution can increase the concentration of oxygen vacancies, such as Cu and Ni ions, which naturally take the divalent oxidation state [12]. If the valence state of the B ions is fixed, neutrality is maintained only by the formation of oxygen vacancies. The oxides may be predominantly ionic conductors, in this case.

In order to characterize the materials, it is more often to measure their electronic and ionic conductivity instead of concentrations of electrons (holes) and mobile ions (vacancies). The calculated ionic and electronic conductivity, which were separately, measured by using 4-probe ionic direct current and ordinary 4-probe direct current techniques, respectively.

In all materials that there are in principle nonzero electronic and ionic conductivity, the overall electrical conductivity σ_{tot} is the sum of electronic conductivity σe and ionic conductivity σ_i, as Equation (1.19),

$$\sigma_{tot} = \Sigma \, \sigma_{ij} + \sigma_e \qquad\qquad (1.19)$$

where σ_{ij} is the partial conductivity (in $\Omega^{-1}cm^{-1}$) of the *jth*-type ionic charge carriers presenting in the solid. . Ionic charge carriers can be either atomic in nature or normally defects of either the anionic or cationic sublattice. Ionic conductivity occurs normally via interstitial sites or by hopping into a vacant site (vacancy motion) or a more complex combination based on interstitial and vacant sites.

Electronic (electron/hole) conductivity occurs via delocalized states in the conduction-valence band or via localized states by a thermally assisted hopping mechanism. The presence of electronic conduction in perovskites proceeds via B.

Lattice cations through overlapping B-O-B bonds via a mechanism known as the Zerner double exchange process is shown in Equation (1.20) [13]:

$$B^{n+}\text{-}O^{2-}\text{-}B^{(n+1)} \longrightarrow B^{(n+1)+}\text{-}O^{2-}\text{-}B^{(n+1)+} \longrightarrow B^{(n+1)+}\text{-}O^{2-}\text{-}B^{n+} \qquad (1.20)$$
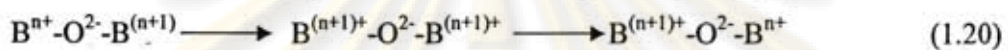
This process is facilited by strong overlap of the B site cation and O_2^- orbital which is maximized for B-O-B angles at 180 °C, i.e., cubic structure. In the orthorhombic structure, the tilting of BO_6 give rise to a decrease in the B-O-B overlap and thus would be expected to provide a larger barrier to electronic conduction. In the above double exchange mechanism, electronic conduction requires the presence of B site cations with multiple valences.

Furthermore, the electronic conduction can be n-type or p-type, depending on the material properties and ambient oxygen partial pressure. The energy level shifts from the center of the energy gap toward the empty zone for an n-type semiconductor or the filled band for a p-type semiconductor. An n-type conductor is an electron conductor while a p-type conductor is an electron hole conductor [14].

1.1.8.4 Electrical properties

The electrical conductivity of perovskites also shows wide variations. Several compounds have been used for their dielectric properties, while others show metallic conductivity, although most are semiconductors. As for other compounds, the electrical behavior in perovskites depends on the outermost electrons, which may be localized at specific atomic sites or may be collective. Since localized electrons may carry a spontaneous moment, there is a strong correlation between the electrical and magnetic properties of perovskites. Rare-earth perovskites containing transition ions show widely differing electrical properties. The electrical properties of perovskites

have aroused special interest since the discovery in 1986 of superconductivity at 40 K in cuprates. These cuprates are whole superconductors, exhibiting a mixed valence of copper Cu^{2+}–Cu^{3+}. Among these, the exception is Ce–doped Nd_2CuO_4, with Tc close to 25 K, which belongs to a different structural type and is an electron superconductor. All these compounds have a common feature, the two-dimensional character of the structure, which has been shown to be an important factor for the existence of superconductivity at high temperature [15].

1.1.9 Oxygen adsorption property

Oxygen adsorption on perovskite oxides has been studied mainly because of these compounds as redox catalysts. They were used for redox reactions in connection with purification of automobile exhaust gases [16]. Thus the study by temperature-programmed desorption (TPD) of oxygen adsorption on perovskite oxides has attracted considerable interest.

Yamazoe et al. [17] reported the first oxygen TPD results from perovskites. The objective was to study the influence of partial substitution of La^{3+} by Sr^{2+} in $La_{1-x}Sr_xCoO_3$ oxides on their surface and catalytic properties. Oxygen TPD peaks from perovskites appeared two oxygen desorption peaks after adsorption on $La_{1-x}Sr_xCoO_3$ at 1023 K. The low-temperature peak (α-type) was attributed to adsorbed oxygen, whereas the high- temperature peak (β-type) was ascribed to lattice oxygen. They concluded that the amount of desorbed oxygen from $La_{1-x}Sr_xCoO_3$ increased with increasing x-substitution. Since A-site substitution with a divalent ion is known to induce the formation of oxygen vacancies.

In a recent contribution, Yokoi and Uchida [18] observed that the amount of O_2 desorbed and the temperature of the α-type oxygen desorption from $LaMO_3$ (M = Cr, Mn, Fe, Co, Ni) tended to decreased with the increasing atomic number of the transition metal. The β-type oxygen desorption peak was found to be more specially associated with the M cation, although it is also affected by La-site substitution.

In 1996, Zhen Zhao, et al. [19] investigated the oxygen TPD of the single-phase catalysts $LaNiO_3$, La_2NiO_4, and $LaSrNiO_4$. For La_2NiO_4 there exists only one desorption peak (α) of oxygen which could be attributed to the ordinarily chemically adsorbed oxygen (O_2^-). For $LaNiO_3$, there appear two desorption peaks (α,β) of

oxygen. The β-type peak was attributed to the lattice oxygen, namely, the oxygen that is released by the reduction of Ni^{3+} according to the following reaction:

$2Ni^{3+} + O^{2-} \rightarrow 2Ni^{2+} + V_0 + 1/2O_2$. Yet for $LaSrNiO_4$, there exists three desorption peaks (α, α', β) of oxygen in the O_2-TPD spectrum. The attributions of α and β are the same as that for $LaNiO_3$, while α' corresponds to the desorption of the oxygen chemically adsorbed on the oxygen vacancies. Therefore, the order of the mobility of lattice oxygen could be given below: $LaSrNiO_4 > LaNiO_3 > La_2NiO_4$. Although, there exist a little oxygen vacancies in the sample $LaNiO_3$ (*ABO$_3$*), no α' desorption peak appeared. It may be suggested that the type of oxygen vacancy in $LaNiO_3$ is different from that in $LaSrNiO_4$ (*A$_2$BO$_4$*). The ordered oxygen vacancies have been found in $LaNiO_3$ perovskite-type oxide. The oxygen vacancies produced by the substitution of La with Sr in $LaSrNiO_4$ seem to be disordered.

Junjiang Zhu, et al. [20] studied the $La_{2-x}Sr_xCuO_4$ ($x = 0.0, 0.5, 1.0$) catalysts for NO+CO reaction. In O_2-TPD experiment, the desorption area of β oxygen, which was contributed by the oxygen adsorbed on the oxygen vacancy, increased with the increase of Sr content and was in the same order as the activity, indicating that the activity depended largely on the oxygen vacancy resulted by Sr addition.

1.1.10 Perovskite synthesis

The procedure for preparing perovskite type membranes consists of three steps: powder synthesis, shaping and sintering. Powder synthesis, as the first step, plays a critical role in determining the particle size of perovskite powder, and consequently has an influence on the microstructure of perovskite membrane. There are many routes to synthesize perovskite, such as a conventional solid–state reaction method and a wet chemical process that includes thermal decomposition of cyanide, metal–EDTA, chemical co precipitation and the sol-gel process etc.

1.1.10.1 Gas phase reaction

The deposition of perovskite films with a specific thickness and composition generally requires gas phase reaction or transport. Many physical techniques have been developed for gas phase deposition such laser ablation, dc

sputtering, magnetron sputtering, electron beam evaporation, thermal evaporation and spray–pyrolysis.

In general, they can be divided into two categories based on the target they use. The first type uses separate targets where a different speed of deposition for each element has to be determined. The second method uses the performed perovskite material itself as target and the stoichiometric phase is transported to the substrate by sputtering or ablation techniques. Gas depositions can be divided further into three categories: (1) deposition at low substrate temperature followed by a post-annealing at elevated temperatures, (2) deposition at intermediate temperature of 873 to 1073 K, and (3) deposition at crystallization temperature under an appropriate atmosphere.

1.1.10.2 Solution reaction

Solution preparation of perovskite materials generally involves the use of metalloorganic compounds that are dissolved in a common solvent. General ways of making perovskite materials usually adopt mixing the constituent oxides, hydroxides and carbonates. These materials generally have a large particle size. The selection strategy of this approach frequently requires repeated mixing and extended heating at high temperature to generate a homogeneous and single-phase material. In order to overcome the disadvantages of low surface area and limited control of the micro-structure inherent in the high temperature process, precursors generated by sol-gel preparations or co precipitation of metal ions by precipitating agents such as hydroxide, cyanide, oxalate, carbonate, citrate ions etc., have been used.

These gel or coprecipitated precursors can offer molecular or near molecular mixing and provide a reactive environment during the course of subsequent heating and decomposition. Because of the improved solid-state diffusion resulting from the improved mixing, they need a relatively lower temperature to produce similar materials compared to the traditional methods. These methods frequently offer additional advantages, such as atomic/molecular level homogenous mixing of constituent metal ions, better reactivity at lower reaction temperatures, high purity, and good control of stoichiometry and high sinter ability.

In 2003, Li, et al. [21] investigated a mixed-conducting complex oxide $La_2NiO_{4+\delta}$ were prepared by complex sol–gel method. Both ethylene diamine

tetraacetic acid (EDTA) and citric acid (Cit) were used as ligands. A dense supported membrane of $La_2NiO_{4+\delta}$ was fabricated by coating the sol on a porous α-Al_2O_3 substrate and followed by heat treatment. A single-phase $La_2NiO_{4+\delta}$ membrane was obtained at 1123 K which is much lower than the temperature needed for conventional solid-state synthesis. The thickness of the membrane is about 40 μm measured by weight method, and there is no crack detectable by gas chromatography. X-ray diffraction (XRD) and IR spectrometry verify the presence of K_2NiF_4-type structure. δ is experimentally determined to be 0.15–0.19. The oxygen flux of the supported membrane, measured by the steady-state method, is not less than 0.3 ml cm^{-2} min^{-1} at 923 K, which is significantly higher than that of the bulk membrane made from by particle sintering similar material, showing its great potential for the application in both air separation and catalytic membrane reactor.

The solution route used will also determine the extent of intermixing of the metal species, whether formation of a network versus formation of individual inorganic phases occurs, the temperature of pyrolysis of organic species occurs, the weight loss associated with oxide formation, the densification and crystallization behavior of obtained metal oxide.

A more subtle concern is the choice of the presumably inert anions, which will be determined by the pH values, ionic strength, degree of super saturation and impurities. This is important firstly because of the tendency of these ions to become incorporated in the final product and secondly because there are subsequent effects can vary dramatically. Conditions that favor large particle size, slow growth and equilibrium will generally produce the purest precipitate.

The advantages of the solution reaction methods, such as better control the stoichiometry and purity, greater flexibility in from thin films and new compositions, an easily generated porous, and an enhanced ability to control particle size.

1.1.10.3 Solid-state reaction

The most common procedure for perovskite oxides synthesis via solid state reactions is the calcination of a homogenous mixture of the corresponding metal–carbonates, hydroxides, and oxides. This is also known as ball milling and

calcinations method. This method is very convenient but the impurities are introduced from raw materials, milling media, and the calcination container. Because of the high temperature required for the complete reaction. The problems such as multiphase have to be minimized in order to generate homogeneous high performance perovskite. For example, LSCF represents a typical case. Raw materials La_2O_3, $SrCO_3$, CoO_3, and Fe_2O_3 were mixed and ball–milled. After drying, then the mixed powders were calcined at 1,000°C to remove impurities and to achieve single–phase perovskite powder. The high temperature was required to complete reaction.

1.1.11 Perovskite membrane preparation

1.1.11.1 Wet chemical synthesis of perovskite

Because of the perovskite synthesis via solid-state reaction has found that the impurities occurred. For this reason, the improvement of the perovskite synthesis has been interested continuously. A series of chemical methods, especially solution reaction or wet chemical synthesis or liquid phase synthesis, have been developed from solid-state synthesis. Solution reactions have been developed from solid-state synthesis to produce the required properties of raw perovskite powders, such as spray–pyrolysis, freeze drying, precipitation, sol-gel and liquid mix process, etc.

It is widely known that the synthesis of ceramic powders by using the conventional solid-state synthesis promotes the crystal growth and resulting in a hard agglomeration. The good sintered ability may be obtained when the preparation procedure is weak agglomerates are formed. Therefore, the properties of the raw material powder are largely determined by the properties of the raw material powders, which several requirements are imposed, fine particles (< 1 μm), narrow size range, no aggregation, controlled particle shape, uniformity in chemical and phase compositions, and high purity [22].

Liquid mix process is a generic name for various processes that start with a homogeneous solution containing the desired cations, which use additives and evaporation to convert the homogeneous liquid to rigid cross-linked polymer, and which utilize heat to convert the polymer into a homogeneous oxide powder.

Solubility is one of the most important considerations in solution techniques. Metal oxalates, sulphates, nitrates, chlorides, and acetates were avoided. Because of the low solubility of these compounds could lead to the phase separation in the final product. Not only it is desirable that solubility being high in order to minimize the amount of solvent which must be removed, but also the particular components must be compatible, e.g., iron sulfates could not be combined with barium chloride. Because of barium sulfate would precipitate in the reaction.

The initial process was pioneered by Pechini and is referred to either as Pechini process [23]. The following steps are used to achieve a powder.

1. An aqueous solution is prepared with metal alkoxides, oxides, hydrated oxides, or carbonates in an alpha-hydroxycarboxylic acid such as citric acid; the ratio of metal ions can be precisely controlled.

2. A polyhydroxy alcohol such as ethylene glycol is added and the liquid is heated to 150 to 250°C to allow the chelates to undergo polyesterification.

3. Heating is continued to remove excess water, resulting in solid polymeric resin.

4. The temperature is increased to about 400°C to char or decompose the resin.

5. The temperature is further increased to 500 to 900°C to form crystallites of the mixed oxide composition. The crystallites are typically 20 to 50 nm and clustered into agglomerates.

The citric process has been used to fabricate a variety of multicomponent electronic ceramic materials. The citrate solution synthesis process is similar to the Pechini process, except that ethylene glycol or other polyhydroxy alcohols are not utilized. To produce citrate precursor solutions, stoichiometric amounts of the desired metal nitrates are dissolved in water and citric acid is then added to form citrate species. This process results in solution species that have a lower organic content than in the Pechini process, and consequently, films that display less weight loss during conversion to the ceramic phase. The nitrate method simply involves the dissolution of the desired nitrates in deionized water or alcohol. The

approach is thus more straightforward than the Pechini and citrate routes, but dewetting of the substrate may present a problem.

In addition, the modified citrate method was synthesized by stoichiometric nitrates dissolved into HNO_3 and citric acid was added at a ratio of, citric acid to metal ions, 2:1. The pH value of the solution was adjusted to 9 by adding $NH_3.H_2O$ and the final solution was stirred for 24 hours. Spontaneous combustion occurred when the solution was dried at 473 K.

The modifications of Pichini process have been developed (was called citate method) that involved the use from citric acid and metal nitrate before thermal decomposition. For example, the production of Sr-substituted $LaMnO_3$ perovskite powder by the amorphous citrate process, obtained the manganese citrate-nitrate precursor as shown in Equation 1.21 [24]:

(1.21)
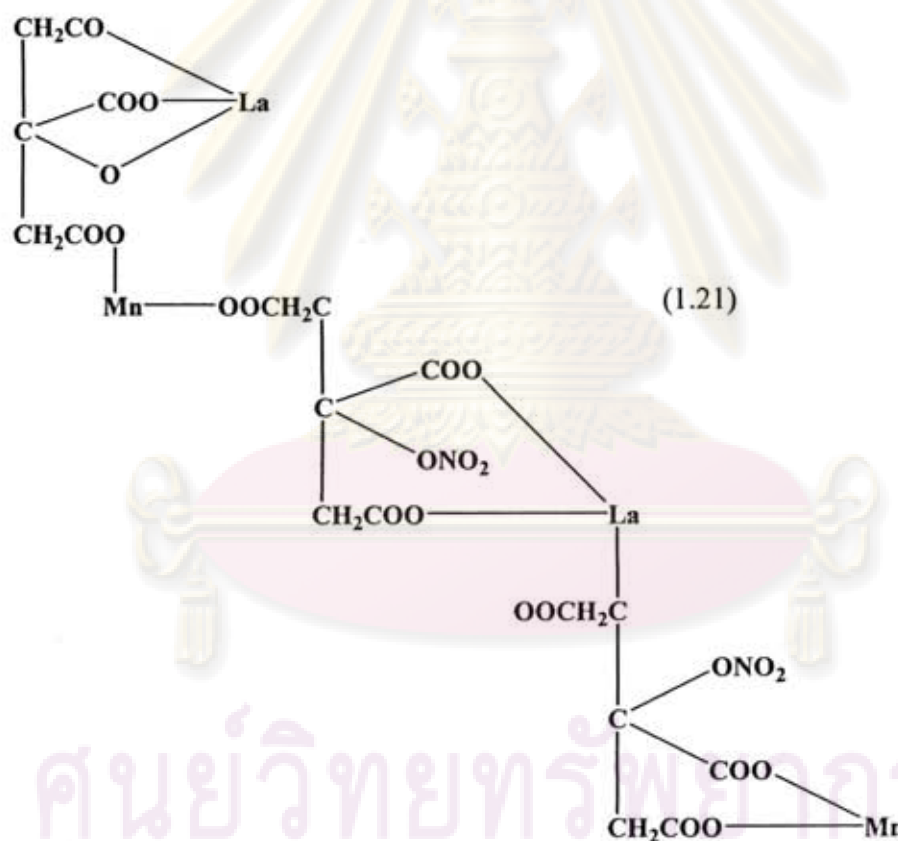
In the complex, the lanthanum is triply charged and replaces in normal citrate formation in the hydrogen of three –COOH groups and it replaces in the hydrogen of one –OH group and two –COOH groups. As manganese is divalent state

replaces in the hydrogen of two –COOH groups while NO_2 replaces the hydrogen of one –OH group, respectively.

In all cases the minimum amount of citric acid used was that necessary to bond the metals if all the NO_3^- ions were replaced. However, the amounts of metal and citric acid should not less than equimolar. If the high amount of citric acid was used, Mn_2O_3 was presented from the complex as in Equation 1.22:

$$\begin{array}{l}
CH_2COO \\
\quad | \quad\quad ONO_2 \quad Mn \\
\quad C \\
\quad | \quad\quad COO \\
CH_2COO \\
\quad\quad | \\
\quad Mn \quad\quad OOCH_2C \\
\quad\quad\quad\quad | \quad COO \\
\quad\quad\quad\quad C \\
\quad\quad\quad\quad | \quad ONO_2 \\
\quad\quad\quad CH_2COO \quad\quad Mn
\end{array}$$

(1.22)
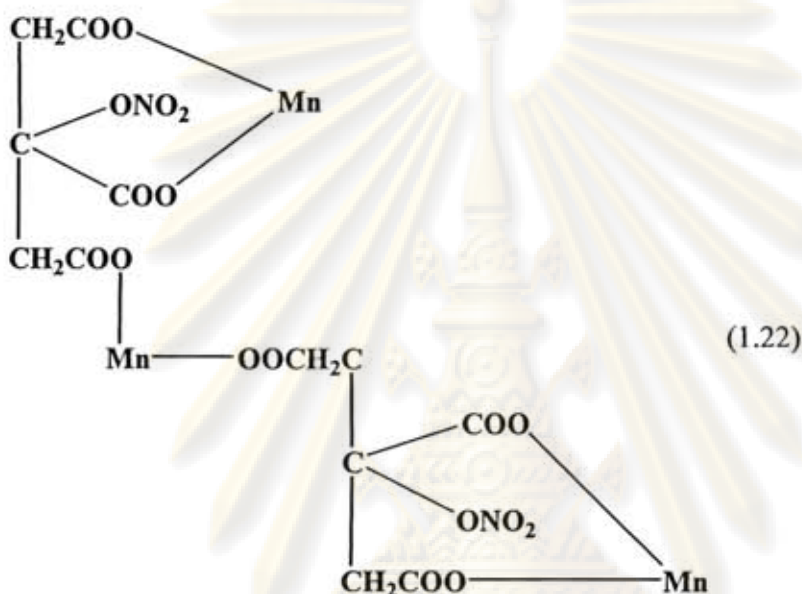
The formation of above structure would allow some citric acid, water, and nitrate ions to be lost during the preparation of gel. Every three molecules of citric originally present one remains uncombined and may be removed from the mixture by either evaporation or decomposition to yield acetone, carbon dioxide and water during the precursor preparation in the vacuum oven. The formation of this complex would also liberate NO_3^- groups for each two molecules of $Mn(NO_3)_2$ originally present in solution. The calcinations temperature should be higher than $800^{\circ}C$ because the wide range of homogeneity at lower temperatures was a result of the segregation of $Sr(NO_3)_2$ during precursor preparation and the production of $SrCO_3$ during precursor decomposition. However, it should not be higher than $1,100^{\circ}C$ because these would inevitably lead to a decrease in surface area. They also reported that the best compromise would appear and initial treatment of the precursor at $700^{\circ}C$ to yield the

high surface area followed by an increase in temperature to $1,100^{\circ}C$ for a period of up to 4 hours to remove carbon.

Another modification of the Pechini process was called the citric acid pyrolysis method [25]. The citrate process is a synthesis route which can lead to the $YBa_2Cu_3O_{7-\delta}$, the mixed metal oxides were dissolved by nitric acid. Then pH value of the dissolved nitrate solution was adjusted by $NH_3.H_2O$ and then NH_4NO_3 served as fuel. It is a particular type of sol-gel method, and offers the advantage of relative simplicity and the feasibility of the chemical compounds used in the development of the process. The method assures a great local and overall stoichiometry.

The perovskite powders made by wet chemical methods are very fine, and can be not agglomerate, which facilitates the densification process. The powders made from wet chemical methods using sintering temperature which can be lower than those made from conventional solid-state synthesis methods. By means of these wet chemical methods, it is possible to obtain monophasic, pure, fully reacted powders with submicronic and even nanometric sizes, homogeneous and narrow size distribution, and very reactive characteristic. When comparing several techniques in wet chemical methods, liquid mix process is distinguished in the case of less energy consumption, simplest technology, and potential to get fine particles and a singlephase powder. Both adding several acids such as citric, malic acid, or etc. and adjusting the pH of aqueous solution are used to provide the fine homogeneous perovskite with the high surface area.

1.1.12 Powder sizing

Powder particles are influenced on compacting and sintering. A single particle size does not produce good packing. Optimum packing for particles all the same size results in over 30% void space. Adding particles of a size equivalent to the largest voids reduces the void pore volume to 23%. Therefore, to achieve maximum particle packing, a range of particle sizes is required. Powder particles are influenced on compacting and sintering. The objective of the pressing step is to achieve maximum particle packing and uniformity.

Hard and dense agglomerates in ceramic powders usually result in large interagglomerate pores after sintering. Therefore small particle size is important

because it facilitates the high strength of green disc and the sintering process. The primary driving force for densification of a compact powder at high temperature is the change in surface free energy. Very small particles have high surface areas. The high surface free energy and very strong thermodynamic driving force decrease their surface by bonding them together. The particle with approximate sizes of 1 μm or less can be compacted into a porous shape and sintered at a high temperature to near-theoretical density [26]. Typically, the finer the powder, the greater its surface area, and the lower the temperature and shorter time for densification. Long time of the sintering temperature causes of the increasing in grain growth and lowering strength. calcined powder is not usually available with the optimum particle size distribution. The ball milling and screening are the common techniques to achieve the desire particle size of powder.

1.1.13 Powder compacting by uniaxial pressing

Uniaxial pressing is accomplished by placing the powder in to a rigid die and applying pressure along a single axial direction through a rigid plunger, or piston to achieve compacting. Pressing results in the direct contact of particles, reduces the average distance between particles, and changes the shape of particles. The apparent density of a compact was controlled by mixing of the proper various particles size fractions.

To enhance the compacting, before pressing, the powder should be disaggregated by mixing the powder with solvent such as isopropanol in the ultrasonic bath or added a couple drops of acetone to reduce the surface tension.

1.1.14 Sintering

Sintering is the process whereby powder compacts are heated so that adjacent particles fuse together. The fusing of particles results in an increase in the density of the part and hence the process is sometimes called densification. There are some processes such as hot isostatic pressing which combine the compaction and sintering processes into a single step.

The density of the component can also change during sintering, depending on the materials and the sintering temperature. These dimensional changes can be

controlled by an understanding and control of the pressing and sintering parameters, and components can be produced with dimensions that need little or no rectification to meet the dimensional tolerances. The driving force for sintering is the decrease in surface free energy that occurs as the surface area of the polycrystalline aggregate is reduced. This process can be achieved by solid-state reaction or alternatively in the presence of a liquid phase. When a powdered aggregate is sintered, pore size is reduced, and the grain growth can be much enhanced. The growth of the neck is due to the transport of matter or of the counter-flow of vacancies between the particles and the pores. In crystalline powder, its transport occurs by diffusion (bulk, surface, or grain boundary diffusion), whereas in amorphous materials, it occurs by viscous flow. Kuczynski has defined the neck growth as in Equation 1.23.

$$X^n/r^m = kt \tag{1.23}$$

Where X and r are defined in Figure 1.7, t is the time, k is the temperature dependent constant, n and m are constants dependent on the mechanisms of growth, viscous or bulk diffusion, surface diffusion, or evaporation and condensation.

Three stages of sintering can be distinguished. The early stage or initial stages during which the necks form at points of particle contact and the particles usually center approach each other. At this stage the individual particles are still distinguishable. The intermediate stage during that the necks become large, resulting in the formation of an interconnected pore structure. The third or the final stages during, the pores become isolated. Elimination of the interconnectivity of pores eliminates surface and vapor transport.
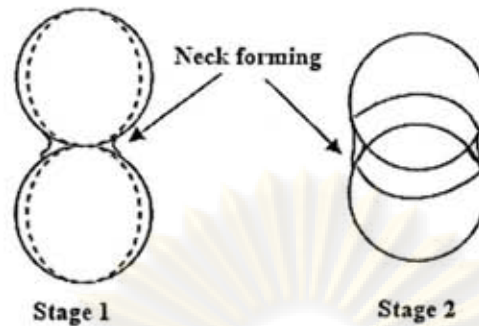
Figure 1.7 Mechanism of sintering.

Closed pores isolated from grain boundaries shrink very slowly because grain boundary diffusion is far away from the pores. The growth of grains, therefore, hinders the attainment of theoretical density, since the pore's growth is also enhanced. It is essential, therefore, to retard grain growth so that densification of the compact can continue to the theoretical limit. This is particularly important with the present trend of using ultrafine particles as starting materials for the fabrication of technical ceramics. Surface diffusion becomes important in the case of very fine particles. Grain boundary diffusion and volume diffusion are the main mechanisms causing shrinkage of the neck, whereas surface diffusion does not contribute to any shrinkage. The most important diffusion paths during the sintering of two spheres with a grain boundary are surface diffusion, grain boundary diffusion, volume diffusion from the grain boundary to the neck surface, and volume diffusion from the sphere surface to the neck surface. The sintering rate also affected by the crystallization and growth processes, which occur concurrently. The sintering rate is reduced when there is intensive grain growth because when diffusion forms the pores occurs toward the boundaries of individual grains, the distance over which diffusion occurs with a reduction in pores is determined by the size of the crystals.

1.2 Literature review

In 2000, Odier, *et al.* [27] have studied the stability of $Pr_2NiO_{4-\delta}$ under pure oxygen flow by *in situ* measurement of its weight versus T. Above 850°C a fast oxidation is observed corresponding to the ex-solution of PrO_y species and to the formation of metallic $Pr_4Ni_3O_{10-x}$. This reaction is not reversible. The quantity of

exchanged oxygen, its fast kinetics, and the metallic behavior of the composite suggest that this material should have interesting applications for electrodes of solid oxide fuel cells.

In 2001, Kharton, *et al.* [28] reported results on oxygen permeation through dense ceramics of $La_{2x}Sr_xNi_{1-y-z}Fe_yCu_zO_{4+\delta}$ ($x = 0$–0.10; $y = 0.02$–0.10; $z = 0$–0.10), $LaPrNi_{0.9}Fe_{0.1}O_{4+\delta}$, $La_2Cu_{1-x}Co_xO_{4+\delta}$ ($x = 0.02$–0.30) and $Ln_2CuO_{4+\delta}$ (Ln = Pr, Nd) at 973–1223 K suggest two significant contributions to the ionic conductivity of the oxygen-hyperstoichiometric phases with K_2NiF_4-type structure. 1) Oxygen interstitial migration in the rock-salt-type layers of the K_2NiF_4-like lattice increases with increasing temperature. 2) The role of oxygen vacancy diffusion in the perovskite layers increases when temperature decreases. This behavior was attributed to the lower activation energy for ionic conduction via the vacancy diffusion mechanism. The oxygen permeability of the title materials was found to be limited by both bulk ionic conductivity and surface exchange rates and may thus be enhanced by catalytically active layers, including Pt, Ag and praseodymium oxide, deposited on the membrane surface. Thermal expansion coefficients of the title materials vary in the range of $(10.1$–$13.4) \times 10^{-6}$ K^{-1}. Relatively low TEC values are the major advantage of K_2NiF_4-like nickelates and cuprates.

In 2002, Kilner, *et al.* [29] determined oxygen diffusion and surface exchange coefficients for the materials $La_2Ni_{1-x}Co_xO_{4+\delta}$ by the Isotope Exchange Depth Profile Secondary Ion Mass Spectrometry (IEDP SIMS) method. It is shown that the addition of cobalt ($0 < x < 0.5$) leads to the formation of single-phase materials and that the oxygen diffusion coefficient varies only slightly with x. In contrast, the surface exchange coefficient was found to be strongly dependent upon the value of x, with the activation enthalpy for this process dropping to values as low as ~20 kJ mol^{-1} for the high cobalt content material.

In 2003, Skinner, *et al.* [30] studied $La_2NiO_{4+\delta}$ structure using in-situ high temperature neutron diffraction over a temperature range of 25–800 °C in vacuum. The behavior of this material, and in particular the oxygen interstitial content, is discussed and quite remarkable bond length changes observed. It is observed that at temperatures above 150 °C $La_2NiO_{4+\delta}$ transforms to the tetragonal *I4/mmm* structure and maintains this over the entire temperature range on both heating and cooling. The

loss of the interstitial oxygen was observed over the low temperature region of the study and significant changes in both lattice constant and bond lengths found to mirror these changes, indicating the structural importance of the interstitial oxygen.

Ullmann, et al. [5] investigated the $A_{2-a}A'_aMO_{4-x}$ oxides (A= La; A'= Sr; M= Mn, Fe, Co, Ni) with the perovskite-related K_2NiF_4-type structure and compared with the characteristics of perovskite-type oxides AMO_{3-x} containing the same cations. The K_2NiF_4-type manganites, ferrites, cobaltites and nickelates are assumed to be reduction products of the corresponding perovskite-type oxides. The thermodynamic stabilities, in terms of reversible oxygen desorption, were higher than those of the corresponding perovskite-type oxides. Within the range of oxygen partial pressure (pO_2) from air to argon/H_2/H_2O, the oxidation states of the M cations were determined. The comparison of the oxidation states of M in AMO_{3-x} and (AMO_{3-x}).AO gives evidence on the stabilizing influence of the AO interlayer on the perovskite layer. The electrical conductivity of the A_2MO_4 oxides was of p-type and reached values close to 100 S cm^{-1} at high oxygen partial pressures and 800 °C for nickelates and cobaltites. The thermal expansion of K_2NiF_4-type oxides is generally lower than that of the comparable perovskite-type oxides.

In 2004, Whitfield, et al. [31] synthesized the solid solution, $La_2Ni_{1-x}Co_xO_{4+\delta}$ ($0.00 \leq x \leq 1.00$), based on the K_2NiF_4 structure by the Pechini method using both conventional and microwave heating and studied for potential use as cathodes in solid-oxide fuel cells. A structural phase transition was observed with increasing cobalt substitution, between $x = 0.50$ and 0.60 from tetragonal to orthorhombic symmetry. $La_2Ni_{1-x}Co_xO_{4+\delta}$, where $0.00 \leq x \leq 0.20$, is stable in air, and therefore are potential candidates for SOFC cathode materials. Experiments have shown that microwave preparation of $La_2Ni_{0.9}Co_{0.1}O_{4+\delta}$ for 6 h leads to higher porosity than conventionally synthesized material. The long-term stability of $La_2Ni_{0.9}Co_{0.1}O_{4+\delta}$ and CGO and LSGM is questionable, given the formation of secondary phases on extended annealing at 950 °C. However, the retention of the smaller grained microstructure formed by the microwave synthesis, means that microwave processing may have benefits for long-term performance, and should be investigated further with other materials.

Kharton, *et al.* [32] studied the electrical properties of a series of Ni-containing phases, including $La_2Ni_{1-x}M_xO_{4+d}$ (M=Co, Cu; x=0.1–0.2) with K_2NiF_4 and perovskite-type structures, in the oxygen partial pressure range from 10-18 Pa to 50 kPa at 973–1223 K. Within the phase stability domain, the conductivity of layered nickelates is predominantly p-type electronic and occurs via small-polaron mechanism, indicated by temperature-activated hole mobility and $p(O_2)$ dependencies of electrical properties. In oxidizing conditions similar behavior is characteristic of Ni-containing perovskites, which exhibit, however, significant ionic contribution to the transport processes. The role of ionic conduction increases with decreasing $p(O_2)$ and becomes dominant in reducing atmospheres. All nickelate-based phases decompose at oxygen pressures considerably lower with respect to Ni/NiO boundary. The partial substitution of nickel in $La_2Ni(M)O_{4+\delta}$ has minor effect on the stability limits, which are similar to that of $La_{0.90}Sr_{0.10}Ga_{0.65}Mg_{0.15}Ni_{0.20}O_{3-\delta}$. On the contrary, praseodymium doping enhances the stability of $La_{0.50}Pr_{0.50}Ga_{0.65}Mg_{0.15}Ni_{0.20}O_{3-\delta}$ down to $p(O_2)$ values as low as 10^{-17}–10^{-10} Pa at 1023–1223 K.

In 2005, Aguadero, *et al.* [4] indicated materials formulated $La_2Ni_{1-x}Cu_xO_{4+\delta}$ ($0 \leq x \leq 1$) have been prepared by the nitrate-citrate route, having an orthorhombic K_2NiF_4 structure. $La_2NiO_{4+\delta}$, which under heat treatments (873–1098 K) and high oxygen pressure (200–250 bar), resulted to be the compound with the highest capability to accommodate excess oxygen ($\delta = 0.16$). This led to an increase of excess oxygen in the structure. Rietveld refinements on neutron powder diffraction data probe the excess of oxygen to be accommodated as interstitial defect at the atomic position (1/4, 1/4, z; $z \approx 1/4$), which requires the displacement of four neighbouring oxygen atoms from their normal positions. This result is in agreement with a non-stoichiometry model which induces the stabilization of oxygen vacancies in the perovskite layer of these materials. Results obtained herein reveal heat treatment under high oxygen pressure (873 K, 200 bars) as a promising method to enhance transport properties in K_2NiF_4-type structures.

Fontaine, *et al.* [33] developed composition and porosity graded $La_{2-x}NiO_{4+\delta}$ ($x \geq 0$) cathode interlayers for low-temperature solid oxide fuel cell that exhibit good adhesion with the electrolyte, controlled porosity and grain size and good electrochemical behaviour. $La_{2-x}NiO_{4+\delta}$ ($x \geq 0$) monolayers are prepared from a derived

sol–gel method using nitrate salts, acetylacetone and hexamethylenetetramine in acetic acid. As a function of the organic concentration and the molar ratio of lanthanum to nickel, these layers present platelets or spherical shape grains with a size distribution ranging from 50 to 200 nm, as verified by SEM-FEG.

In 2006, Qing Xu, *et al.* [34] synthesized $La_2NiO_{4+\delta}$ with a pure K_2NiF_4 phase from a polyaminocarboxylate complex precursor with diethylenetriaminepentaacetic acid (H_5DTPA) as ligand. Powder (100–200 nm) with a pure K_2NiF_4 phase was produced by calcining the complex precursor at 900 °C for 2 h in air. It was found that $La_2NiO_{4+\delta}$ ceramic sintered at 1300 °C for 4 h shows a dense microstructure with average grain size of about 1 μm. The $La_2NiO_{4+\delta}$ ceramic exhibit an electrical conductivity of 76 $\Omega-1$ cm-1 at 800 °C. This research demonstrates the advantage of the polyaminocarboxylate complex method in preparing $La_2NiO_{4+\delta}$ with respect to the simplicity of synthesis process, fine and uniform morphology of synthesized powder and superior electrical conducting properties of sintered specimen.

Kharton, *et al.* [39] studied the oxygen hyperstoichiometry of K_2NiF_4-type $La_2Ni_{0.9}Fe_{0.1}O_{4+\delta}$ by the coulometric titration and thermogravimetric analysis at 923–1223 K. Doping of lanthanum nickelate with iron increases the oxygen excess under oxidizing conditions, but has a minor effect on the low-p (O_2) phase stability. In the oxygen partial pressure range 6×10^{-5}–0.7 atm, the p (O_2)-T-δ diagram can be adequately described by equilibrium process of oxygen incorporation, electron hole localization on Ni^{2+} cations blocking neighboring sites in the B sublattice, and a similar site-exclusion effect near interstitial anions. The predominant state of iron cations under oxidizing conditions, confirmed by the Mossbauer spectroscopy, is 3^+. Due to very low chemical expansion of $La_2Ni_{0.9}Fe_{0.1}O_{4+\delta}$ lattice, the thermodynamic functions governing oxygen intercalation and the site-blocking factors are independent of defect concentrations. Although the hole mobility in $La_2Ni_{0.9}Fe_{0.1}O_{4+\delta}$ tends to weakly decrease with increasing temperature, the mobility values varying in the range of 0.16–0.18 $cm^2\times V^{-1}\times s^{-1}$ are characteristic of a hopping conduction mechanism.

Aguadero, *et al.* [41] studied the thermal evolution of the crystal structure of a cathode material across the usual working conditions in solid oxide fuel cells. It is essential to understand not only its transport properties but also its chemical and

mechanical stability in the working environment. In this regard, high-resolution neutron powder diffraction (NPD) measurements have been performed in air from 25 to 900 °C on O_2-treated (350 °C/200 bar) $La_2Ni_{0.6}Cu_{0.4}O_{4+\delta}$. The crystal structure was Rietveld-refined in the tetragonal $F4/mmm$ space group along all the temperature range. The structural data have been correlated with the transport properties of this layered perovskite. The electrical conductivity of O_2-treated $La_2Ni_{0.6}Cu_{0.4}O_{4+\delta}$ exhibits a metal (high T)-to-semiconductor (low T) transition as a function of temperature, displaying a maximum value of 110 S cm^{-1} at around 450 °C. The largest conductivity corresponds, microscopically, to the shortest axial $Ni-O_2$ distance (2.29(1) A°), revealing a major anisotropic component for the electronic transport. We have also performed a durability test at 750 °C for 560 h obtaining a very stable value for the electrical conductivity of 87 S cm^{-1}. The thermal expansion coefficient was 12.8 x10^{-6} K^{-1} very close to that of the usual SOFC electrolytes. These results exhibit $La_2Ni_{0.6}Cu_{0.4}O_{4+\delta}$ as a possible alternative cathode for IT-SOFC.

Ishihara, et al. [35] studied Pr_2NiO_4-based oxide as a new mixed electronic and oxide ionic conductor. It was found that Pr_2NiO_4 doped with Cu and Fe for Ni site exhibits the relatively high oxygen permeation rate. The trivalent cation seems to be effective for increasing the oxygen permeation rate. Among the examined cation, the highest oxygen permeation rate was obtained by doping 5 mol% Fe. Chemical stability of Pr_2NiO_4-based oxide seems to be reasonably high. Application of this new mixed conductor for the oxygen permeation membrane under the CH_4 partial oxidation was also studied and it was confirmed that the oxygen permeation rate much improved under the CH_4 oxidation condition.

Vashook, et al. [36] prepared potential cathode materials $Pr_{2-x}Sr_xNiO_{4\pm\delta}$ compositions with x=0.3 and 0.6 at 1300 °C in air and their electrical conductivity and oxygen non-stoichiometry were investigated in the temperature range 20–1000 °C and oxygen partial pressure (pO_2) 1–21,000 Pa. Sr-doping allows partially to stabilize the $Pr_2NiO_{4\pm\delta}$ structure, but some phase transitions were observed in spite of that. The electrical conductivity and the oxygen mobility of the Pr- and La-containing ceramic nickelates with K_2NiF_4- type structure are 10–15% higher for $Pr_{2-x}Sr_xNiO_{4\pm\delta}$ compounds at the same temperature and oxygen partial pressure.

Miyoshi, *et al.* [37] investigated K_2NiF_4-type oxides of $Pr_2Ni_{0.8-x}Cu_{0.2}Fe_xO_4$ as a new MIEC material for oxygen-permeating membranes. An X-ray diffraction analysis suggested that a single phase K_2NiF_4-type structure was obtained in the composition range from x=0 to 0.05 in $Pr_2Ni_{0.8-x}Cu_{0.2}Fe_xO_4$. The electrical conductivity of $Pr_2Ni_{0.8-x}Cu_{0.2}Fe_xO_4$ gradually decreased with the increasing amount of Fe substituted for Ni. However it showed a high hole conductivity and also exhibited an excellent oxygen permeation rate. $Pr_2Ni_{0.75}Cu_{0.2}Fe_{0.05}O_4$ has a high chemical stability, Therefore, the K_2NiF_4-type oxide of $Pr_2Ni_{0.75}Cu_{0.2}Fe_{0.05}O_4$ is highly promising as an oxygen-permeating membrane material.

Wen, *et al.* [38] synthesized $A_{2-a}A'_aMO_4$ (A=Pr, Sm, A'=Sr, M=Ni, Mn) with K_2NiF_4-type structure by solid reaction. Their chemical stability, electrical conductivity and thermal expansion behavior as well as cathodic polarization were investigated in relation to the cathode of SOFC. The results showed that $A_{2-a}A'_aMO_4$ exhibited a low reactivity with yttria stabilized zirconia (YSZ) electrolyte. The thermal expansion coefficient (TEC) values changed with the ionic radius of A. The conductivities of the nickelate, which were about 102 S cm^{-1} at 800 °C, are about one order of magnitude higher than those of manganite. While the nickelates showed a lower cathodic polarization in comparison with manganites. In conclusion, therefore, nickelate $A_{2-a}A'_aMO_4$ exhibited a higher potential to be used as cathode for SOFC after optimizing the composition.

In 2007, Kovalevsky, *et al.* [40] appraised the oxygen permeability and stability of dense $Pr_2NiO_{4+\delta}$ ceramics in comparison with K_2NiF_4-type lanthanum nickelate. In oxidizing atmospheres, $Pr_2NiO_{4+\delta}$ exhibit an extensive oxygen uptake and decomposition into the Ruddlesden–Popper-type $Pr_4Ni_3O_{10}$ and praseodymium oxide at temperatures below 900°C. At 900–950°C when the K_2NiF_4-type praseodymium nickelate is stable in the ceramic membranes placed under an oxygen partial pressure gradient, the steady-state oxygen permeability of $Pr_2NiO_{4+\delta}$ is similar to $La_2NiO_{4+\delta}$. The phase changes on cooling lead to considerably higher oxygen permeability, which becomes comparable to that of perovskite-type cobaltites, and to noticeable isothermal expansion. The stability of $Pr_2NiO_{4+\delta}$ in reducing atmospheres, estimated from the $p(O2)$ dependencies of total conductivity and Seebeck coefficient, is lower than that of $La_2NiO_{4+\delta}$, probably due to a smaller size of the A-site cation.

Ishihara, *et al.* [42] investigated Pr_2NiO_4-based oxides as a series of new mixed electronic and oxide-ionic conductors for oxygen permeation membrane. High electronic conductivity was observed for the Pr_2NiO_4 system and the temperature dependence was of metal-like behavior, i.e., it decreased with elevating temperature. The oxygen permeability of Pr_2NiO_4-based oxides was much higher than that of La_2NiO_4-based oxides with the same K_2NiF_4-type structure. The effects of the Ni-site dopant were also studied and it was found that the oxygen permeation rate was improved by doping Cu and Mg. In particular, doping of Cu is most effective for enhancing the oxygen permeation rate from air to He, and the optimum concentration of Cu was found at 20%. The maximum permeability of 60 μmol min^{-1} cm^{-2} at 1273 K was attained using a 0.5 mm thick $Pr_2Ni_{0.8}Cu_{0.2}O_4$ membrane. Addition of the excess Cu to $Pr_2Ni_{0.8}Cu_{0.2}O_4$ significantly enhanced the oxygen permeation rate, probably due to the remarkable grain growth assisted by the formation of some Cu-containing liquid phase, and the oxygen permeation rate reached to 100 μmol min^{-1} cm^{-2} with the same conditions.

According to the past studies, many researches demonstrated that perovskite type K_2NiF_4 structure is suitable for using as cathode material for solid oxide fuel cell because they have high stability in air and less thermal expansion than perovskite type ABO_3 structure. From many researches, ionic conductivity of La_2NiO_4 is higher than La_2CuO_4 and ionic radius of Praseodymium (Pr) is similar to Lanthanum (La). Moreover, Pr is a metal which is rarely studied. La_2NiO_4 shows a promising candidate for SOFC cathode. Because of similarity of Pr to La, it is likely that Pr_2NiO_4 can be used as cathode material. Therefore Ni is interested to improve the electrical conductivity by doping various metals at B site of Pr_2NiO_4.

Therefore, in the present work, $Pr_2Ni_{1-x}M_xO_4$, $Pr_2Ni_{1-x}M_xGa_{0.05}O_4$ and $Pr_2Ni_{1-x-0.05}M_xGa_{0.05}O_4$ (M = Cu, Co, Mg, Zn, In and x = 0.1-0.3) were synthesized by modified citrate method and characterized by XRD for the crystal structure, We are interested in exploring the tendency of doped Pr_2NiO_4 materials for cathode of SOFC. Their properties were investigated by TGA, O_2-TPD and DC4-probes methods.

1.3 The objectives of the thesis

The objectives of this study are as folows:

1. To synthesize perovskite powders of $Pr_2Ni_{1-x}M_xO_4$, $Pr_2Ni_{1-x}M_xGa_{0.05}O_4$ and $Pr_2Ni_{1-x-0.05}M_xGa_{0.05}O_4$ (M = Cu, Co, Mg, Zn, In and x = 0.1-0.3)

2. To prepare perovskite disks and characterize the structure by XRD.

3. To study properties of this material such as thermal, oxygen desorption and electrical property.

ศูนย์วิทยทรัพยากร
จุฬาลงกรณ์มหาวิทยาลัย

CHAPTER II

EXPERIMENTAL

The chemicals, apparatus and experimental procedures such as processing of perovskite powders synthesis, perovskite disc preparation and characterization of materials, are described as below:

2.1 Chemicals

The chemicals listed in Table 2.1, were used without further purification.

Table 2.1 Reagents for synthesis of perovskites.

Reagents	Formula Weight	Purity%	Company
$Pr(NO_3)_3 \cdot 6H_2O$	435.02	99.9	Aldrich
	435.01	99.9	Mitsuwa
$Ni(NO_3)_2 \cdot 6H_2O$	290.79	98.0	Wako
$Cu(NO_3)_2 \cdot 3H_2O$	241.60	99.0	Fluka
$Co(NO_3)_2 \cdot 6H_2O$	291.03	98.0	Fluka
$Zn(NO_3)_2 \cdot 6H_2O$	297.48	99.0	Fluka
$In(NO_3)_3 \cdot 3H_2O$	354.88	-	Wako
$Mg(NO_3)_2 \cdot 6H_2O$	256.41	99.0	Fluka
$Ga(NO_3)_3 \cdot xH_2O$	255.74	99.999	Aldrich
$C_6H_8O_7$	192.43	99.5	Fluka

Reagents	Formula Weight	Purity%	Company
HNO_3	63.01	65	Merck
liq.NH_3	35.05	25	Merck
C_2H_5OH	46.07	-	Merck

2.2 Synthesis of perovskite powder by modified citrate method

The perovskite powders $Pr_2Ni_{1-x}M_xO_4$, $Pr_2Ni_{1-x}M_xGa_{0.05}O_4$ and $Pr_2Ni_{1-x-0.05}M_x$ $Ga_{0.05}O_4$ (M = Cu, Co, Mg, Zn, In and x = 0.1-0.3) were synthesized in basic solution. Stoichiometric amounts of corresponding high purity metal nitrates (based on 5 g. of perovskite powder) were partially dissolved in 10 ml ultra pure nitric acid (65%). Then citric acid was added with stirring at a ratio of citric acid to metal ions (2:1). The mixture solution was then titrated with $NH_3.H_2O$ at the controlled rate of 2-3 ml/min. The pH value of the solution was adjusted to ~9.

The combustion of the homogeneous solution was carried out on a hot plate at around 200-300°C by slowly heating temperature in a three-liter beaker covered with a fine sieve to prevent the loss of fine powder. The water was evaporated until a sticky gel was obtained. Then it became a large swelling viscous mass and finally self ignited by NH_4NO_3. The combustion lasted for about 10-20 seconds. The resulting powder was ground by mortar and pestle, subsequently the synthesized perovskite oxide was calcined in a Carbolite RHF 1600 muffle furnace in air to achieve phase purity and remove the residual carbon. The conditions used for the calcination of the perovskite powders were set as follows:

800°C, dwell 6 hrs.

2 hrs.   2 hrs.

Room temperature   Room temperature
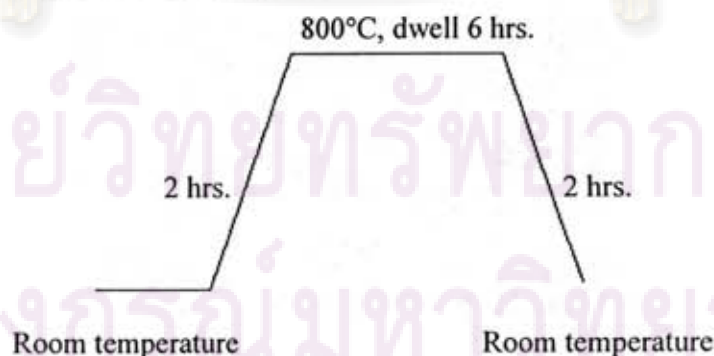
Scheme 2.1 The calcination condition of perovskite powder.

The particle was ground completely well by mortar before characterization.

The equation for the formation of these perovskites assuming complete combustion of the redox mixtures containing citric acid, for example, $Pr_2Ni_{1-x}Cu_xO_4$, can be written as;

$$Pr(NO_3)_3 + (1-x)Ni(NO_3)_2 + xCu(NO_3)_3 + 2HOC(COOH)(CH_2COOH)_2$$

$$Pr_2Ni_{1-x}Cu_xO_{4-\delta} (s) + 12CO_2 (g) + 8H_2O (g) + 3N_2 (g) \qquad (2.1)$$
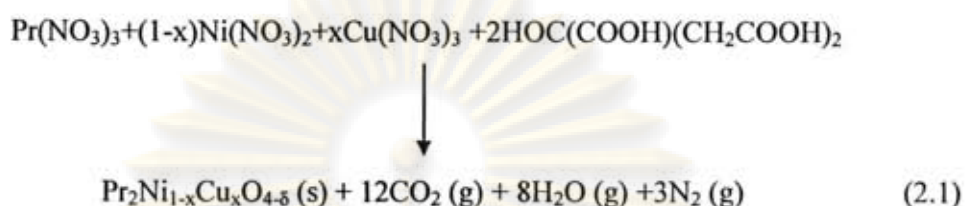
According to Equation (2.1), two moles of citric acid are required to react with 2 moles of all combined metal nitrates. In other words, the total metals will react with citric acid in the approximately equimolar ratio. However, in practice, the excess amount of citric acid was used to assure the complete reaction of all the metal nitrates. Normally, three moles of citric acid was used to react with 2 moles of the total metal nitrates. Therefore, every three molecules of citric acid originally present, one remained uncombined and was removed from the mixture later by either evaporation or decomposition to yield carbon dioxide and water during heating in the vacuum oven. In this research, the amount of citric acid is twice as much as the total metal nitrate, was used in the synthesis of each perovskites.

2.3 Perovskite disc preparation

A KBr die was used for the shape-forming process, which includes loading, pressing and ejecting.
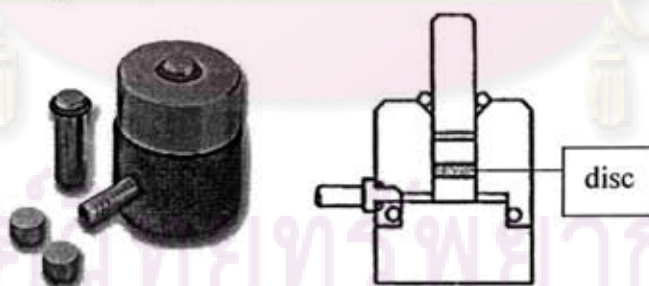
Figure 2.1 shows KBr die.

The calcined perovskite powder was ground and loaded into the cavity. The die having the perovskite powder inside was knocked against table for 2-3 times to evaporate the air inside the powder. After the die was completely assembled, the

plunger was brought to the surface of the powders gently for final leveling and then rotates for smooth surface. About 1-3 tons were then applied on the plunger of the die by the uniaxial pressing machine. At the beginning of pressing, the pressure was slowly applied to 1-3 ton for 20 minutes. The pressure was released and then the die was removed from the press. All the components were then stripped away except for the die assembly and plunger. Then the assembly was held while the press was slowly pumped until the pellet ejected. The black disc is around 1 mm thick, 20 mm diameter from 1.8 g of powder. Then the black discs were generally sintered in air. The sintering conditions were as follows:

1300°C, dwell 6 hrs.

3 hrs.

1000°C

6 hrs.

5 hrs.

Room temperature   Room temperature
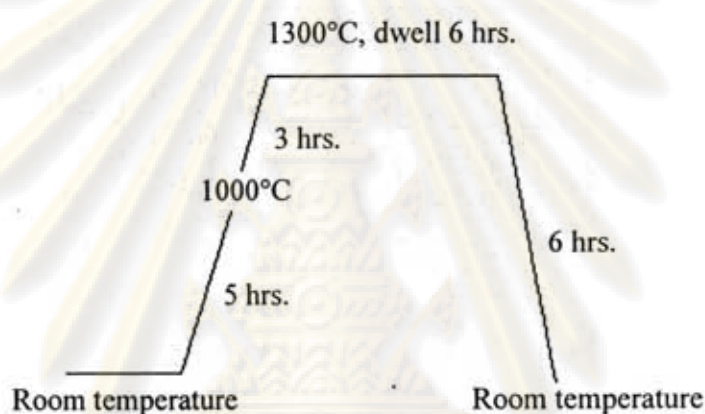
Scheme 2.2 The sintering conditions of perovskite disc.

Then the black discs changed to the dark gray discs.

2.4 Characterization of the perovskite oxides

2.4.1 X-ray diffractrometry (XRD)

The X-ray patterns, for either powder or disc, were taken by using Rigaku, DMAX 2002 Ultima Plus X-Ray powder diffractometer eqipped with a monochromator and a Cu-target X-ray tube (40 kV, 30 mA) and angles of 2θ ranged from 20-70 degree at Department of Chemistry, Faculty of Science, Chulalongkorn University. The phase formations of perovskite powders were characterized after calcination and sintering by XRD.

2.4.2 Scanning electron microscopy (SEM)

The morphology of the membrane discs was carried out using a JEOL JSM-5800LV scanning electron microscopy, Oxford Instrument (model Link ISIS series 300) at the Scientific and Technological Research Equipment Center (STREC), Chulalongkorn University. This instrument uses X-rays or electrons scattered back from the surface "illuminated" by a restored electron beam to generate an image with remarkable three-dimensional qualities.

2.4.3 DENSITY

Density of perovskite disc was determined by the Archimedes immersion method using distillated water as a medium, Precisa Gravimetrics AG (model R 2055M – DR), at Department of Chemistry, Faculty of Science, Chulalongkorn University.

2.4.4 Thermogravimetric analysis (TGA)

Thermogravimetric analysis (TGA) was performed on TA instrument thermogravimetric analyzer (model SDT 2960) at Department of Chemistry, Faculty of Science, Chulalongkorn University. The powder specimen after sintering was heated up from room temperature to 1,000°C under N_2 atmosphere and heating rate of 20 °C/min.

2.4.5 Temperature-programmed desorption (TPD)

The perovskite capabilities of adsorbing O_2 were measured by oxygen Temperature-programmed desorption (O_2-TPD), at Department of Chemistry, Faculty of Science, Chulalongkorn University.

The perovskite capabilities of adsorbing O_2 were measured using temperature-programmed desorption (O_2-TPD), BEL JAPAN, INC. (model BEL-CAT) at Department of Chemistry, Faculty of Science, Chulalongkorn University. About 200 mg of sample was loaded in a U-shape quartz tube. Helium was used as the carrier gas with a flow rate of 40 ml/min. The first step, the perovskite powder (sintered) was pretreated, the perovskite powder was heated to 900°C in He flow for 100 min and then 99.99% O_2 gas was flowed for 120 min, after adsorbed 99.99% O_2 gas, then

cooled to 100°C for 100 min. The powder was maintained at 100°C in He flow for another 30 min to eliminate physically adsorbed O_2. The temperature increased from 100°C to 900°C at a rate of 10°C/min. TCD was used on line with a computer data acquisition system. The obtained values are described to the desorbed amount of oxygen from the sample.

2.4.6 Electrical conductivity

The electrical conductivity of the perovskite materials was measured by the conventional DC 4-probes method using Pt electrode. Specimens of perovskite were sintered at 1300 °C for 6 h in air. The relative densities of specimens ranged from 95% to 99%. The sintered disk was cut into a rectangular shape with approximate dimensions of 0.12 cm × 0.52 cm × 1.12 cm. Four platinum (Pt) wires were attached to the rod with Pt paste. Two current contacts were made at the rod edges, and two voltage contacts in between at a distance L. The sample was then fired at 950 °C for 10 min with a heating rate of 5 °C/min to allow complete adhesion of the electrodes, obtain a firm bonding and good electrical contact between the Pt wires and the sample. Measurements were performed from room temperature to 800 °C with a heating rate of 5 °C/min. The voltage (V) between the two inner electrodes and the current intensity (I) were recorded after the sample was left at each temperature at which measurement was taken, for 40 min. The electrical conductivity was calculated by the equation:

$$S = (I/V)*(L/(W*T)) \ldots\ldots\ldots\ldots(2.2)$$

S = electrical conductivity

I = applied current (A)

V = resulting potential (V)

L = length between Pt (cm)

T = thickness of memprane (cm)

W = wide of membrane (cm)
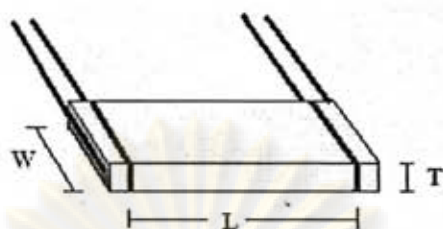
Figure 2.2 shows a rectangular specimen of perovskite. Four platinum (Pt) wire contacts were made. W = wide L = length T = thickness
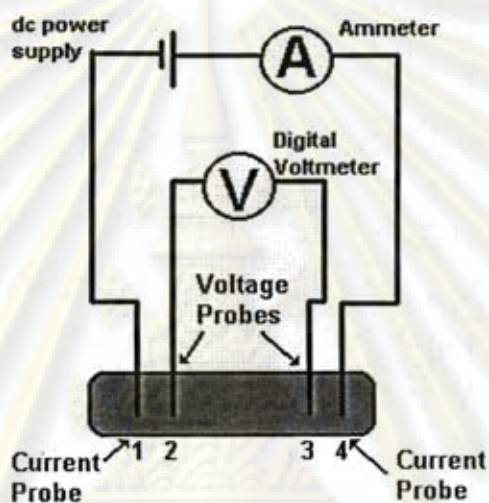
Figure 2.3 shows scheme of DC 4-probes method.

ศูนย์วิทยทรัพยากร

จุฬาลงกรณ์มหาวิทยาลัย

CHAPTER III

RESULTS AND DISCUSSION

3.1 Synthesis of perovskite powder by modified citrate method

The $Pr_2Ni_{1-x}M_xO_4$, $Pr_2Ni_{1-x}M_xGa_{0.05}O_4$ and $Pr_2Ni_{1-x-0.05}M_xGa_{0.05}O_4$ (M = Cu, Co, Mg, Zn, In and x = 0.1-0.3) perovskite-like were synthesized by modified citrate method. Citric acid is utilized as a complexing agent. The complexation process increases the solubility of metal ions and helps to maintain homogeneity by preventing their selective precipitation.

By modified citrate method, the metal nitrates were dissolved in 70% nitric acid, which then reacted with citric acid to form metal-citrate-nitrate complexes. Liquid ammonia was added for adjust pH of solution and fuel in the process. These metal-citrate complexes can undergo polymerization when liquid ammonia was added. Meanwhile $NH_3.H_2O$ was added, the white fume of NH_4NO_3 was suddenly observed, which came from the free NO_3^- reacting with $NH_3.H_2O$ and generating the heat. In the case of $Pr_2Ni_{0.9}Cu_{0.1}O_4$, in the first the color of the mixture changed from green solid to clear green solution when 70% nitric acid was added. Afterwards the solution was titrated by $NH_3.H_2O$ and remained green solution at $NH_3.H_2O$ 3 ml and fume stopped at $NH_3.H_2O$ 12 ml. At this point, the remained citric acid and NH_4NO_3 might dissolve in the solution due to the adding of $NH_3.H_2O$. Then the solution changed to blue cloudy solution when liquid ammonia was increased ($NH_3.H_2O$ 17 ml) and to clear blue solution ($NH_3.H_2O$ 20 ml, pH $\approx$ 8). This solution indicated the metal citrate-nitrate gel resulting from the polymerization of the metal citrate-nitrate complex when $NH_3.H_2O$ was increased. Finally, the solution changed from clear blue to clear deep blue solution (pH $\approx$ 9).

The combustion of metal citrate-nitrate gel solution was composed of three steps, evaporation, decomposition, and spontaneous combustion. The excess solvent was firstly evaporated until a sticky gel was obtained. Finally, at around $200^{\circ}C$ the spontaneous combustion was initiated to convert the mixture into the powder. The synthesized perovskite oxides were calcined at 800°C and sintered at 1300°C.

3.2 Tolerance number of perovskite compounds

The stability of the oxides was determined by the tolerance numbers. The tolerance number can be calculated from the Goldschmidt's equation (Appendice A).

The calculated tolerance numbers of the synthesized compounds were summarized in Table 3.1.

Table 3.1 Tolerance number of prepared perovskites.

(a) $Pr_2Ni_{1-x}M_xO_4$

Compounds	Tolerance No.	Compounds	Tolerance No.
Pr_2NiO_4	0.873	$Pr_2Ni_{0.8}Zn_{0.2}O_4$	0.868
$Pr_2Ni_{0.9}Cu_{0.1}O_4$	0.871	$Pr_2Ni_{0.7}Zn_{0.3}O_4$	0.866
$Pr_2Ni_{0.85}Cu_{0.15}O_4$	0.870	$Pr_2Ni_{0.9}In_{0.1}O_4$	0.868
$Pr_2Ni_{0.7}Cu_{0.3}O_4$	0.868	$Pr_2Ni_{0.8}In_{0.2}O_4$	0.863
$Pr_2Ni_{0.9}Co_{0.1}O_4$	0.870	$Pr_2Ni_{0.7}In_{0.3}O_4$	0.859
$Pr_2Ni_{0.8}Co_{0.2}O_4$	0.868	$Pr_2Ni_{0.9}Mg_{0.1}O_4$	0.871
$Pr_2Ni_{0.7}Co_{0.3}O_4$	0.865	$Pr_2Ni_{0.8}Mg_{0.2}O_4$	0.870
$Pr_2Ni_{0.9}Zn_{0.1}O_4$	0.870	$Pr_2Ni_{0.7}Mg_{0.3}O_4$	0.869

(b) $Pr_2Ni_{1-x-0.05}M_xGa_{0.05}O_4$

Compounds	Tolerance No.	Compounds	Tolerance No.
$Pr_2Ni_{0.85}Cu_{0.1}Ga_{0.05}O_4$	0.872	$Pr_2Ni_{0.65}Zn_{0.3}Ga_{0.05}O_4$	0.868
$Pr_2Ni_{0.8}Cu_{0.15}Ga_{0.05}O_4$	0.872	$Pr_2Ni_{0.85}In_{0.1}Ga_{0.05}O_4$	0.869
$Pr_2Ni_{0.65}Cu_{0.3}Ga_{0.05}O_4$	0.869	$Pr_2Ni_{0.75}In_{0.2}Ga_{0.05}O_4$	0.865
$Pr_2Ni_{0.85}Co_{0.1}Ga_{0.05}O_4$	0.872	$Pr_2Ni_{0.65}In_{0.3}Ga_{0.05}O_4$	0.860
$Pr_2Ni_{0.75}Co_{0.2}Ga_{0.05}O_4$	0.869	$Pr_2Ni_{0.85}Mg_{0.1}Ga_{0.05}O_4$	0.873
$Pr_2Ni_{0.65}Co_{0.3}Ga_{0.05}O_4$	0.867	$Pr_2Ni_{0.75}Mg_{0.2}Ga_{0.05}O_4$	0.872
$Pr_2Ni_{0.85}Zn_{0.1}Ga_{0.05}O_4$	0.872	$Pr_2Ni_{0.65}Mg_{0.3}Ga_{0.05}O_4$	0.870
$Pr_2Ni_{0.75}Zn_{0.2}Ga_{0.05}O_4$	0.870		

(c) $Pr_2Ni_{1-x}M_xGa_{0.05}O_4$

Compounds	Tolerance No.	Compounds	Tolerance No.
$Pr_2Ni_{0.9}Cu_{0.1}Ga_{0.05}O_4$	0.855	$Pr_2Ni_{0.7}Zn_{0.3}Ga_{0.05}O_4$	0.851
$Pr_2Ni_{0.85}Cu_{0.15}Ga_{0.05}O_4$	0.855	$Pr_2Ni_{0.9}In_{0.1}Ga_{0.05}O_4$	0.853
$Pr_2Ni_{0.7}Cu_{0.3}Ga_{0.05}O_4$	0.852	$Pr_2Ni_{0.8}In_{0.2}Ga_{0.05}O_4$	0.848
$Pr_2Ni_{0.9}Co_{0.1}Ga_{0.05}O_4$	0.855	$Pr_2Ni_{0.7}In_{0.3}Ga_{0.05}O_4$	0.844
$Pr_2Ni_{0.8}Co_{0.2}Ga_{0.05}O_4$	0.852	$Pr_2Ni_{0.9}Mg_{0.1}Ga_{0.05}O_4$	0.856
$Pr_2Ni_{0.7}Co_{0.3}Ga_{0.05}O_4$	0.850	$Pr_2Ni_{0.8}Mg_{0.2}Ga_{0.05}O_4$	0.855
$Pr_2Ni_{0.9}Zn_{0.1}Ga_{0.05}O_4$	0.855	$Pr_2Ni_{0.7}Mg_{0.3}Ga_{0.05}O_4$	0.853
$Pr_2Ni_{0.8}Zn_{0.2}Ga_{0.05}O_4$	0.853		

The perovskite structure is stable in the range $0.75 < t < 1.0$. The closer the t is to unity, the greater is the stability of the perovskite structure, whereas greater declinations from unity give distorted unit cells. Pr_2NiO_4 had tolerance number 0.873 therefore it is able to form the perovskite structure. However, these perovskites had tolerance number less than 0.95, which meant that they all should not have a cubic structure. Deviations from the ideal structure are well known as orthorhombic, rhombohedral, tetragonal, monoclinic and triclinic symmetry. The tolerance number for substitution of the B-site cation is close to the value of Pr_2NiO_4 therefore the structure of metal–doped Pr_2NiO_4 should be orthorhombic.

3.3 Characterization of the perovskite compounds

As–synthesized powder was calcined to remove residual water and other impurities. In case of sintering process, the effect of heat treatment is related to improve crystallized structure and the fusing of particles to increase the density of the perovskite disc and eliminate the pores.

The structure of synthesized perovskite compounds were characterized by XRD and the surface morphology by SEM.

3.3.1 X-ray diffraction (XRD)

XRD was used to indicate the formation of the perovskite-type phase with either a K_2NiF_4 or distorted K_2NiF_4 structure. The phase formations of perovskites were characterized after calcinations and sintering. The diffraction peaks of perovskites were observed within 2θ in the range of 20 to 70°.

3.3.1.1 Phase formation of Pr_2NiO_4

The Pr_2NiO_4 calcined powder and disc were characterized by XRD. The XRD patterns were illustrated in Figure 3.1.
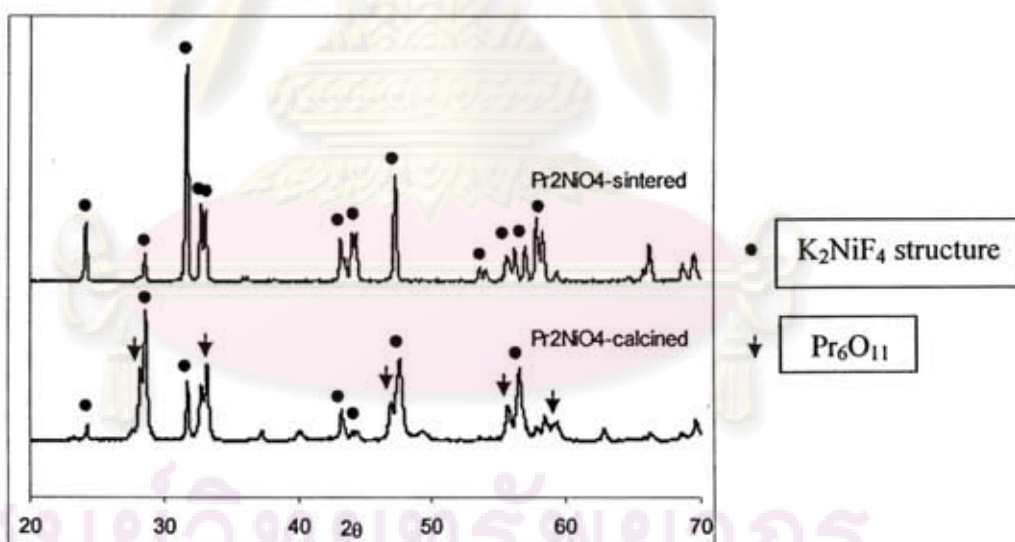
Figure 3.1 XRD pattern of Pr_2NiO_4

(1) Pr_2NiO_4 powder after calcined at 800°C for 6 hrs.

(2) Pr_2NiO_4 disc after sintered at 1300°C for 6 hrs.

The calcined powder exhibited the Pr_2NiO_4 diffraction lines with the existence of secondary phase (Pr_6O_{11}) (PDF 42-1121) [37] at 2θ of 28, 32, 46, 55 and 58. Afterwards, the calcined powder was uniaxially pressed into disks, and then followed by sintering at 1300°C for 6 h. It is noted that all the diffraction peaks can be assigned to that of Pr_2NiO_4 (PDF 86-0870). It showed the formation of single phase with orthorhombic K_2NiF_4-type structure. The secondary phase disappeared after Pr_2NiO_4 disc was sintered.

In this study, the effects of the dopant (Cu, Co, Zn, In and Mg) at Ni-site of Pr_2NiO_4 were investigated.

3.3.1.2 Phase formation of $Pr_2Ni_{1-x}M_xO_4$ (M = Cu, Co, Zn, In, Mg and x = 0.1-0.3)

A. $Pr_2Ni_{1-x}Cu_xO_4$ (x=0.1, 0.15, 0.3)

The structures of $Pr_2Ni_{1-x}M_xO_4$ (M = Cu, Co, Zn, In, Mg and x = 0.1-0.3) after sintering at 1573 K were analyzed by XRD. XRD patterns of Pr_2NiO_4 doped with Cu at Ni site revealed the main phase of K_2NiF_4-type structure. Secondary phase formation (marked with ↘) was also observed (Pr_6O_{11}) at $2\theta=28°$. It is seen that the amount of the Pr_6O_{11} phase increased with the increasing amount of metal (Cu: 0.1, 0.15, 0.3) substituted at Ni site (see Figure 3.2). From Shannon's tables the effective ionic radius for Cu^{2+} in octahedral coordination is 0.87 Å, which is close to the ionic radius for Ni^{2+} in the same coordination (0.83 Å). When compared with Pr_2NiO_4, substitution of nickel by copper in B-site of Pr_2NiO_4 induce a little slightly shift to lower angle of 2θ.
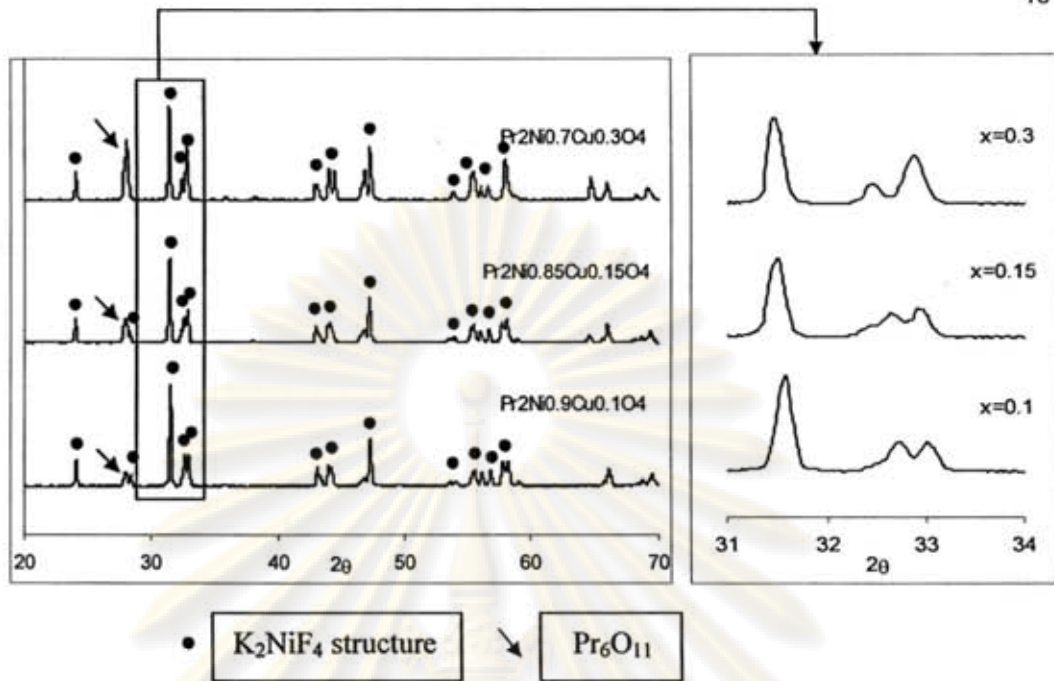
Figure 3.2 XRD patterns of $Pr_2Ni_{1-x}Cu_xO_4$ (x=0.1, 0.15, 0.3) disc.

With increasing of Cu, the pattern peaks shifted gradually to the low angle corresponding to the lattice expansion. It is due to the ionic radius of Cu^{2+} which substituted is somewhat larger than that of Ni^{2+}.

B. $Pr_2Ni_{1-x}Co_xO_4$ (x=0.1, 0.2, 0.3)

For $Pr_2Ni_{1-x}Co_xO_4$ (x=0.1, 0.2, 0.3), it was found that $Pr_2Ni_{1-x}Co_xO_4$ series have K_2NiF_4-type structure but trace of secondary phase still remained after sintering. The main peak of secondary phase as Pr_6O_{11} (2θ=28°) was observed and the amount of the Pr_6O_{11} phase increased with the increasing amount of metal (Co: 0.1, 0.2, 0.3) doped at Ni site (see Figure 3.3). The substitution of Co ion for ion in B-site of Pr_2NiO_4, the oxidation number of Co is regarded as mixed valence of +2 and +3 and Ni also seem to be +2. Therefore the addition of oxygen due to the electroneutrality rule and Pr_6O_{11} amount were increased. The ionic radius of Co^{2+} is similar to ionic radius of Ni^{2+} ($r_{Co^{2+}}$ = 0.89 Å, $r_{Ni^{2+}}$ = 0.83 Å), the substitution of Co^{2+} for Ni^{2+} in B-site of Pr_2NiO_4 induce a little slightly shift to lower angle of 2θ and slightly expansion of lattice crystal.
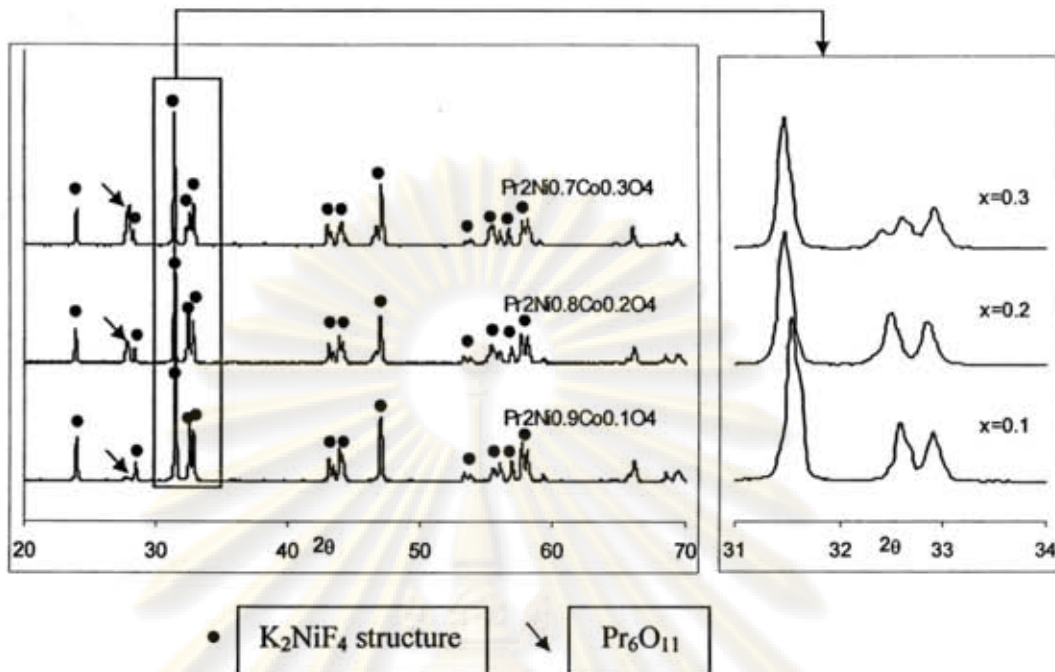
Figure 3.3 XRD patterns of $Pr_2Ni_{1-x}Co_xO_4$ (x=0.1, 0.2, 0.3) disc.

C. $Pr_2Ni_{1-x}Zn_xO_4$ (x=0.1, 0.2, 0.3)

From the XRD patterns in Figure 3.4, it is demonstrated that the perovskite phase of $Pr_2Ni_{1-x}Zn_xO_4$ (x=0.1, 0.2, 0.3) has orthorhombic structure and Pr_6O_{11} (impurity) phase is observed at $2\theta=28°$. The crystal structures of $Pr_2Ni_{1-x}Zn_xO_4$ did not change after doped with Zn. For $Pr_2Ni_{1-x}Zn_xO_4$ with x = 0.2-0.3, all peaks slightly shifted toward lower angles when the amounts of Zn content increased. Generally, the replacement of Ni^{2+} ($r_{Ni^{2+}}$ = 0.83 Å) with the larger cation, Zn^{2+} ($r_{Zn^{2+}}$ = 0.88 Å) will reduce the 2θ degree and induce a lattice expansion.
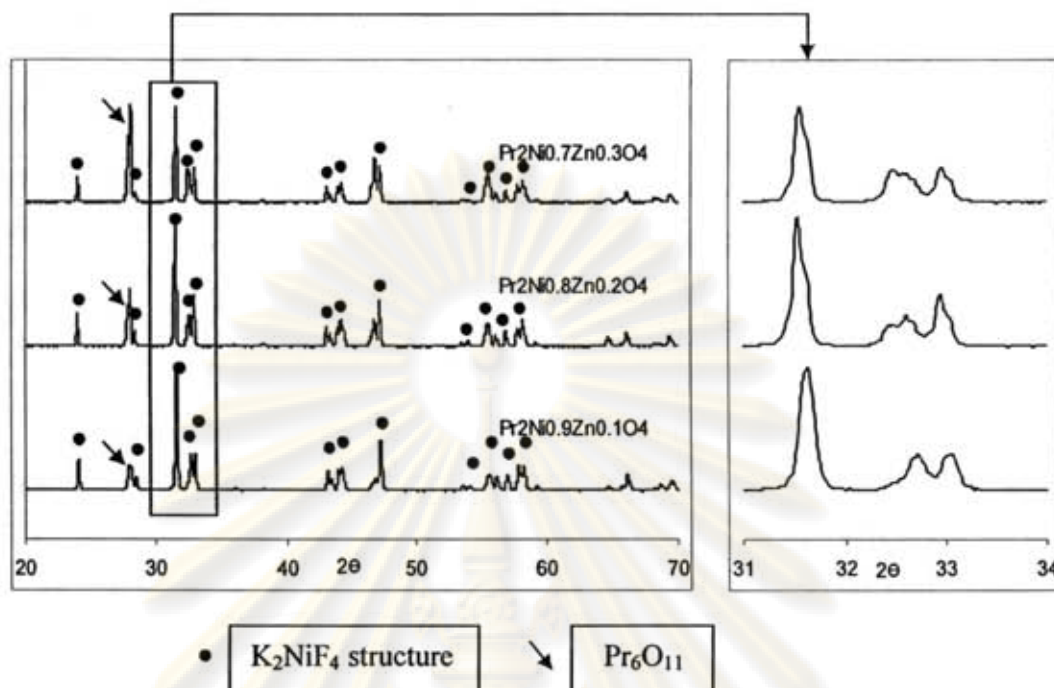
Figure 3.4 XRD patterns of $Pr_2Ni_{1-x}Zn_xO_4$ (x=0.1, 0.2, 0.3) disc.

D. $Pr_2Ni_{1-x}In_xO_4$ (x=0.1, 0.2, 0.3)

Similar to the previous result, in the case of $Pr_2Ni_{1-x}In_xO_4$ x=0.1, 0.2, 0.3), the disc exhibited orthorhombic structure and Pr_6O_{11} (impurity) phase at $2\theta=28°$. The substitution of In ion for ion in B-site of Pr_2NiO_4, the oxidation number of In is +3 and Ni also seem to be +2. The charge imbalance caused by a replacement of Ni^{2+} by In^{3+}. It was compensated by an addition of oxide ion in the lattice and Pr_6O_{11} amount were increased (see Figure 3.5).
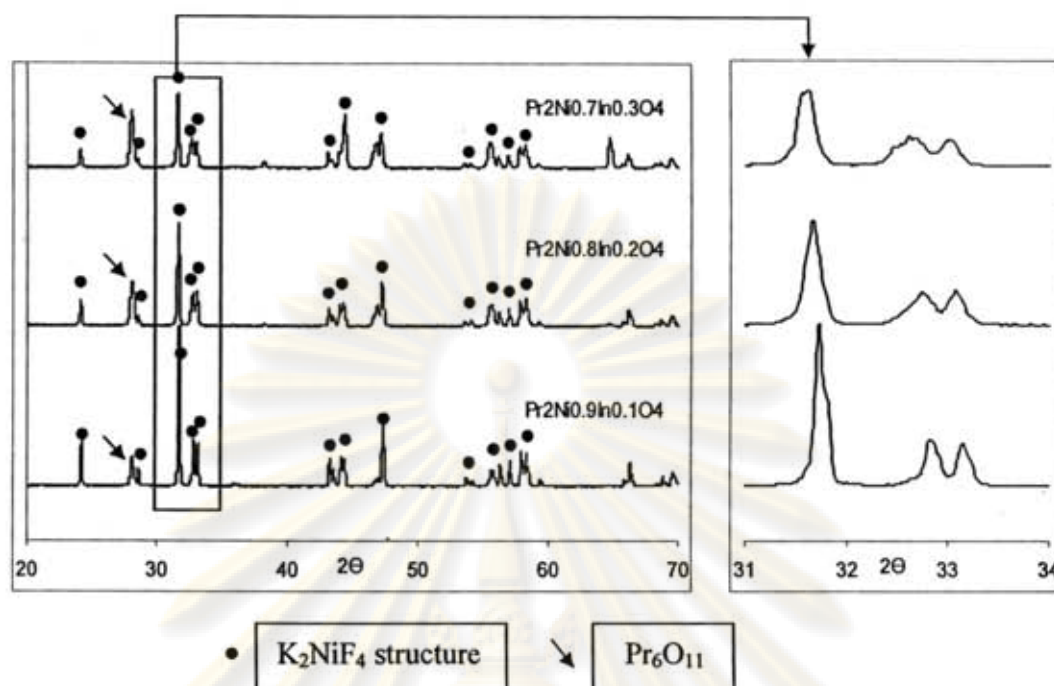
Figure 3.5 XRD patterns of $Pr_2Ni_{1-x}In_xO_4$(x=0.1, 0.2, 0.3) disc.

E. $Pr_2Ni_{1-x}Mg_xO_4$ (x=0.1, 0.2, 0.3)

The XRD patterns of $Pr_2Ni_{1-x}Mg_xO_4$ membranes with various Mg contents were shown in Figure 3.6. For $Pr_2Ni_{0.9}Mg_{0.1}O_4$, it is noted that the diffraction peaks can be assigned to the K_2NiF_4 structure. The main peak of secondary phase as Pr_6O_{11} (2θ=28°) was still detected. When Mg substitution was more than 0.1, the X-ray pattern displays not only some diffraction lines of the Pr_2NiO_4 perovskite but also those of Pr_6O_{11} and MgO. This is due to the fact that the complete structure was not obtained. Therefore, it is considered that the optimum amount of Mg for Ni site is around 10 mol%.
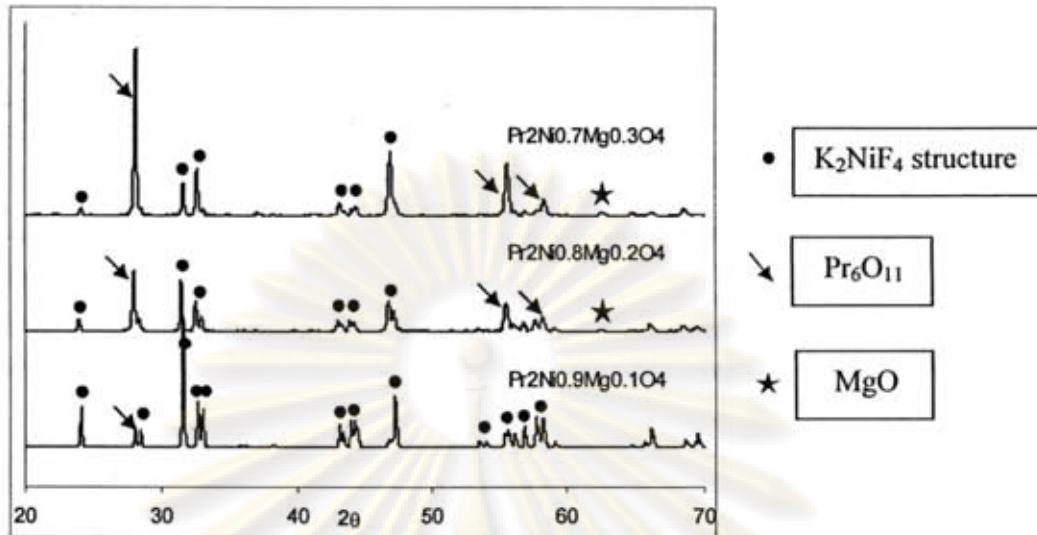
Figure 3.6 XRD patterns of $Pr_2Ni_{1-x}Mg_xO_4$ (x=0.1, 0.2, 0.3) disc.

From XRD analyses, the results of crystalline phase analysis of $Pr_2Ni_{1-x}M_xO_4$ (M = Cu, Co, Mg, Zn, In and x = 0.1-0.3) are summarized in Table 3.2. All compositions of the system $Pr_2Ni_{1-x}M_xO_4$ except $Pr_2Ni_{1-x}Mg_xO_4$ (x= 0.2, 0.3) prepared by the modified citrate method showed the existence of K_2NiF_4 phase and orthorhombic structure.

It should be noted that Pr_6O_{11} phase appeared only on the surface and can be polished before application. For example $Pr_2Ni_{0.85}Cu_{0.15}O_4$ after polished was shown in Figure 3.7.
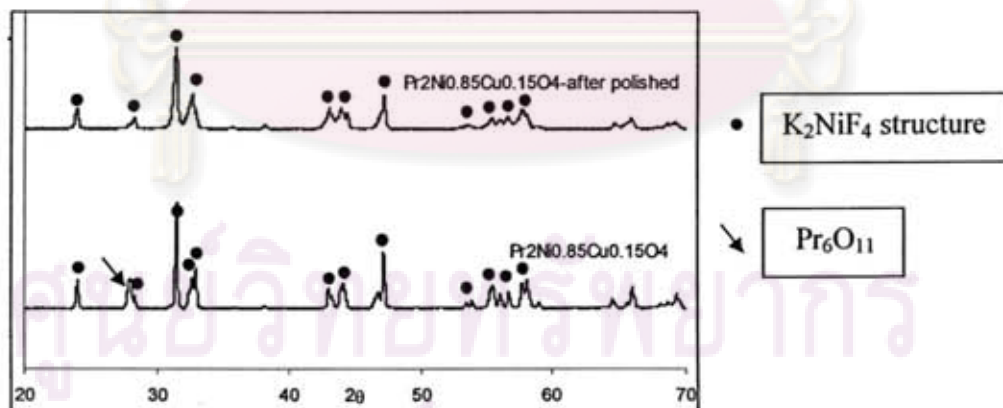
Figure 3.7 XRD patterns of $Pr_2Ni_{0.85}Mg_{0.15}O_4$ disc.

(1) $Pr_2Ni_{0.85}Mg_{0.15}O_4$ disc after sintered at 1300°C for 6 hrs.

(2) $Pr_2Ni_{0.85}Mg_{0.15}O_4$ disc after sintered at 1300°C for 6 hrs and polished.

Table 3.2 XRD analyses of sintered discs of $Pr_2Ni_{1-x}M_xO_4$ (M = Cu, Co, Mg, Zn, In and x = 0.1-0.3).

chemical compound $Pr_2Ni_{1-x}M_xO_4$		Crystal system	phase
Metal at B-site	x		
Cu	0.1	orthorhombic	$K_2NiF_4 + Pr_6O_{11}$
	0.15	orthorhombic	$K_2NiF_4 + Pr_6O_{11}$
	0.3	orthorhombic	$K_2NiF_4 + Pr_6O_{11}$
Co	0.1	orthorhombic	$K_2NiF_4 + Pr_6O_{11}$
	0.2	orthorhombic	$K_2NiF_4 + Pr_6O_{11}$
	0.3	orthorhombic	$K_2NiF_4 + Pr_6O_{11}$
Zn	0.1	orthorhombic	$K_2NiF_4 + Pr_6O_{11}$
	0.2	orthorhombic	$K_2NiF_4 + Pr_6O_{11}$
	0.3	orthorhombic	$K_2NiF_4 + Pr_6O_{11}$
In	0.1	orthorhombic	$K_2NiF_4 + Pr_6O_{11}$
	0.2	orthorhombic	$K_2NiF_4 + Pr_6O_{11}$
	0.3	orthorhombic	$K_2NiF_4 + Pr_6O_{11}$
Mg	0.1	orthorhombic	$K_2NiF_4 + Pr_6O_{11}$
	0.2	–	$K_2NiF_4 + Pr_6O_{11} + MgO$
	0.3	–	$K_2NiF_4 + Pr_6O_{11} + MgO$

3.3.1.3 Phase formation of $Pr_2Ni_{1-x}M_xGa_{0.05}O_4$ and $Pr_2Ni_{1-x-0.05}M_xGa_{0.05}O_4$ (M = Cu, Co, Mg, Zn, In and x = 0.1-0.3)

Ishihara *et al.* [35] reported that Pr_2NiO_4 doped with Cu and Fe ions for Ni site exhibits the relatively high oxygen permeation rate. Doping second cation to Ni site is effective for improving the oxygen permeation rate and the trivalent cation seems to be effective for increasing the oxygen permeation rate. Among the examined cation, the highest oxygen permeation rate was obtained by doping 5 mol% Fe.

Therefore we are interested in exploring the effect of doping stoichiometrically and excess of Ga (second cation) to Ni site in $Pr_2Ni_{1-x}M_xO_4$ (M = Cu, Co, Zn, In; x = 0.1-0.3 and Mg; x = 0.1).

A. $Pr_2Ni_{1-x}Cu_xGa_{0.05}O_4$ and $Pr_2Ni_{1-x-0.05}Cu_xGa_{0.05}O_4$ (x = 0.1, 0.15, 0.3)

XRD patterns of perovskite discs in various compositions after sintered at 1,300°C, reveal the orthorhombic structure. The formation of Pr_6O_{11} was observed, which is recognized from the main peak at $2\theta=28°$. Because of the small ion size of Ga^{3+} ($r_{Ga^{3+}} = 0.76$ Å, $r_{Ni^{2+}} = 0.83$ Å), substituted for Ni^{2+} in B-site of $Pr_2Ni_{1-x}M_xO_4$ caused XRD peak shift slightly to higher angle of 2θ.

(1) x = 0.1

(2) x = 0.15

(3) x = 0.3

● K_2NiF_4 structure   ↘ Pr_6O_{11}
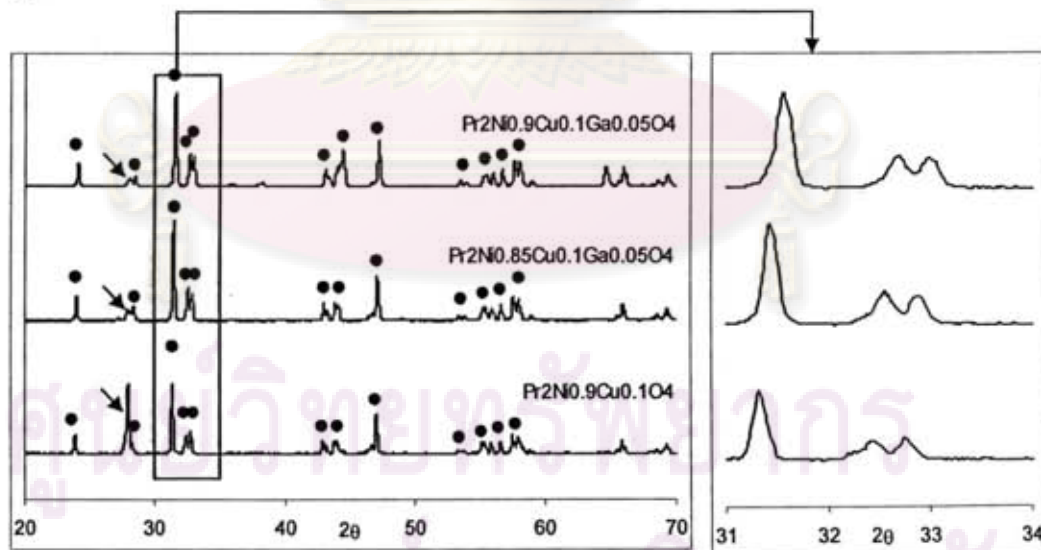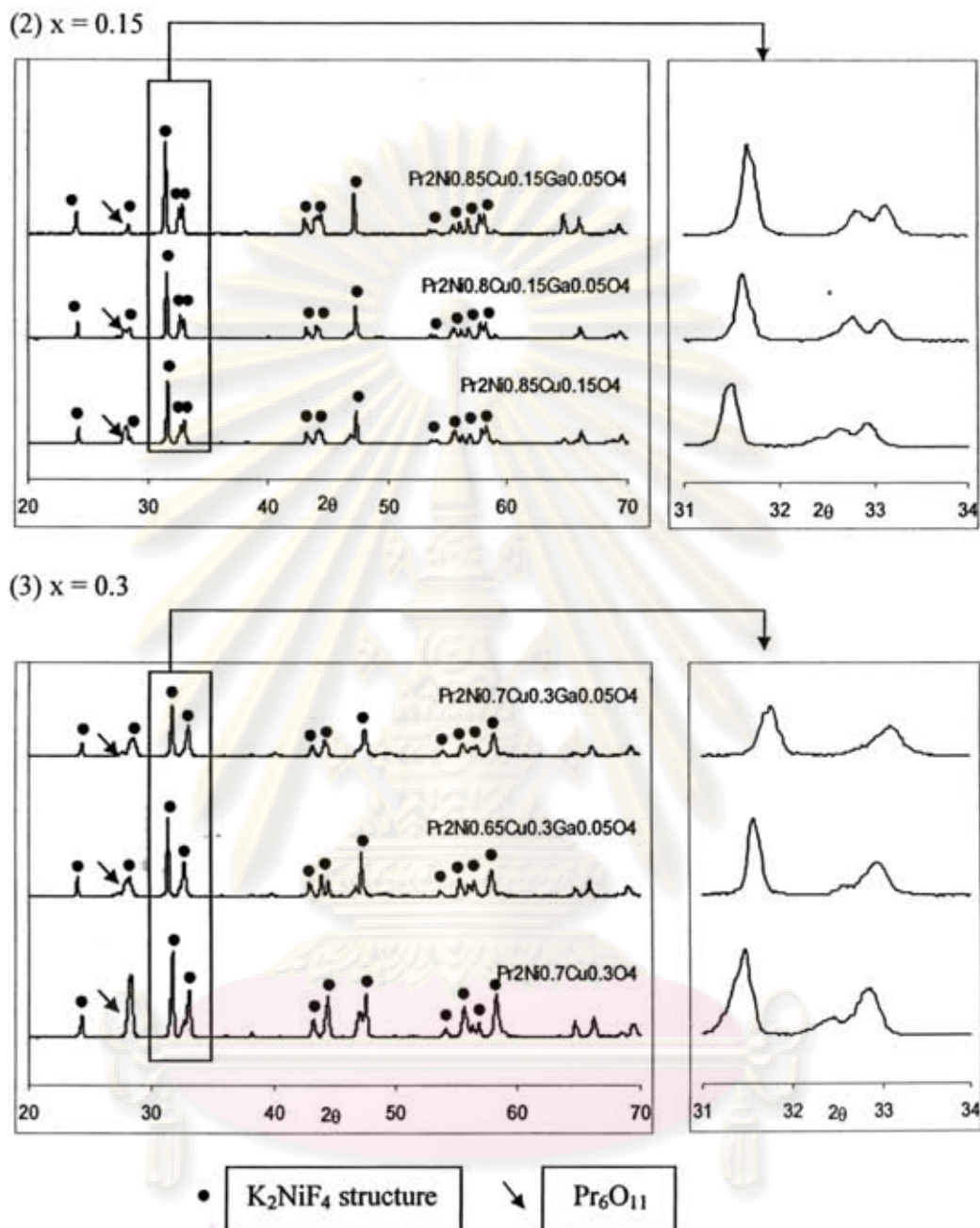
Figure 3.8 XRD patterns of $Pr_2Ni_{1-x}Cu_xO_4$, $Pr_2Ni_{1-x}Cu_xGa_{0.05}O_4$ and $Pr_2Ni_{1-x}Cu_xGa_{0.05}O_4$ compound. (1) x = 0.1 (2) x = 0.2 (3) x = 0.3

B. $Pr_2Ni_{1-x}Co_xGa_{0.05}O_4$ and $Pr_2Ni_{1-x-0.05}Co_xGa_{0.05}O_4$ (x = 0.1, 0.2, 0.3)

      Ga doped $Pr_2Ni_{0.9}Co_{0.1}O_4$, exhibited K_2NiF_4-type structure and the small impurity peak at $2\theta=28°$ were also found. The XRD peaks slightly shift to higher angle of 2Θ. It means that substitution of Ga^{3+} smaller size in B–site cause lattice shrinkage.

(1) x = 0.1
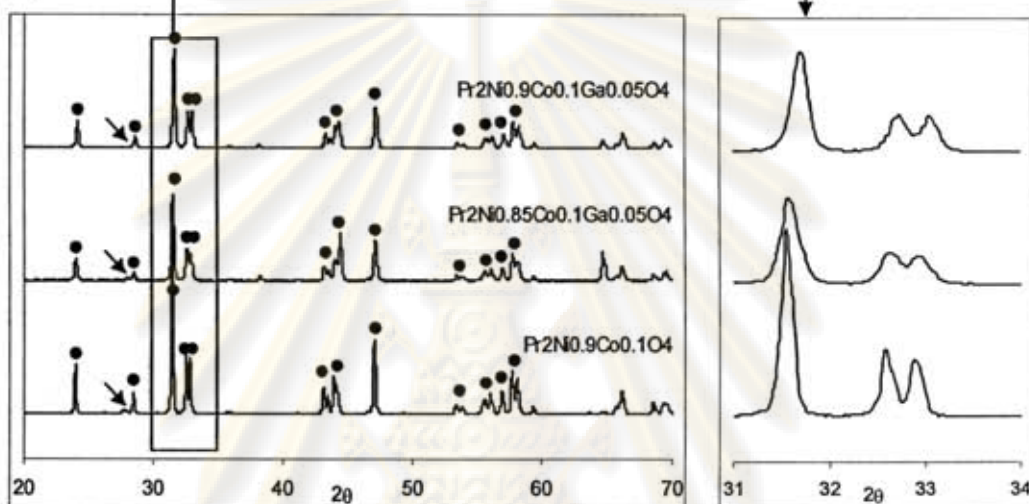
(2) x = 0.2
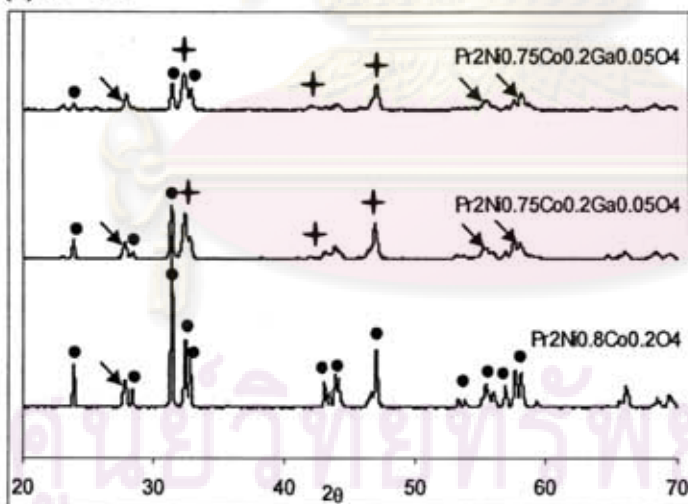
(3) x = 0.3
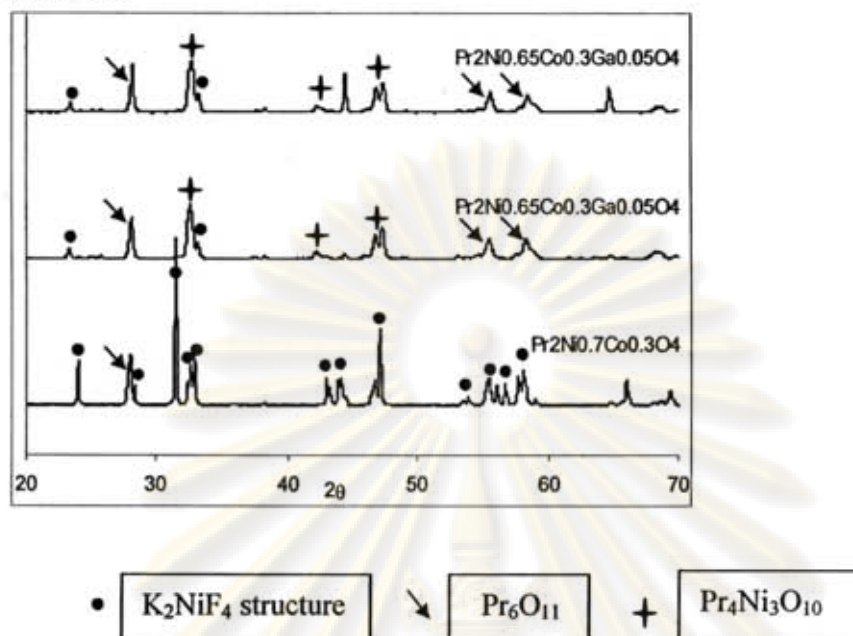
Figure 3.9   XRD patterns of $Pr_2Ni_{1-x}Co_xO_4$, $Pr_2Ni_{1-x-0.05}Co_xGa_{0.05}O_4$ and
$Pr_2Ni_{1-x}Co_xGa_{0.05}O_4$ compound. (1) x = 0.1 (2) x = 0.2 (3) x = 0.3

XRD patterns of $Pr_2Ni_{1-x-0.05}Co_xGa_{0.05}O_4$ and $Pr_2Ni_{1-x}Co_xGa_{0.05}O_4$ (x=0.2, 0.3) display not only diffraction lines of the perovskite but also secondary phases of Pr_6O_{11} and $Pr_4Ni_3O_{10}$. It is suggested that addition of Ga^{3+} into B site caused the callapse of the Pr_2NiO_4 structure. It is concluded that Ga–doped $Pr_2Ni_{1-x}Co_xO_4$ (x=0.2, 0.3) were not obtained.

C. $Pr_2Ni_{1-x}M_xGa_{0.05}O_4$, $Pr_2Ni_{1-x-0.05}M_xGa_{0.05}O_4$ (M = Zn, In; x = 0.1, 0.2, 0.3 and M = Mg; x = 0.1)

From XRD patterns of Zn^{2+}, In^{3+} and Mg^{2+} ions content, XRD patterns of $Pr_2Ni_{1-x-0.05}M_xGa_{0.05}O_4$ and $Pr_2Ni_{1-x}M_xGa_{0.05}O_4$ show the similar result with Ga doped $Pr_2Ni_{1-x}Cu_xO_4$. All patterns reveal the orthorhombic structure. The formation of Pr_6O_{11} was observed, which is recognized from the main peak at $2\theta=28°$, the introduction of Ga^{3+} ($r_{Ga^{3+}} = 0.76$ Å) into Ni site cause the somewhat shrinkage of the lattice therefore XRD peak shift to higher angle.

From XRD analyses, the results of crystalline phase analysis of Ga doped $Pr_2Ni_{1-x}M_xO_4$ (M = Cu, Co, Zn, In; x = 0.1-0.3 and Mg; x = 0.1) are

summarized in Table 3.4. All compositions of the system Ga doped $Pr_2Ni_{1-x}M_xO_4$ except $Pr_2Ni_{1-x}Co_xO_4$ (x = 0.2, 0.3) showed the existence of K_2NiF_4 phase with orthorhombic symmetry.

Table 3.3 XRD analyses of sintered discs of Ga doped $Pr_2Ni_{1-x}M_xO_4$ (M = Cu, Co, Zn, In; x = 0.1-0.3 and Mg; x = 0.1).

chemical compound		Synthesis result of Ga doped $Pr_2Ni_{1-x}M_xO_4$		Crystal system	phase
Metal at B-site	x	Stoichio metry	nonstoichio metry		
Cu	0.1	√	√	orthorhombic	$K_2NiF_4 + Pr_6O_{11}$
	0.15	√	√	orthorhombic	$K_2NiF_4 + Pr_6O_{11}$
	0.3	√	√	orthorhombic	$K_2NiF_4 + Pr_6O_{11}$
Co	0.1	√	√	orthorhombic	$K_2NiF_4 + Pr_6O_{11}$
	0.2	×	×	–	$K_2NiF_4 + Pr_4Ni_3O_{10} + Pr_6O_{11}$
	0.3	×	×	–	$K_2NiF_4 + Pr_4Ni_3O_{10} + Pr_6O_{11}$
Zn	0.1	√	√	orthorhombic	$K_2NiF_4 + Pr_6O_{11}$
	0.2	√	√	orthorhombic	$K_2NiF_4 + Pr_6O_{11}$
	0.3	√	√	orthorhombic	$K_2NiF_4 + Pr_6O_{11}$
In	0.1	√	√	orthorhombic	$K_2NiF_4 + Pr_6O_{11}$
	0.2	√	√	orthorhombic	$K_2NiF_4 + Pr_6O_{11}$
	0.3	√	√	orthorhombic	$K_2NiF_4 + Pr_6O_{11}$
Mg	0.1	√	√	orthorhombic	$K_2NiF_4 + Pr_6O_{11}$

√ – complete phase of perovskite was obtained.

× – show in perovskite was not obtained.

3.3.2 Scanning electron microscope (SEM) and density

The morphologies of perovskite disc were obtained by SEM technique. The effect of doping Cu, Co, Zn, In, Mg and Ga to Ni-site in Pr_2NiO_4 were compared in the term of grain size, impurity and porosity. Densities of samples were determined by the Archimedes immersion method using water as a medium.

3.3.2.1 The morphology of Pr_2NiO_4

The surface morphology of Pr_2NiO_4 disc after sintered at 1300°C for 6 hours was shown in Figure 3.9.

Figure 3.10 Surface morphology of Pr_2NiO_4 disc.

SEM micrograph of Pr_2NiO_4 disc exhibited high density and homogenous phase. The rough grain size of perovskite disc are in the size range of 3–5 µm. These particle size data were directly estimated from SEM micrographs. The density of Pr_2NiO_4 is 7.202 g.cm^3 and relative density is 98.2%.

3.3.2.2 The morphologies of $Pr_2Ni_{1-x}Cu_xO_4$, $Pr_2Ni_{1-x-0.05}Cu_xGa_{0.05}O_4$ and $Pr_2Ni_{1-x}Cu_xGa_{0.05}O_4$ (x = 0.1, 0.15, 0.3)

Form Figure 3.10, the surface of $Pr_2Ni_{1-x}Cu_xO_4$ disc looked uniform, crack-free and high density. Therefore the Cu contents in Pr_2NiO_4 system did not affect on morphology of disc after sintering.

Figure 3.11 Surface morphology of $Pr_2Ni_{1-x}Cu_xO_4$ (x = 0.1, 0.15, 0.3) discs.

The grain size slightly increased with the increasing content of Cu. The average grain size for the $Pr_2Ni_{0.9}Cu_{0.1}O_4$, $Pr_2Ni_{0.85}Cu_{0.15}O_4$, $Pr_2Ni_{0.7}Cu_{0.3}O_4$ discs are about 3μm, 5 μm and 7 μm, respectively. As observed previously [43–44] the increase in particle size with the doping level is a result of a change in the melting point of the samples. Doping with copper decreases melting points of the materials, this effect results in an enhanced grain growth. With further increasing of the Cu^{2+} content to 0.30, an increase in the amount of the Pr_6O_{11} packed plate-like grains was observed which agreed with the XRD result.

The densities of $Pr_2Ni_{1-x}Cu_xO_4$ with various amounts of Cu were listed in Table 3.4. $Pr_2Ni_{0.9}Cu_{0.1}O_4$ has the highest density.

Table 3.4 Density of $Pr_2Ni_{1-x}Cu_xO_4$ discs when x = 0.1, 0.15 and 0.3.

$Pr_2Ni_{1-x}Cu_xO_4$ disc	Density/$g.cm^3$
$Pr_2Ni_{0.9}Cu_{0.1}O_4$	7.143
$Pr_2Ni_{0.85}Cu_{0.15}O_4$	7.037
$Pr_2Ni_{0.7}Cu_{0.3}O_4$	6.819
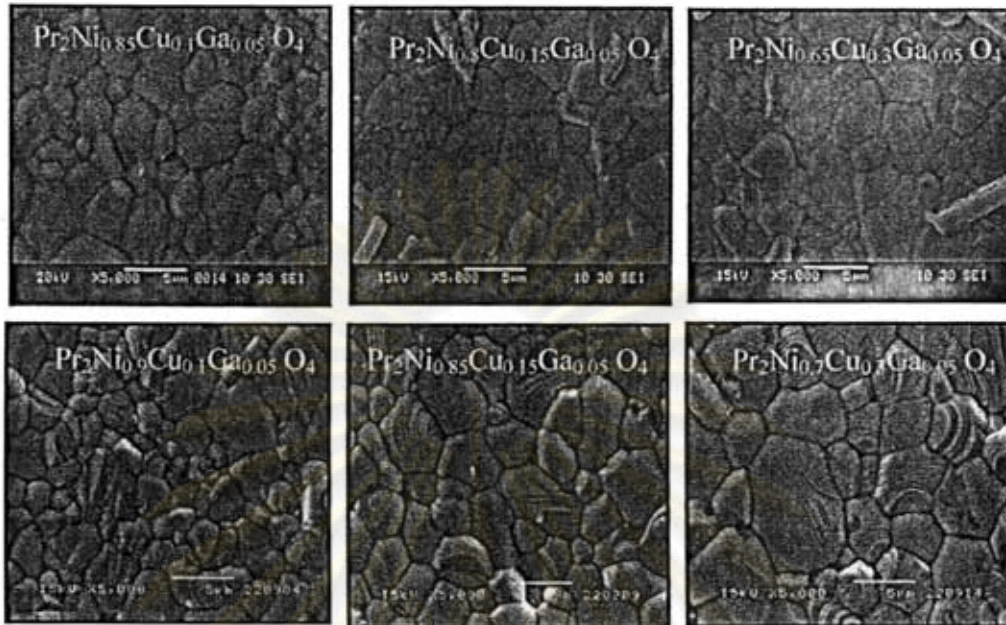
Figure 3.12 Surface morphology of $Pr_2Ni_{1-x-0.05}Cu_xGa_{0.05}O_4$ and $Pr_2Ni_{1-x}Cu_xGa_{0.05}O_4$ (x = 0.1, 0.15, 0.3) discs.

SEM micrograph of Ga doped $Pr_2Ni_{1-x}Cu_xO_4$ shows a microstructure with no porosity and the packed grain sizes are in the size range of 3–7 μm.

Density of $Pr_2Ni_{1-x-0.05}Cu_xGa_{0.05}O_4$, $Pr_2Ni_{1-x}Cu_xGa_{0.05}O_4$ discs determined by the Archimedes method was listed in Table 3.5. It can be suggested that Ga contents in $Pr_2Ni_{1-x}Cu_xO_4$ did not affect the density of $Pr_2Ni_{1-x}Cu_xO_4$.

Table 3.5 Density of $Pr_2Ni_{1-x-0.05}Cu_xGa_{0.05}O_4$, $Pr_2Ni_{1-x}Cu_xGa_{0.05}O_4$ discs when x = 0.1, 0.15 and 0.3.

$Pr_2Ni_{1-x-0.05}Cu_xGa_{0.05}O_4$ disc	Density/$g.cm^3$	$Pr_2Ni_{1-x}Cu_xGa_{0.05}O_4$ disc	Density/$g.cm^3$
$Pr_2Ni_{0.85}Cu_{0.1}Ga_{0.05}O_4$	7.322	$Pr_2Ni_{0.9}Cu_{0.1}Ga_{0.05}O_4$	7.119
$Pr_2Ni_{0.8}Cu_{0.15}Ga_{0.05}O_4$	7.043	$Pr_2Ni_{0.85}Cu_{0.15}Ga_{0.05}O_4$	6.935
$Pr_2Ni_{0.65}Cu_{0.3}Ga_{0.05}O_4$	6.942	$Pr_2Ni_{0.7}Cu_{0.3}Ga_{0.05}O_4$	6.698

3.3.2.3 The morphologies of $Pr_2Ni_{1-x}Co_xO_4$ (x = 0.1, 0.2, 0.3), $Pr_2Ni_{0.85}Co_{0.1}Ga_{0.05}O_4$ and $Pr_2Ni_{0.9}Co_{0.1}Ga_{0.05}O_4$

The surface of $Pr_2Ni_{1-x}Co_xO_4$ discs were investigated by SEM technique shown in Figure 3.13.

Figure 3.13 Surface morphology of $Pr_2Ni_{1-x}Co_xO_4$ (x = 0.1, 0.2, 0.3) discs.

The slight increase of the grain size from about 3 μm to about 6 nm was observed when the amount of Co^{2+} increased from 0.1 to 0.3. The increasing amount of Co in the structure reduced the melting point of the materials. Therefore the fusion of grain easily occurred. The SEM micrographs showed well-sintered dense ceramics.

The densities of $Pr_2Ni_{1-x}Co_xO_4$ with various amounts of Cu were listed in Table 3.6. Co contents in $Pr_2Ni_{1-x}Co_xO_4$ did not affect the density of $Pr_2Ni_{1-x}Co_xO_4$.

Table 3.6 Density of $Pr_2Ni_{1-x}Co_xO_4$ discs when x = 0.1, 0.2 and 0.3.

$Pr_2Ni_{1-x}Co_xO_4$ disc	Density/g.cm^3
$Pr_2Ni_{0.9}Co_{0.1}O_4$	7.106
$Pr_2Ni_{0.8}Co_{0.2}O_4$	7.108
$Pr_2Ni_{0.7}Co_{0.3}O_4$	7.089
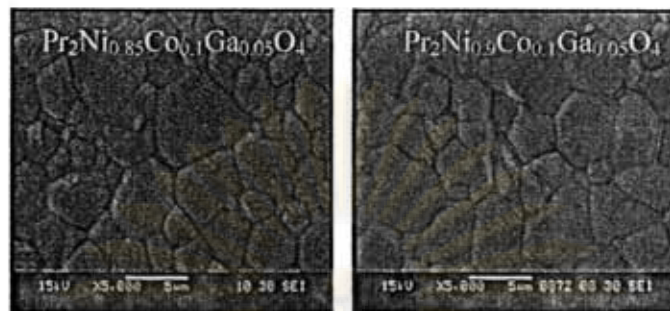
Figure 3.14 Surface morphology of $Pr_2Ni_{0.85}Co_{0.1}Ga_{0.05}O_4$ and $Pr_2Ni_{0.9}Co_{0.1}Ga_{0.05}O_4$ discs.

The SEM images of $Pr_2Ni_{0.85}Co_{0.1}Ga_{0.05}O_4$ and $Pr_2Ni_{0.9}Cu_{0.1}Ga_{0.05}O_4$ discs showed larger grain size. The ceramic is dense and the packed grains are in the size range of 3–7 μm.

Density of $Pr_2Ni_{0.85}Co_{0.1}Ga_{0.05}O_4$ and $Pr_2Ni_{0.9}Cu_{0.1}Ga_{0.05}O_4$ were listed in Table 3.7, it revealed that Ga contents in $Pr_2Ni_{1-x}Co_xO_4$ did not affect the density of disc.

Table 3.7 Density of $Pr_2Ni_{0.85}Co_{0.1}Ga_{0.05}O_4$ and $Pr_2Ni_{0.9}Co_{0.1}Ga_{0.05}O_4$ discs.

Ga doped $Pr_2Ni_{0.9}Co_{0.1}O_4$ disc	Density/$g.cm^3$
$Pr_2Ni_{0.85}Co_{0.1}Ga_{0.05}O_4$	7.249
$Pr_2Ni_{0.9}Co_{0.1}Ga_{0.05}O_4$	7.098

3.3.2.4 The morphologies of $Pr_2Ni_{1-x}Zn_xO_4$, $Pr_2Ni_{1-x-0.05}Zn_xGa_{0.05}O_4$ and $Pr_2Ni_{1-x}Zn_xGa_{0.05}O_4$ (x = 0.1, 0.2, 0.3)

The SEM micrographs of $Pr_2Ni_{1-x}Zn_xO_4$ with small grain size and dense microstructure were illustrated in Figure 3.15.
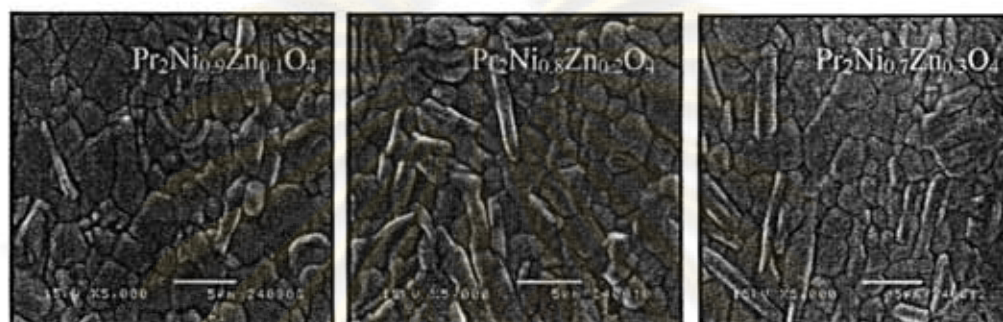
Figure 3.15 Surface morphology of $Pr_2Ni_{1-x}Zn_xO_4$ (x = 0.1, 0.2, 0.3) discs.

The estimation of Zn^{2+} grain size was found to be in the range of 2–4 µm, almost independently on composition. The average particle size of the Zn-containing samples is smaller than that of Pr_2NiO_4 (of about 3–5 µm). The residual Zn may distribute on the grain boundary which hinders the development of the grains of perovskite phase in the sintering process. With further increasing the Zn^{2+} content 0.10 to 0.30, Figure 3.14 shows an increase in the amount of the Pr_6O_{11} packed plate-like grains, which agrees with the XRD observation.

Table 3.8 shows the density of $Pr_2Ni_{1-x}Zn_xO_4$ discs when x = 0.1, 0.2 and 0.3. It is found that the density decreased with doped Zn in Pr_2NiO_4.

Table 3.8 Density of $Pr_2Ni_{1-x}Zn_xO_4$ discs when x = 0.1, 0.2 and 0.3.

$Pr_2Ni_{1-x}Zn_xO_4$ disc	Density/g.cm^3
$Pr_2Ni_{0.9}Zn_{0.1}O_4$	6.525
$Pr_2Ni_{0.8}Zn_{0.2}O_4$	6.590
$Pr_2Ni_{0.7}Zn_{0.3}O_4$	6.492
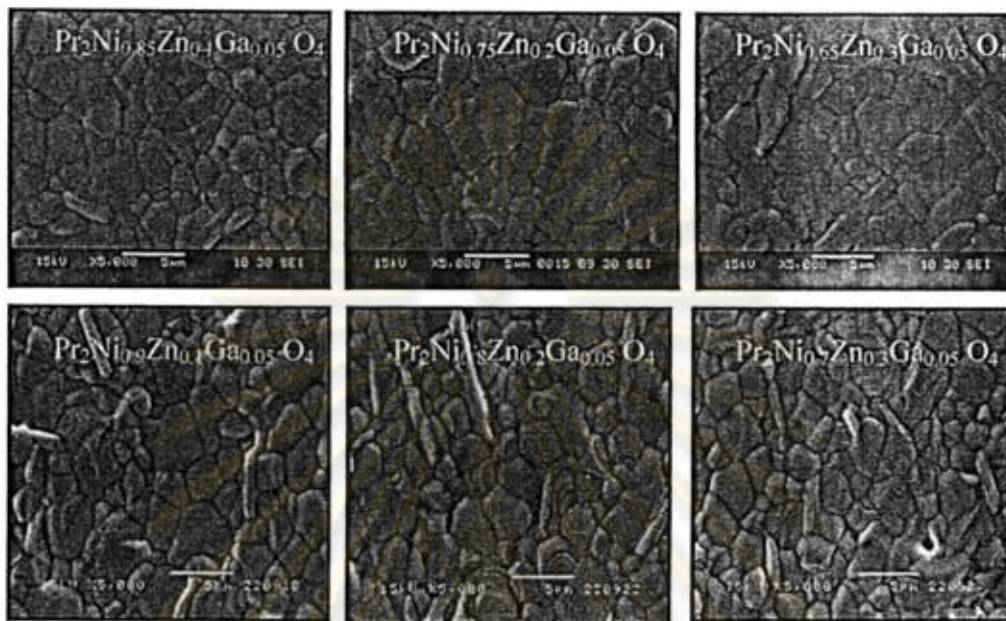
Figure 3.16 Surface morphology of $Pr_2Ni_{1-x-0.05}Zn_xGa_{0.05}O_4$ and $Pr_2Ni_{1-x}Zn_xGa_{0.05}O_4$ (x = 0.1, 0.2, 0.3) discs.

SEM micrographs of $Pr_2Ni_{1-x-0.05}Zn_xGa_{0.05}O_4$ and $Pr_2Ni_{1-x}Zn_xGa_{0.05}O_4$ (x = 0.1, 0.2, 0.3) show small grain size about 2–4 μm. Morphology of samples appeared crack-free and uniform.

The densities of $Pr_2Ni_{1-x}Cu_xO_4$ with various amounts of Zn were listed in Table 3.9.

Table 3.9 Density of $Pr_2Ni_{1-x-0.05}Zn_xGa_{0.05}O_4$ and $Pr_2Ni_{1-x}Zn_xGa_{0.05}O_4$ discs when x = 0.1, 0.2 and 0.3.

$Pr_2Ni_{1-x-0.05}Zn_xGa_{0.05}O_4$ disc	Density/g.cm^3	$Pr_2Ni_{1-x}Zn_xGa_{0.05}O_4$ disc	Density/g.cm^3
$Pr_2Ni_{0.85}Zn_{0.1}Ga_{0.05}O_4$	6.457	$Pr_2Ni_{0.9}Zn_{0.1}Ga_{0.05}O_4$	6.580
$Pr_2Ni_{0.75}Zn_{0.2}Ga_{0.05}O_4$	6.006	$Pr_2Ni_{0.8}Zn_{0.2}Ga_{0.05}O_4$	6.757
$Pr_2Ni_{0.65}Zn_{0.3}Ga_{0.05}O_4$	6.132	$Pr_2Ni_{0.7}Zn_{0.3}Ga_{0.05}O_4$	6.579

3.3.2.5 The morphologies of $Pr_2Ni_{1-x}In_xO_4$, $Pr_2Ni_{1-x-0.05}In_x$-$Ga_{0.05}O_4$ and $Pr_2Ni_{1-x}In_xGa_{0.05}O_4$ (x = 0.1, 0.2, 0.3)

Fig. 3.16 shows the SEM micrographs of $Pr_2Ni_{1-x}In_xO_4$ (x = 0.1, 0.2, 0.3) disc sintered at 1300 °C for 6 h.
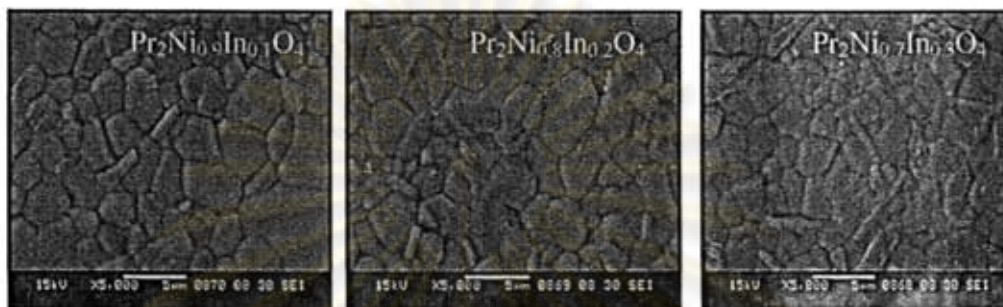
Figure 3.17 Surface morphology of $Pr_2Ni_{1-x}In_xO_4$ (x = 0.1, 0.2, 0.3) discs.

The observed morphology reveals that uniform, crack-free and high density. The grain size slightly decreased with an increasing content of In. The average grain size for the $Pr_2Ni_{0.9}In_{0.1}O_4$, $Pr_2Ni_{0.8}In_{0.2}O_4$, $Pr_2Ni_{0.7}In_{0.3}O_4$ disc are about 5 μm, 4 μm and 2 μm, respectively. As compared to $Pr_2Ni_{1-x}Cu_xO_4$ and $Pr_2Ni_{1-x}Co_x$-O_4, the increases of doped metal cation contents increase the melting point of the compounds. Therefore the fusion of grain difficultly occurred.

The densities of $Pr_2Ni_{1-x}In_xO_4$ with various amounts of In were listed in Table 3.10. $Pr_2Ni_{0.9}In_{0.1}O_4$ has highest density.

Table 3.10 Density of $Pr_2Ni_{1-x}In_xO_4$ discs when x = 0.1, 0.2 and 0.3.

$Pr_2Ni_{1-x}In_xO_4$ disc	Density/$g.cm^3$
$Pr_2Ni_{0.9}In_{0.1}O_4$	7.187
$Pr_2Ni_{0.8}In_{0.2}O_4$	6.601
$Pr_2Ni_{0.7}In_{0.3}O_4$	6.610
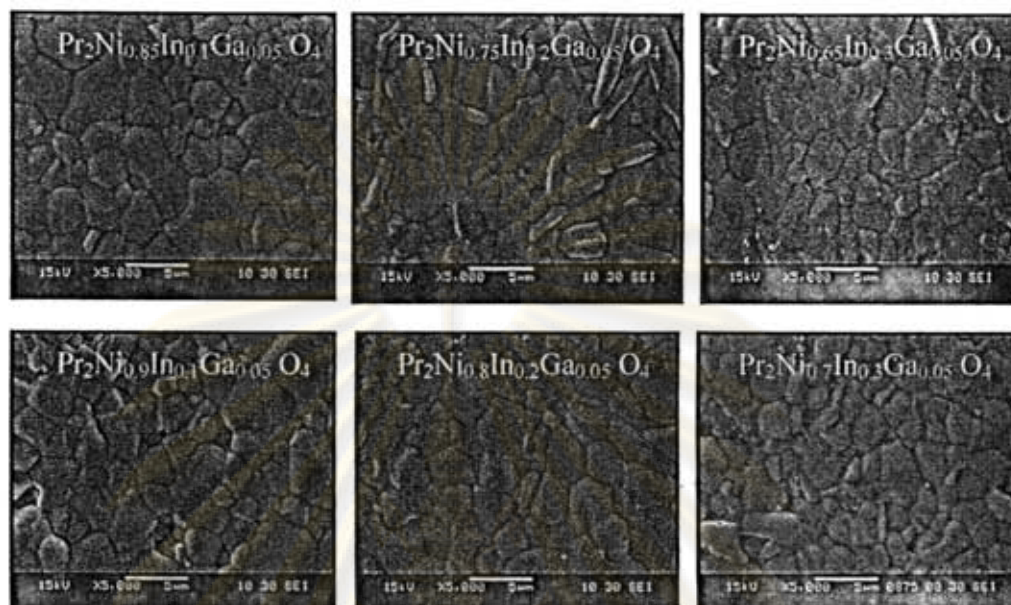
Figure 3.18 Surface morphology of $Pr_2Ni_{1-x-0.05}In_xGa_{0.05}O_4$ and $Pr_2Ni_{1-x}In_xGa_{0.05}O_4$ (x = 0.1, 0.2, 0.3) discs.

SEM observations of Ga doped $Pr_2Ni_{1-x}In_xO_4$ proved that dense materials have a same grain sizes as undoped Ga compositions. The ceramic has a close microstructure with low porosity.

Table 3.11 shows the density of Ga-doped $Pr_2Ni_{1-x}In_xO_4$ discs when x = 0.1, 0.2 and 0.3

Table 3.11 Density of $Pr_2Ni_{1-x-0.05}In_xGa_{0.05}O_4$ and $Pr_2Ni_{1-x}In_xGa_{0.05}O_4$ discs when x = 0.1, 0.2 and 0.3.

$Pr_2Ni_{1-x-0.05}In_xGa_{0.05}O_4$ disc	Density/$g.cm^3$	$Pr_2Ni_{1-x}In_xGa_{0.05}O_4$ disc	Density/$g.cm^3$
$Pr_2Ni_{0.85}In_{0.1}Ga_{0.05}O_4$	7.227	$Pr_2Ni_{0.9}In_{0.1}Ga_{0.05}O_4$	7.239
$Pr_2Ni_{0.75}In_{0.2}Ga_{0.05}O_4$	6.426	$Pr_2Ni_{0.8}In_{0.2}Ga_{0.05}O_4$	6.382
$Pr_2Ni_{0.65}In_{0.3}Ga_{0.05}O_4$	5.970	$Pr_2Ni_{0.7}In_{0.3}Ga_{0.05}O_4$	6.496

3.3.2.6 The morphologies of $Pr_2Ni_{1-x}Mg_xO_4(x = 0.1, 0.2, 0.3)$, $Pr_2Ni_{0.85}Mg_{0.1}Ga_{0.05}O_4$ and $Pr_2Ni_{0.9}Mg_{0.1}Ga_{0.05}O_4$

Figure 3.19 shows SEM pictures of $Pr_2Ni_{1-x}Mg_xO_4$ with $x = 0.1, 0.2$ and 0.3.
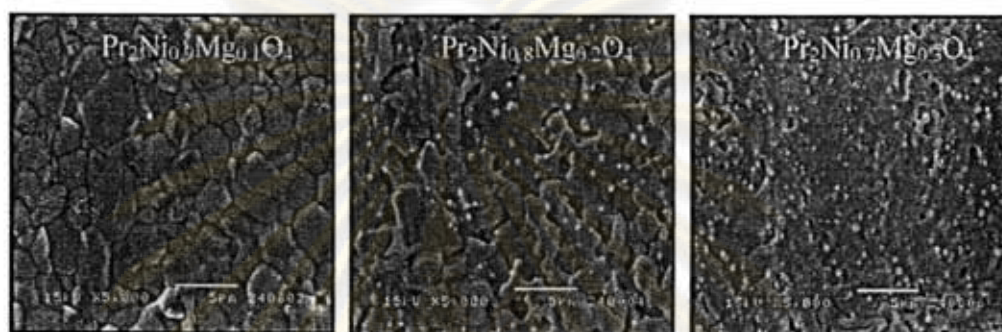
Figure 3.19 Surface morphology of $Pr_2Ni_{1-x}Mg_xO_4$ ($x = 0.1, 0.2, 0.3$) discs.

The morphology of $Pr_2Ni_{0.9}Mg_{0.1}O_4$ looked uniform, crack-free and high density, $Pr_2Ni_{0.8}Mg_{0.2}O_4$ and $Pr_2Ni_{0.7}Mg_{0.3}O_4$ membrane revealed large pores and impurity phase. The white dots scattered on the surface. It means that the Mg^{2+} ions 0.2 and 0.3 mole can not be doped into Pr_2NiO_4 which lead to the formation of secondary phases on the grain boundaries which prevent the grain growth. When comparing the XRD (Figure 3.6) and SEM (Figure 3.18) results, the limit of the Mg^{2+} solubility is determined to be within $x = 0.1$.

In addition, the large closed pores caused the decrease of the disc density. Therefore, the density of $Pr_2Ni_{1-x}Mg_xO_4$ gradually decreased with Mg contents, were listed in Table 3.12.

Table 3.12 Density of $Pr_2Ni_{1-x}Mg_xO_4$ discs when $x = 0.1, 0.2$ and 0.3.

$Pr_2Ni_{1-x}Mg_xO_4$ disc	Density/$g.cm^3$
$Pr_2Ni_{0.9}Mg_{0.1}O_4$	6.296
$Pr_2Ni_{0.8}Mg_{0.2}O_4$	4.717
$Pr_2Ni_{0.7}Mg_{0.3}O_4$	4.779

Figure 3.20 Surface morphology of $Pr_2Ni_{0.85}Mg_{0.1}Ga_{0.05}O_4$ and $Pr_2Ni_{0.9}Mg_{0.1}Ga_{0.05}O_4$ discs.

The average grain size for the Ga doped $Pr_2Ni_{0.9}Mg_{0.1}O_4$ ceramic samples are about 1-4 μm. However, the densities of $Pr_2Ni_{0.85}Mg_{0.1}Ga_{0.05}O_4$, $Pr_2Ni_{0.9}Mg_{0.1}Ga_{0.05}O_4$ discs are listed in Table 3.13.

Table 3.13 Density of $Pr_2Ni_{0.85}Mg_{0.1}Ga_{0.05}O_4$ and $Pr_2Ni_{0.9}Mg_{0.1}Ga_{0.05}O_4$ discs.

Ga doped $Pr_2Ni_{0.9}Mg_{0.1}O_4$ disc	Density/$g.cm^3$
$Pr_2Ni_{0.85}Mg_{0.1}Ga_{0.05}O_4$	6.471
$Pr_2Ni_{0.9}Mg_{0.1}Ga_{0.05}O_4$	6.265

3.3.3 Thermogravimetric analysis (TGA) method

All series of perovskite discs after sintered at 1,300°C except $Pr_2Ni_{1-x}Mg_xO_4$ (x = 0.2-0.3) and Ga doped $Pr_2Ni_{1-x}Co_xO_4$ (x = 0.2-0.3), were analyzed by thermogravimetric analysis (TGA), under nitrogen gas. The temperature was increased from room temperature to 900°C with heating rate of 20°C min^{-1}.

3.3.3.1 Thermal Analysis of Pr_2NiO_4

Figure 3.21 shows the weight loss of Pr_2NiO_4 sample (sintered at 1300°C) as a function of temperature upon heating process in nitrogen.
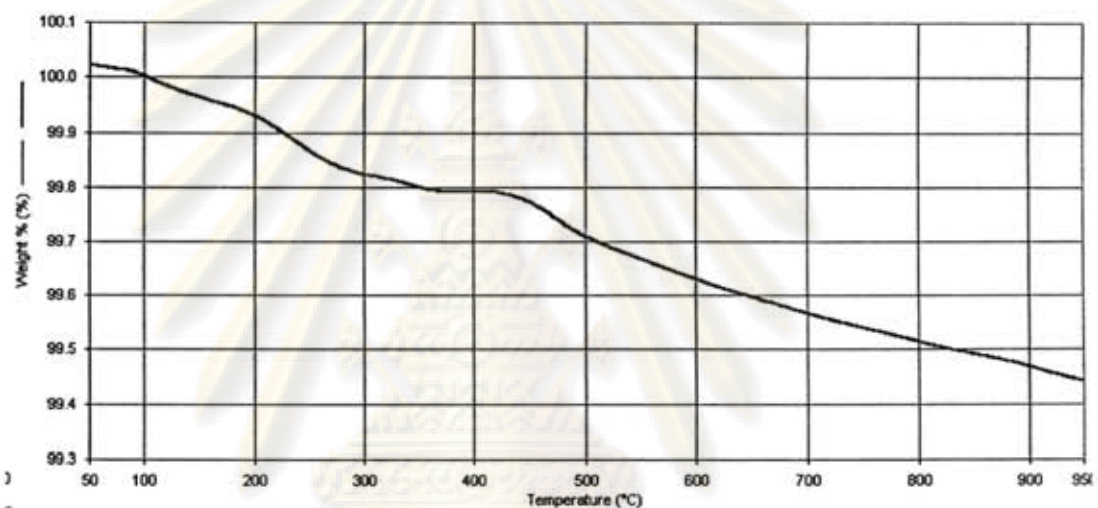
Figure 3.21 Relative weight loss of Pr_2NiO_4 as function of temperatures under N_2.

In the TGA profile, a slow weight loss from room temperature up to 100°C is observed which can be attributed to the loss of adsorbed water and carbon dioxide. Then the weight of sample decrease gradually from 100°C to 950°C. Manthiram *et al.* [36] found that the relative degree of oxygen loss from the lattice could be assessed with the TGA curves. The weight change corresponds to oxygen vacancy concentration, which related to oxygen desorption.

3.3.3.2 Thermal Analysis of $Pr_2Ni_{1-x}Cu_xO_4$, $Pr_2Ni_{1-x-0.05}Cu_x$- $Ga_{0.05}O_4$ and $Pr_2Ni_{1-x}Cu_xGa_{0.05}O_4$ (x = 0.1, 0.15, 0.3)

The weight losses for the $Pr_2Ni_{1-x}Cu_xO_4$ (x = 0.1, 0.15, 0.3) compounds are plotted versus temperature shown in Figure 3.22.
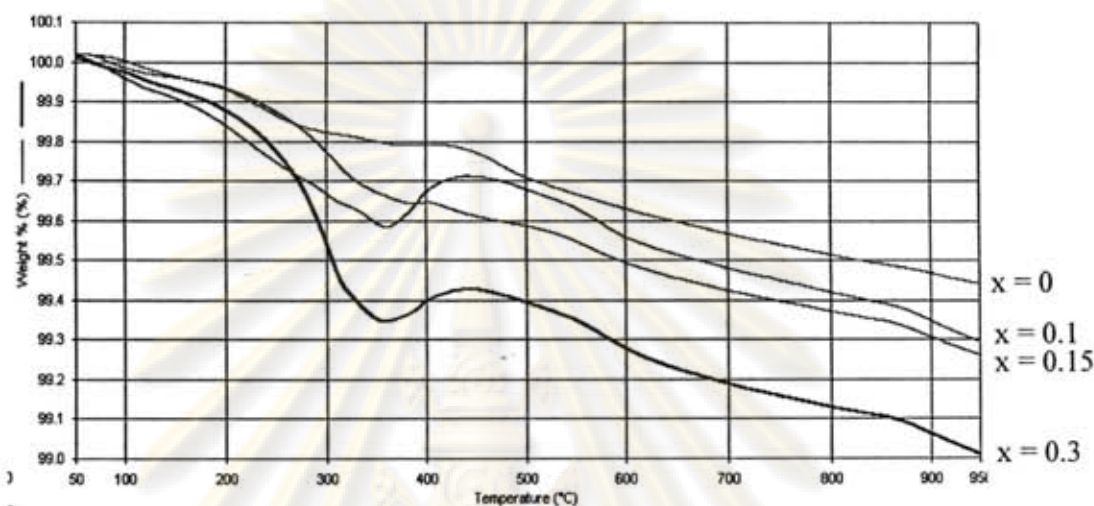
Figure 3.22 Relative weight loss of $Pr_2Ni_{1-x}Cu_xO_4$ as function of temperatures and Cu content under N_2.

From TGA curves, it is seen that all Cu composition of $Pr_2Ni_{1-x}Cu_xO_4$ have the same weight loss starting around 100°C and more than Pr_2NiO_4. A change in weight was monitored during the temperature from 100°C to 950°C. The heating weight loss started below 100°C, while mass gain occurred above 350°C to 450°C. The weight loss started decreasing from 450°C to 950°C. The weight addition step might be the effect of oxygen contaminated in nitrogen atmosphere. Generally excess oxygen in the perovskite compound frequently occurred in the structure because it has oxygen vacancies in the perovskite planes and oxygen interstitials in the rock–salt layers [12]. Therefore under heat treatments 350 to 450°C led to an increase of excess oxygen in the structure.

The TGA data of $Pr_2Ni_{1-x}Cu_xO_4$ reveals that $Pr_2Ni_{0.7}Cu_{0.3}O_4$ perovskite had the highest weight change as compared to that of the other composition. According to the findings reported by Manthiram *et al.*, observed weight loss during heating is due to the loss of oxygen from the lattice. It is observed that, both of

$Pr_2Ni_{0.9}Cu_{0.1}O_4$ and $Pr_2Ni_{0.85}Cu_{0.15}O_4$ has less weight change than $Pr_2Ni_{0.7}Cu_{0.3}O_4$ since their oxygen loss is lower than that of $Pr_2Ni_{0.7}Cu_{0.3}O_4$. The extent of oxygen loss increases with increasing Cu content in $Pr_2Ni_{1-x}Cu_xO_4$. It is noted that the $Pr_2Ni_{0.7}Cu_{0.3}O_4$ has the highest oxygen loss, which is in good agreement with the work of Aguadero $et\ al.$ [4]

The effect of Ga doped $Pr_2Ni_{1-x}Cu_xO_4$ were studied. The weight loss of $Pr_2Ni_{0.7}Cu_{0.3}O_4$ compared with $Pr_2Ni_{0.65}Cu_{0.3}Ga_{0.05}O_4$ and $Pr_2Ni_{0.7}Cu_{0.3}Ga_{0.05}O_4$ was shown in Figure 3.23.
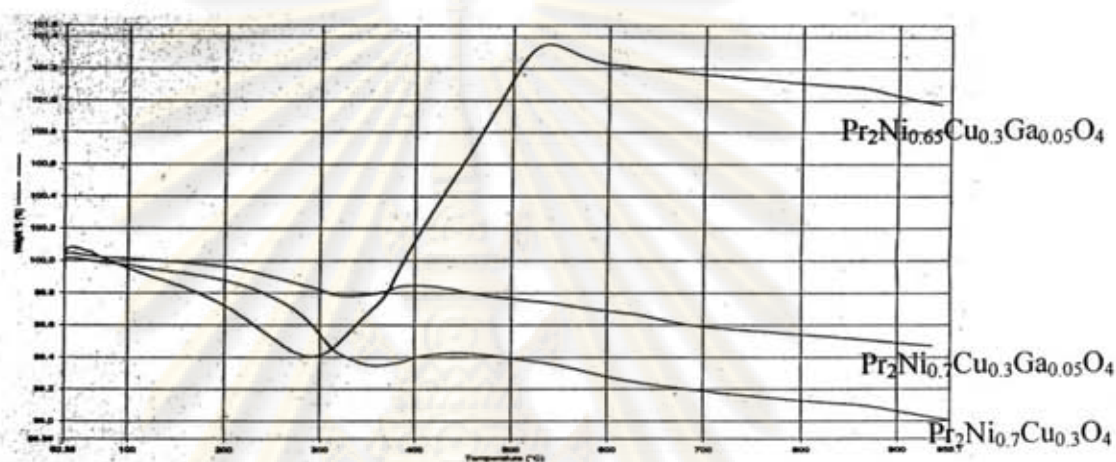
Figure 3.23 Relative weight loss of $Pr_2Ni_{0.7}Cu_{0.3}O_4$ and Ga doped $Pr_2Ni_{0.7}Cu_{0.3}O_4$ as function of temperatures under N_2.

In the case of Ga–doped $Pr_2Ni_{1-x}Cu_xO_4$, it is found that Ga^{3+} addition has an effect on higher capability to accommodate excess oxygen. In order to balance the charge, the amount of oxygen increased in the structure. Because Ga^{3+} was directly substituted Ni^{2+}, it exhibited gain weight of oxygen in stoichiometric more than nonstoichiometric composition (see figure 3.23). It is noticed that the weight % of $Pr_2Ni_{0.65}Cu_{0.3}Ga_{0.05}O_4$ decrease rapidly from room temperature to 290°C and increase abruptly from 300°C to 530°C and decrease gradually at high temperature. Thermal induced oxygen gain in the lattice is the reason for the weight addition. For this reason, it indicated that the weight loss of Ga–doped is less than Ga–undoped $Pr_2Ni_{1-x}Cu_xO_4$.

3.3.3.3 Thermal Analysis of $Pr_2Ni_{1-x}Co_xO_4$ (x = 0.1, 0.2, 0.3), $Pr_2Ni_{0.85}Co_{0.1}Ga_{0.05}O_4$ and $Pr_2Ni_{0.9}Co_{0.1}Ga_{0.05}O_4$

The weight changes for $Pr_2Ni_{1-x}Co_xO_4$ powder samples with various Co contents were heated under N_2 atmosphere. It is suggested that the observed weight change results from the loss of lattice oxygen on heating. TG weight losses are plotted versus temperature in Figure 3.24.
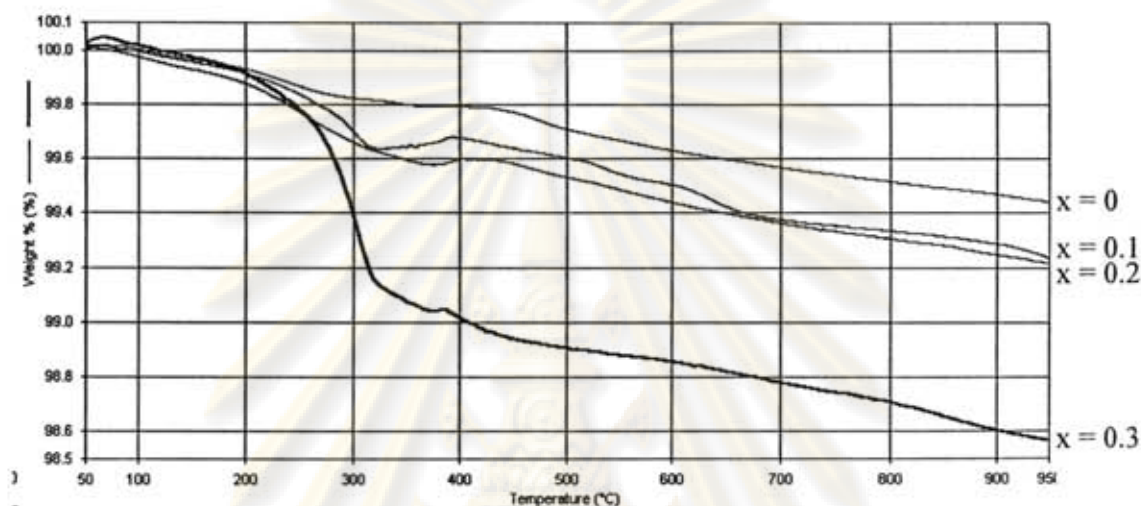
Figure 3.24 Relative weight loss of $Pr_2Ni_{1-x}Co_xO_4$ as function of temperatures and Co content under N_2.

The TGA curves show $Pr_2Ni_{0.7}Co_{0.3}O_4$ has dramatically weight loss starting at 250°C. On the contrary, the weight of $Pr_2Ni_{0.9}Co_{0.1}O_4$ and $Pr_2Ni_{0.8}Co_{0.2}O_4$ start decreasing around 100°C. At 370°C-380°C, the weight of all the samples increase slightly and then decrease slowly until to high temperature. It is explained that oxygen might be adsorbed back into the crystals causing the weight addition.

Pr_2NiO_4, $Pr_2Ni_{0.9}Co_{0.1}O_4$ and $Pr_2Ni_{0.8}Co_{0.2}O_4$ are more stable than $Pr_2Ni_{0.7}Co_{0.3}O_4$. The oxygen loss increases with increasing Co content in $Pr_2Ni_{1-x}Co_xO_4$. Because Co cations have various oxidation states of +2, +3 and +4, therefore it easily changes oxidation state and not stable. Therefore, the increased Co content in $Pr_2Ni_{1-x}Co_xO_4$ causes the increase of oxygen loss from the structure.

The effect of Ga doped $Pr_2Ni_{0.9}Co_{0.1}O_4$ were studied. The weight losses of $Pr_2Ni_{0.9}Co_{0.1}O_4$ compared with $Pr_2Ni_{0.85}Co_{0.1}Ga_{0.05}O_4$ and $Pr_2Ni_{0.9}Co_{0.1}Ga_{0.05}O_4$ was shown in Figure 3.25.
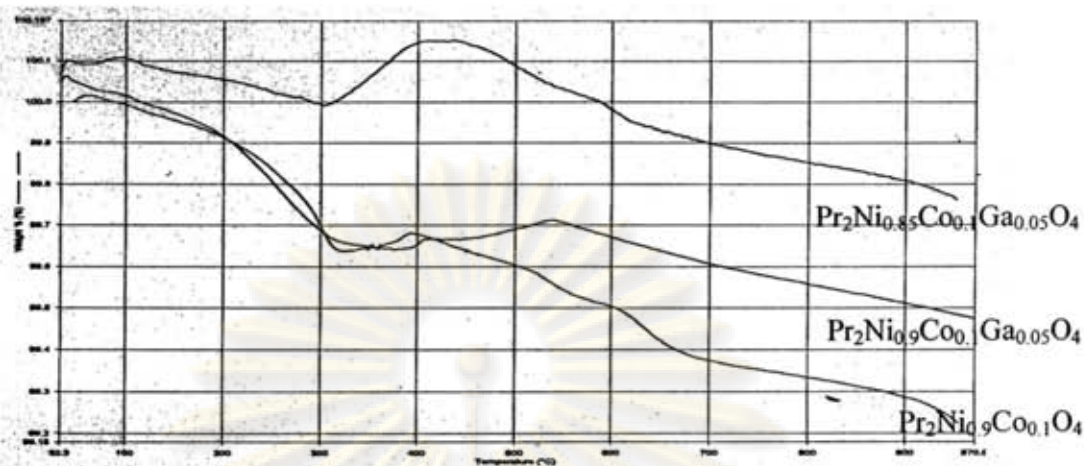
Figure 3.25 Relative weight loss of $Pr_2Ni_{0.9}Co_{0.1}O_4$ and Ga doped $Pr_2Ni_{0.9}Co_{0.1}O_4$ as function of temperatures under N_2.

The oxidation number of Ga^{3+} ions is higher than Ni^{2+}, caused the increase of oxygen in the lattice due to the electroneutrality rule. The stoichiometric compositions have an affect on highest capability to accommodate excess oxygen. Thus Ga–doped $Pr_2Ni_{0.9}Co_{0.1}O_4$ especially stoichiometric compositions have weight loss less than $Pr_2Ni_{0.9}Co_{0.1}O_4$.

3.3.3.4 Thermal Analysis of $Pr_2Ni_{1-x}Zn_xO_4$, $Pr_2Ni_{1-x-0.05}Zn_xGa_{0.05}O_4$ and $Pr_2Ni_{1-x}Zn_xGa_{0.05}O_4$ (x = 0.1, 0.2, 0.3)

Figure 3.26 shows the relative weight change versus temperature for $Pr_2Ni_{1-x}Zn_xO_4$ compounds with various compositions (x = 0.1, 0.2, 0.3).
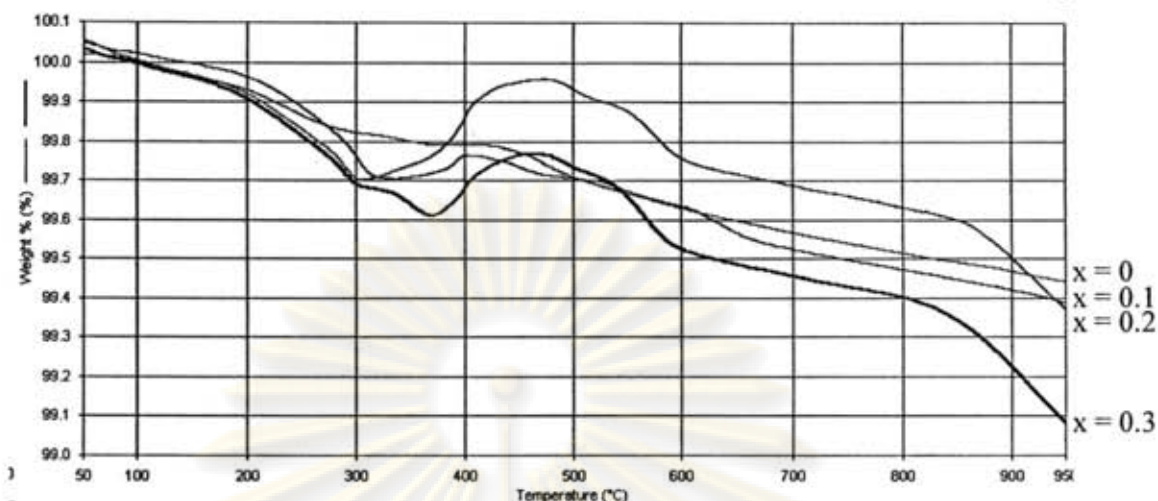
Figure 3.26 Relative weight loss of $Pr_2Ni_{1-x}Zn_xO_4$ as function of temperatures and Zn content under N_2.

All compositions of $Pr_2Ni_{1-x}Zn_xO_4$ has the weight loss after heat up from 100°C to 350°C and increased weight after heat from 300°C to 450°C and then decreased weight loss until 900°C. In the temperature range of 300°C to 450°C, the amounts of oxygen increased due to the nitrogen gas contaminated with oxygen gas. The TGA data of $Pr_2Ni_{1-x}Zn_xO_4$ with x = 0.3 had the highest weight loss.

The effect of Ga doped $Pr_2Ni_{1-x}Zn_xO_4$ were studied. The weight loss of $Pr_2Ni_{0.7}Zn_{0.3}O_4$ compared with $Pr_2Ni_{0.65}Zn_{0.3}Ga_{0.05}O_4$ and $Pr_2Ni_{0.7}Zn_{0.3}Ga_{0.05}O_4$ was shown in Figure 3.27.
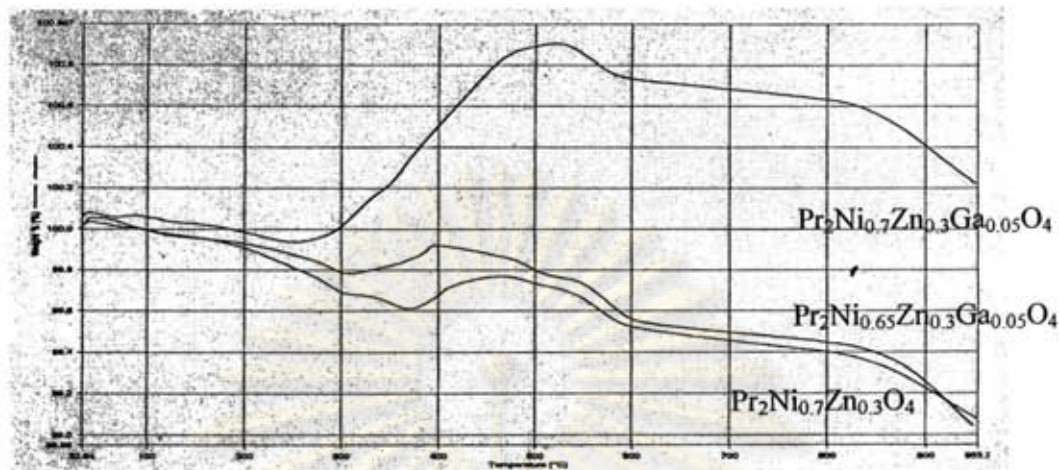
Figure 3.27 Relative weight loss of $Pr_2Ni_{0.7}Zn_{0.3}O_4$ and Ga doped $Pr_2Ni_{0.7}Zn_{0.3}O_4$ as function of temperatures under N_2.

For Ga doped at B-site of $Pr_2Ni_{1-x}Zn_xO_4$, the result is similar to $Pr_2Ni_{1-x}Cu_xO_4$, $Pr_2Ni_{1-x}Co_xO_4$. It exhibited gain weight of oxygen in the lattice in stoichiometric and nonstoichiometric more than Ga–undoped composition.

3.3.3.5 Thermal Analysis of $Pr_2Ni_{1-x}In_xO_4$, $Pr_2Ni_{1-x-0.05}In_xGa_{0.05}O_4$ and $Pr_2Ni_{1-x}In_xGa_{0.05}O_4$ (x = 0.1, 0.2, 0.3)

Thermogravimetric analyses of powder $Pr_2Ni_{1-x}In_xO_4$ after sintering was measured under nitrogen atmosphere. The weight changes were displayed in Figure 3.28.
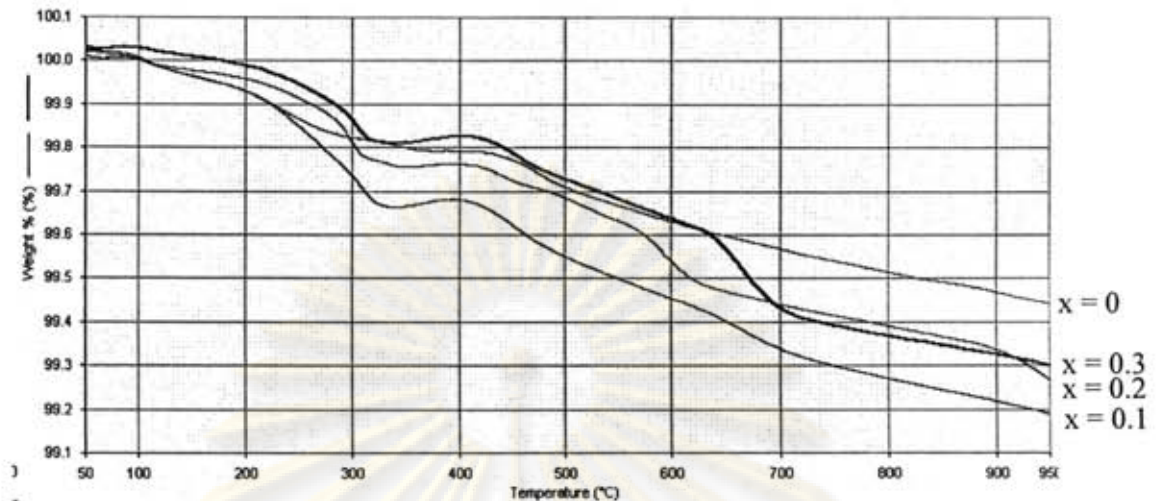
Figure 3.28 Relative weight loss of $Pr_2Ni_{1-x}In_xO_4$ as function of temperatures and In content under N_2.

From Figure 3.28, the weight loss of $Pr_2Ni_{1-x}In_xO_4$ show the same pattern, it started decrease from 100°C to 320°C and increase slightly to 400°C and then decrease gradually from 420°C to 950°C.

The relative weight loss of $Pr_2Ni_{1-x}In_xO_4$ (x = 0.1-0.3) are different from the others. The oxygen loss decreases with increasing In content. The result indicated that the $Pr_2Ni_{0.9}In_{0.1}O_4$ membrane had the highest oxygen loss. It suggests a stronger binding of the oxygen to the lattice with increasing In content, implying a stronger In–O bond compared to the Ni–O bond.

The effect of Ga doped $Pr_2Ni_{1-x}In_xO_4$ were studied. Figure 3.29 exhibited the effect of Ga doped $Pr_2Ni_{0.7}In_{0.3}O_4$. The weight loss of $Pr_2Ni_{0.7}In_{0.3}O_4$ was compared with $Pr_2Ni_{0.65}In_{0.3}Ga_{0.05}O_4$ and $Pr_2Ni_{0.7}In_{0.3}Ga_{0.05}O_4$.
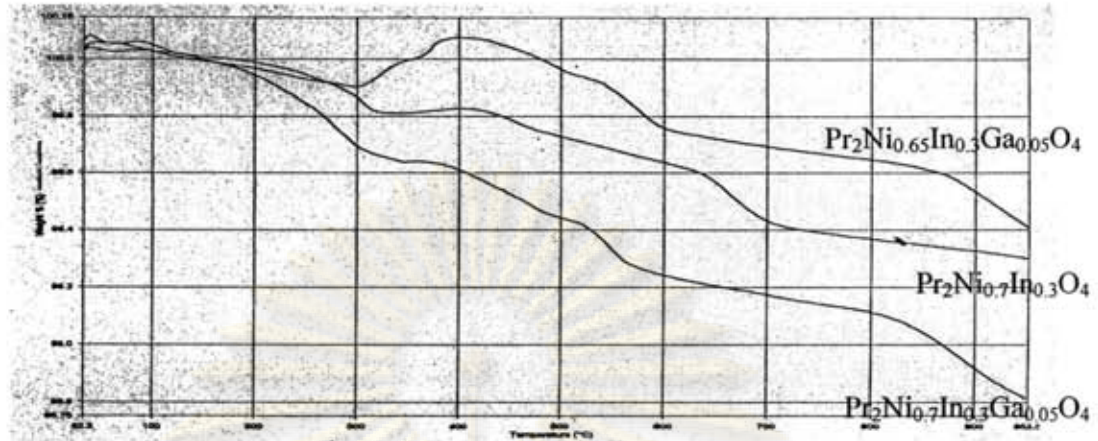
Figure 3.29 Relative weight loss of $Pr_2Ni_{0.7}In_{0.3}O_4$ and Ga doped $Pr_2Ni_{0.7}In_{0.3}O_4$ as function of temperatures under N_2.

Ga^{3+} ion added to $Pr_2Ni_{0.7}In_{0.3}O_4$ affects on higher capability to accommodate excess oxygen. It exhibited the weight increase. But in the case of excess Ga^{3+} ions addition to the oxide, only weight loss was observed. (see Figure 3.29)

The ionic radius of Ga^{3+} ions ($r_{Ga^{3+}}$ = 0.76 Å) is smaller than In^{3+} ions ($r_{In^{3+}}$ = 0.94 Å) is a possible reason. Ga^{3+} ions added to stoichiometric composition was easily substituted at Ni–site of $Pr_2Ni_{1-x}In_xO_4$. In the case of excess Ga^{3+} ions added to the mixed oxide, Ga^{3+} ions was hardly introduced in the vacancy site of Ni^{2+} in $Pr_2Ni_{1-x}In_xO_4$ or interstitial site. The oxidation state of In^{3+} is higher than Ni^{2+}, therefore the excess of Ga^{3+} ions in the structure cause the repulsion of the charge.

3.3.3.6 Thermal Analysis of $Pr_2Ni_{0.9}Mg_{0.1}O_4$, $Pr_2Ni_{0.85}Mg_{0.1-}$ $Ga_{0.05}O_4$ and $Pr_2Ni_{0.9}Mg_{0.1}Ga_{0.05}O_4$

TGA plots of the $Pr_2Ni_{0.9}Mg_{0.1}O_4$ sample was shown in Figure 3.30.
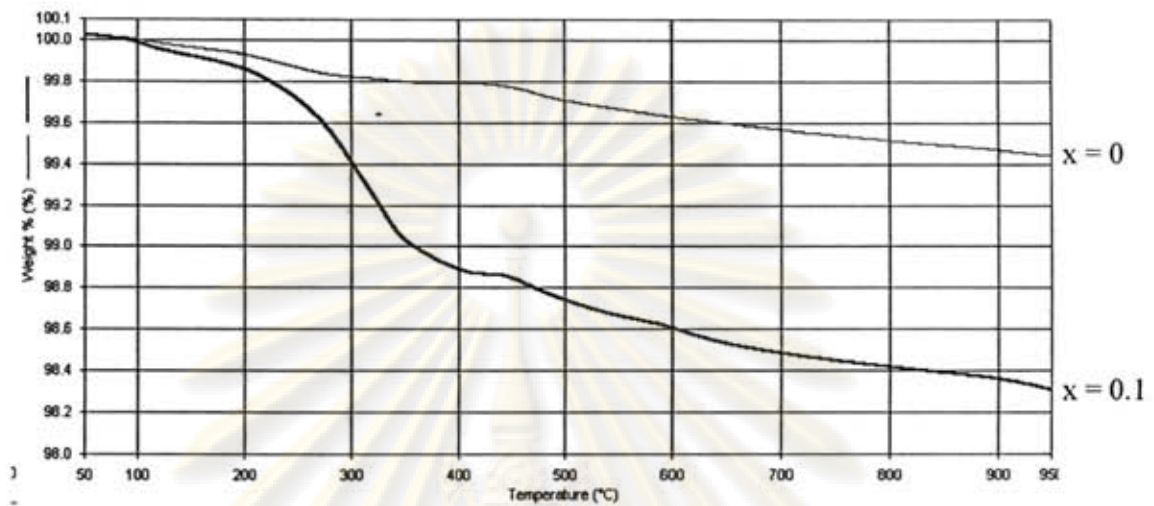
Figure 3.30 Relative weight loss of $Pr_2Ni_{0.9}Mg_{0.1}O_4$ as function of temperatures under N_2.

From Figure 3.30, the TGA curves show that $Pr_2Ni_{0.9}Mg_{0.1}O_4$ had rapidly weight loss starting at 250°C and decreased slightly to 950°C. The $Pr_2Ni_{0.9}Mg_{0.1}O_4$ was compared with Pr_2NiO_4, it is seen that the weight change of $Pr_2Ni_{0.9}Mg_{0.1}O_4$ was more than the Pr_2NiO_4. It suggested that $Pr_2Ni_{0.9}Mg_{0.1}O_4$ have the great oxygen loss in the lattice.

The effect of Ga doped $Pr_2Ni_{0.9}Mg_{0.1}O_4$ were studied. Figure 3.31 exhibited the effect of Ga doped $Pr_2Ni_{0.9}Mg_{0.1}O_4$. The weight loss of $Pr_2Ni_{0.9}Mg_{0.1}O_4$ was compared with $Pr_2Ni_{0.85}Mg_{0.1}Ga_{0.05}O_4$ and $Pr_2Ni_{0.9}Mg_{0.1}Ga_{0.05}O_4$.
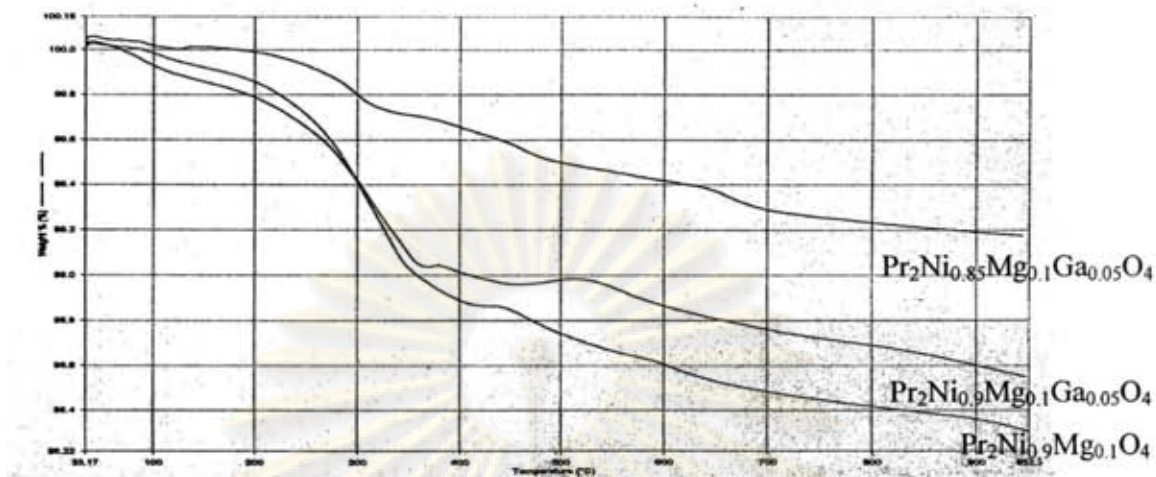
Figure 3.31 Relative weight loss of $Pr_2Ni_{0.9}Mg_{0.1}O_4$ and Ga doped $Pr_2Ni_{0.9}Mg_{0.1}O_4$ as function of temperatures under N_2.

Ga-doped in $Pr_2Ni_{0.9}Mg_{0.1}O_4$ is resemble to Ga–doped $Pr_2Ni_{1-x}M_xO_4$ (M=Cu, Co, Zn). It exhibited gain weight of oxygen in the lattice in stoichiometric and nonstoichiometric more than Ga–undoped composition.

3.3.4 Temperature-program desorption of oxygen (O$_2$-TPD)

Oxygen desorption property is useful to predict the oxygen permeability of the prepared samples. Oxygen desorption properties of perovskites are determined by O$_2$-TPD experiments. The oxygen was adsorbed through chemisorption mechanism. O$_2$ gas participated not only on surface but also inside the perovskite.

In general, the desorption peaks obtained from the perovskite-like mixed oxides contain three kinds of oxygen species. The desorption peak appeared at $T <$ 500 °C is ascribed to the oxygen chemically adsorbed on the surface (denoted as: α oxygen); the desorption peak appeared at $500 < T < 800$ °C is ascribed to the oxygen chemically adsorbed on the oxygen vacancy (denoted as: β oxygen); and the desorption peak appeared at $T > 800$ °C is ascribed to the oxygen escaped from the lattice (denoted as: γ oxygen) [19]. In particular its onset and intensity depend in part on the nature of the metal B of the structure. When the B ion is partially substituted with an ion of different oxidation state, charge compensation is required so as to achieve electroneutrality. This can either be achieved by formation of oxygen vacancies or oxygen hyperstoichiometry [12].

3.3.4.1 Oxygen desorption of Pr$_2$NiO$_4$ compounds

The O$_2$-TPD profile of Pr$_2$NiO$_4$ perovskite after sintering at 1,300°C is given in Figure 3.32.
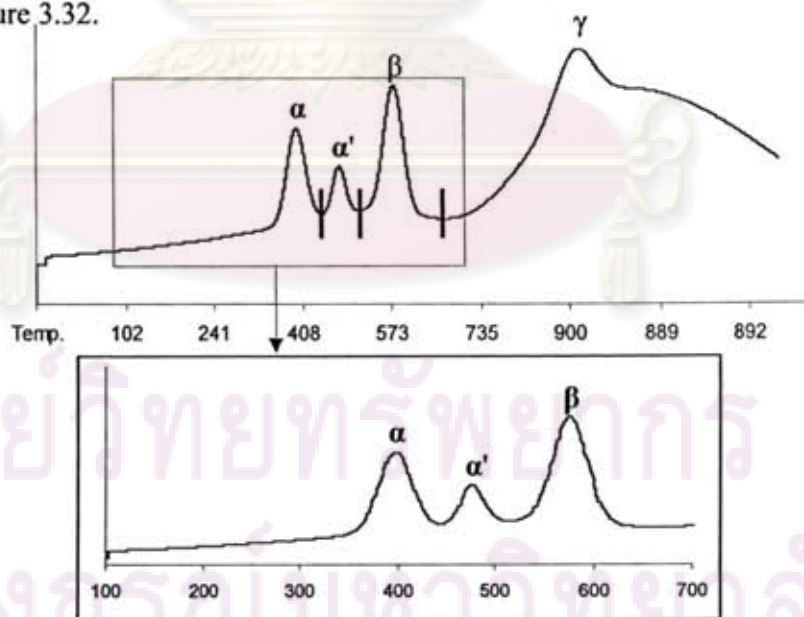
Figure 3.32 O$_2$-TPD chromatogram of Pr$_2$NiO$_4$.

Four oxygen desorption peaks (α, α', β and γ respectively) appear in the TPD pattern at temperatures about 400, 480, 580 and 900°C. The amount of desorption for each peak is 0.087, 0.034, 0.102 and 0.536 mmol O_2/g, respectively. The result shows that there are different states of oxygen on the oxide surface. α and α' peak could be attributed to O^- and O^{2-} adsorb on the surface reported by Moseley [48-49]. For oxygen peak at 580°C could be attributed to the β oxygen which is adsorbed on oxygen vacancies. The last oxygen peak could be assigned to the γ oxygen which is associated with the release of oxygen from the bulk of the solid. It is noted that the oxygen signal not to reach the baseline at the final temperature of 900 °C, indicating that the liberation of oxygen is still occurring. The oxygen desorption from 100°C up to 700°C amounted to 0.224 mmolO_2/g for Pr_2NiO_4 clearly indicates that oxygen desorbed from the crystal lattice. It is noted that the oxygen desorption property of all samples are considered in the range of 100 to 700°C.

3.3.4.2 Oxygen desorption of $Pr_2Ni_{1-x}Cu_xO_4$ and Ga doped $Pr_2Ni_{1-x}Cu_xO_4$ compounds (x=0.1, 0.15, 0.3)

The O_2-TPD profiles for $Pr_2Ni_{1-x}Cu_xO_4$ were shown in Fig. 3.33.
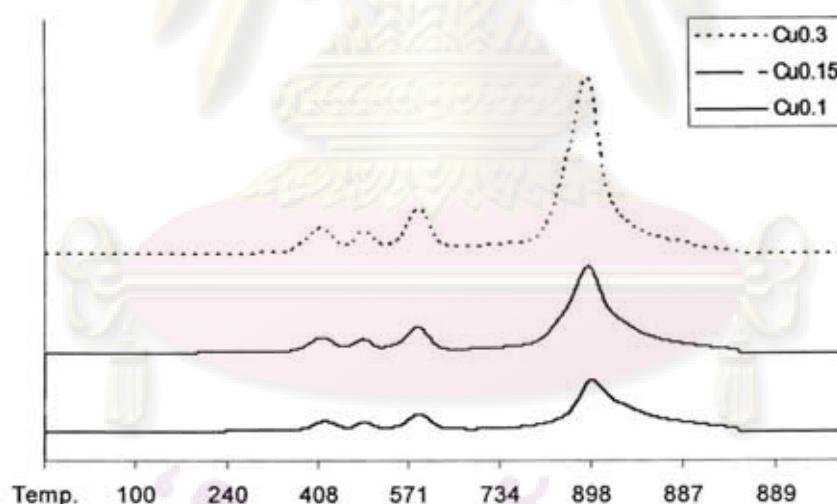
Figure 3.33 O_2-TPD chromatogram of $Pr_2Ni_{1-x}Cu_xO_4$ (x=0.1, 0.15, 0.3).

Four O_2 desorption peaks are observed for all samples in the temperature range100-900°C. The oxygen desorption amount increases with increasing content of Cu substitution for Ni in Pr_2NiO_4 which was listed in Table 3.14. With the increase of x (x=0.1-0.3) the peak area increase gradually, implying that the oxygen vacancies and mobile lattice oxygen increase.

Table 3.14 The amount of oxygen desorbed from Pr_2NiO_4 and $Pr_2Ni_{1-x}Cu_xO_4$, (x = 0.1, 0.15, 0.3).

	Oxygen desorption (mmol/g)			Total oxygen desorption (mmol/g) (100-700°C)	Oxygen desorption (mmol/g) γ (700°C up)
	α (100-450°C)	α' (350-550°C)	β (550-700°C)		
x = 0	0.087	0.034	0.102	0.224	0.536
x = 0.1	0.058	0.031	0.089	0.178	0.539
x = 0.15	0.055	0.033	0.091	0.180	0.518
x = 0.3	0.093	0.044	0.118	0.256	0.562

The desorption peak at 550–700 °C is associated with desorption of the oxygen chemically adsorption on oxygen vacancies. β–oxygen corresponds to the reduction of Cu^{2+} to lower oxidation states. As Cu substitution increases in $Pr_2Ni_{1-x}Cu_xO_4$ (x = 0.1, 0.15, 0.3), it is expected to create more oxygen vacancy in lattice and therefore the amount of desorbing oxygen increases. It is observed that the value of total desoprtion of undoped Pr_2NiO_4 is higher than Cu–doped Pr_2NiO_4 (x = 0.1, 0.15). Doping Cu 30% mole to Pr_2NiO_4 is the right content to enhance the oxygen desorption property. The oxidation number of Pr is regarded as mixed valence of +4 and +3, and those of Ni and Cu also seem to be +2. Therefore, the exact oxygen content number in $Pr_2Ni_{1-x}Cu_xO_4$ seem to be greater than 4, suggesting that the oxide ion conduction is based on the excess oxygen introduced by the higher valence number of Pr, Ni and/ or Cu as suggested in the literature [37].

The effect of Ga doped $Pr_2Ni_{1-x}Cu_xO_4$ were studied to improve the desorption property. The amount of total oxygen desorbed (100-700°C) of $Pr_2Ni_{1-x}Cu_xO_4$ compared with $Pr_2Ni_{1-x-0.05}Cu_xGa_{0.05}O_4$ and $Pr_2Ni_{1-x}Cu_xGa_{0.05}O_4$, were shown in Table 3.15 and Figure 3.34.

Table 3.15 The amount of total oxygen desorbed (100-700°C) of $Pr_2Ni_{1-x}Cu_xO_4$, $Pr_2Ni_{1-x-0.05}Cu_xGa_{0.05}O_4$ and $Pr_2Ni_{1-x}Cu_xGa_{0.05}O_4$ (x=0.1, 0.15, 0.3).

	Total oxygen desorption (α, α', β) 100-700°C (mmol/g)		
	$Pr_2Ni_{1-x}Cu_xO_4$	$Pr_2Ni_{1-x-0.05}Cu_xGa_{0.05}O_4$	$Pr_2Ni_{1-x}Cu_x\ Ga_{0.05}O_4$
x = 0.1	0.178	0.296	0.255
x = 0.15	0.180	0.326	0.255
x = 0.3	0.256	0.300	0.280
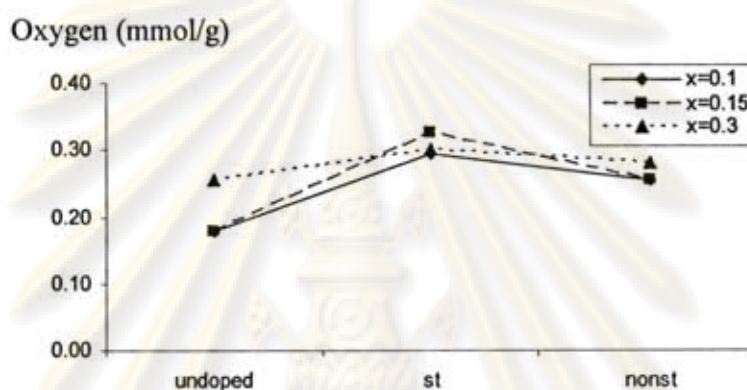
Figure 3.34 The amount of oxygen desorbed of $Pr_2Ni_{1-x}Cu_xO_4$ (undoped), $Pr_2Ni_{1-x-0.05}Cu_xGa_{0.05}O_4$ (st) and $Pr_2Ni_{1-x}Cu_xGa_{0.05}O_4$ (nonst) (x=0.1, 0.15, 0.3).

It is shown that Ga–doped $Pr_2Ni_{1-x}Cu_xO_4$ has higher capability to accommodate excess oxygen than undoped metal. Doping Ga^{3+} 5 mole% into $Pr_2Ni_{1-x}Cu_xO_4$ also increase the excess amount of oxygen which enhance oxygen desorption. It is due to the large free volume in the rock-salt block in Pr_2NiO_4. Therefore Ga doped $Pr_2Ni_{1-x}Cu_xO_4$, the interstitial oxygen and excess cation might be introduced into the rock-salt block [42].

Ga^{3+} was directly substituted by Ni^{2+}, it exhibited the increase amount of oxygen desorbed in stoichiometric more than nonstoichiometric composition of $Pr_2Ni_{1-x}Cu_xO_4$.

3.3.4.3 Oxygen desorption of $Pr_2Ni_{1-x}Co_xO_4$ (x=0.1, 0.2, 0.3) and Ga doped $Pr_2Ni_{1-x}Co_xO_4$ compounds (x=0.1)

The O_2-TPD profiles for $Pr_2Ni_{1-x}Co_xO_4$ revealed a similar trend to the analogous $Pr_2Ni_{1-x}Cu_xO_4$ system.

The amount of oxygen desorbed, calculated from deconvoluted oxygen peaks, is given in Table 3.16.

Table 3.16 The amount of oxygen desorbed from $Pr_2Ni_{1-x}Co_xO_4$ (x = 0.1, 0.2, 0.3).

	Oxygen (mmol/g)			Total oxygen desorption (100-700°C)	Oxygen(mmol/g) γ (700°C up)
	α (100-450°C)	α' (350-550°C)	β (550-700°C)		
x = 0	0.087	0.034	0.102	0.224	0.536
x = 0.1	0.046	0.047	0.084	0.207	0.297
x = 0.2	0.093	0.031	0.083	0.207	0.541
x = 0.3	0.080	0.042	0.111	0.233	0.602

From Table 3.16, It was found that the β oxygen desorbed at intermediate temperature zone of $Pr_2Ni_{1-x}Co_xO_4$ with x=0.3 have the higher total oxygen desorption than that of the other contents. It is concluded that $Pr_2Ni_{1-x}Co_xO_4$ with x=0.3 has the highest total oxygen permeation. In the range of 550–700 °C, the desorption of surface lattice oxygen due to partial reduction of Co^{3+} [50]. As compared to the $Pr_2Ni_{0.7}Cu_{0.3}O_4$, doping Co into Pr_2NiO_4 barely increase the oxygen desorption property of the compound.

The amount of total oxygen desorbed of $Pr_2Ni_{1-x}Co_xO_4$ and Ga doped $Pr_2Ni_{1-x}Co_xO_4$ (x = 0.1) compounds at temperature in range 100-700°C are shown in Table 3.17 and Figure 3.35.

Table 3.17 the amount of total oxygen desorbed (100-700°C) of $Pr_2Ni_{1-x}Co_xO_4$, $Pr_2Ni_{1-x-0.05}Co_xGa_{0.05}O_4$ and $Pr_2Ni_{1-x}Co_xGa_{0.05}O_4$ (x=0.1, 0.2, 0.3).

	Total oxygen desorption (α, α', β) 100-700°C (mmol/g)		
	$Pr_2Ni_{1-x}Co_xO_4$	$Pr_2Ni_{1-x-0.05}Co_xGa_{0.05}O_4$	$Pr_2Ni_{1-x}Co_x Ga_{0.05}O_4$
x = 0.1	0.207	0.290	0.179
x = 0.2	0.207	-	-
x = 0.3	0.233	-	-

Oxygen (mmol/g)
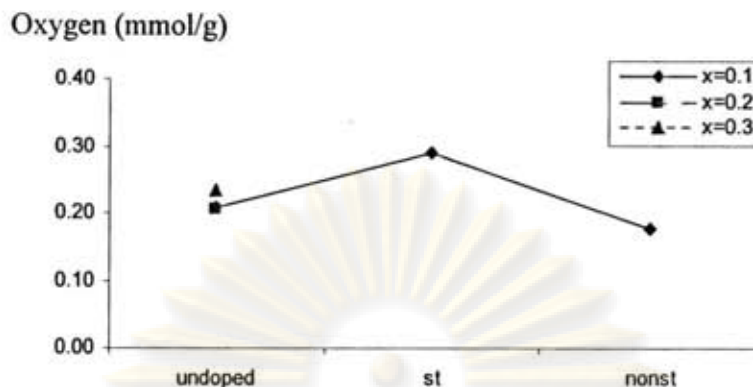
Figure 3.35 The amount of oxygen desorbed of $Pr_2Ni_{1-x}Co_xO_4$ (undoped), $Pr_2Ni_{1-x-0.05}Co_xGa_{0.05}O_4$ (st) and $Pr_2Ni_{1-x}Co_xGa_{0.05}O_4$ (nonst) (x=0.1, 0.2, 0.3).

The oxidation number of Ga^{3+} ions is higher than Ni^{2+}, caused the increase in the excess amount of oxygen due to the electroneutrality rule. The oxide ion conductivity seems to be much improved and in the rock-salt block in Ga doped $Pr_2Ni_{0.9}Co_{0.1}O_4$, interstitial oxygen and excess cation may be introduced into the rock-salt block, which could be the fast oxygen diffusion route.

The stoichiometric compositions have an affect on highest capability to accommodate excess oxygen. Thus Ga–doped $Pr_2Ni_{0.9}Co_{0.1}O_4$ especially stoichiometric compositions has amount of oxygen desorbed more than $Pr_2Ni_{0.9}Co_{0.1}O_4$.

3.3.4.4 Oxygen desorption of $Pr_2Ni_{1-x}Zn_xO_4$ and Ga doped $Pr_2Ni_{1-x}Zn_xO_4$ compounds (x=0.1, 0.2, 0.3)

The O_2-TPD profiles for $Pr_2Ni_{1-x}Zn_xO_4$ showed similar result to analogous $Pr_2Ni_{1-x}Cu_xO_4$ system.

Table 3.18 lists amount of oxygen desorption for $Pr_2Ni_{1-x}Zn_xO_4$ with various compositions of Zn^{2+} ion.

Table 3.18 The amount of oxygen desorbed from $Pr_2Ni_{1-x}Zn_xO_4$ (x = 0.1, 0.2, 0.3).

	Oxygen (mmol/g)			Total oxygen desorption (100-700°C)	Oxygen(mmol/g) γ (700°C up)
	α (100-450°C)	α' (350-550°C)	β (550-700°C)		
x = 0	0.087	0.034	0.102	0.224	0.536
x = 0.1	0.082	0.032	0.088	0.202	0.496
x = 0.2	0.076	0.038	0.100	0.214	0.436
x = 0.3	0.114	0.046	0.120	0.280	0.432

Amount of β oxygen desorption increased with an increasing Zn contents. The amount of oxygen desorption of $Pr_2Ni_{1-x}Zn_xO_4$ with x = 0.3 had the highest as compared to the $Pr_2Ni_{1-x}Zn_xO_4$ with content of x = 0.1, 0.2. It showed that $Pr_2Ni_{0.7}Zn_{0.3}O_4$ had the highest oxygen vacancy and oxygen permeability.

The amount of oxygen desorption during the temperature from 100°C to 700°C of $Pr_2Ni_{1-x}Zn_xO_4$ and Ga doped $Pr_2Ni_{1-x}Zn_xO_4$ (x = 0.1, 0.2, 0.3) is displayed in Table 3.19 and Figure 3.36.

Table 3.19 The amount of total oxygen desorbed (100-700°C) of $Pr_2Ni_{1-x}Zn_xO_4$, $Pr_2Ni_{1-x-0.05}Zn_xGa_{0.05}O_4$ and $Pr_2Ni_{1-x}Zn_xGa_{0.05}O_4$ (x=0.1, 0.2, 0.3).

	Total oxygen desorption (α, α', β) 100-700°C (mmol/g)		
	$Pr_2Ni_{1-x}Zn_xO_4$	$Pr_2Ni_{1-x-0.05}Zn_xGa_{0.05}O_4$	$Pr_2Ni_{1-x}Zn_xGa_{0.05}O_4$
x = 0.1	0.202	0.264	0.190
x = 0.2	0.214	0.318	0.260
x = 0.3	0.280	0.373	0.203
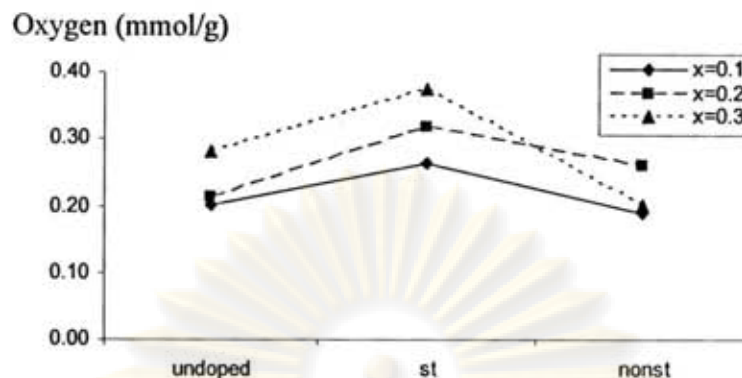
Figure 3.36 The amount of oxygen desorbed of $Pr_2Ni_{1-x}Zn_xO_4$ (undoped), $Pr_2Ni_{1-x-0.05}Zn_xGa_{0.05}O_4$ (st) and $Pr_2Ni_{1-x}Zn_xGa_{0.05}O_4$ (nonst) (x=0.1, 0.2, 0.3).

Ga doped at B-site of $Pr_2Ni_{1-x}Zn_xO_4$ showed the same trend as $Pr_2Ni_{1-x}Cu_xO_4$, $Pr_2Ni_{1-x}Co_xO_4$. Considering the ionic size and valence number of Ga^{3+} ions, interstitial oxygen is easily formed. It exhibited the increase amount of oxygen in stoichiometric and nonstoichiometric more than Ga–undoped composition except $Pr_2Ni_{1-x}Zn_xGa_{0.05}O_4$ (x = 0.1, 0.3).

3.3.4.5 Oxygen desorption of $Pr_2Ni_{1-x}In_xO_4$ and Ga doped $Pr_2Ni_{1-x}In_xO_4$ compounds (x=0.1, 0.2, 0.3)

Four O_2 desorption peaks are observed for all samples. The pattern at temperatures about of 400, 480, 580 and 900°C is similar to $Pr_2Ni_{1-x}Cu_xO_4$ system. The amount of oxygen desorption were listed in Table 3.20.

Table 3.20 The amount of oxygen desorbed from $Pr_2Ni_{1-x}In_xO_4$ (x = 0.1, 0.2, 0.3).

	Oxygen (mmol/g)			Total oxygen desorption (100-700°C)	Oxygen(mmol/g) γ (700°C up)
	α (100-450°C)	α' (350-550°C)	β (550-700°C)		
x = 0	0.087	0.034	0.102	0.224	0.536
x = 0.1	0.086	0.032	0.092	0.210	0.500
x = 0.2	0.086	0.031	0.090	0.207	0.520
x = 0.3	0.082	0.033	0.087	0.202	0.470

The oxygen desorptions of $Pr_2Ni_{1-x}In_xO_4$ (x = 0.1-0.3) are different from the others. The degree of oxygen desorption slightly decreases with increasing In content. According to Ishihara et al., [42] the substitution of the trivalent for the Ni-site, where the regular valence is divalent, results in lower permeation rates compared to doping with divalent cations. A plausible reason for this behavior is not clear.

Figure 3.37 exhibited the effect of Ga doped $Pr_2Ni_{0.7}In_{0.3}O_4$. The amount of oxygen desorption of $Pr_2Ni_{0.7}In_{0.3}O_4$ was compared with $Pr_2Ni_{0.65}In_{0.3}Ga_{0.05}O_4$ and $Pr_2Ni_{0.7}In_{0.3}Ga_{0.05}O_4$.

Table 3.21 The amount of total oxygen desorbed (100-700°C) of $Pr_2Ni_{1-x}In_xO_4$, $Pr_2Ni_{1-x-0.05}In_xGa_{0.05}O_4$ and $Pr_2Ni_{1-x}In_xGa_{0.05}O_4$ (x=0.1, 0.2, 0.3).

	Total oxygen desorption (α, α', β) 100-700°C (mmol/g)		
	$Pr_2Ni_{1-x}In_xO_4$	$Pr_2Ni_{1-x-0.05}In_xGa_{0.05}O_4$	$Pr_2Ni_{1-x}In_xGa_{0.05}O_4$
x = 0.1	0.210	0.344	0.287
x = 0.15	0.207	0.342	0.339
x = 0.3	0.202	0.317	0.299
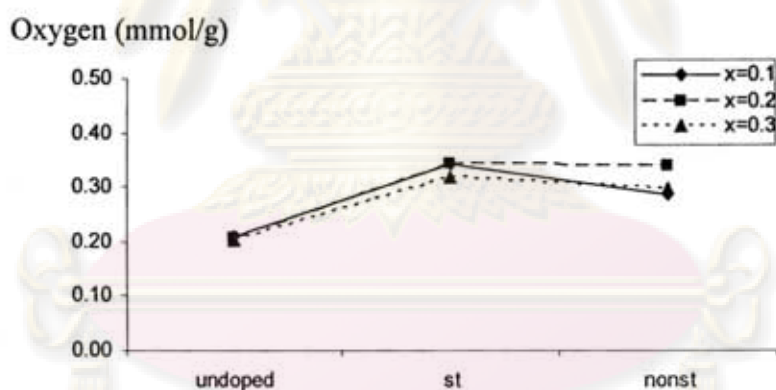
Figure 3.37 The amount of oxygen desorbed of $Pr_2Ni_{1-x}In_xO_4$ (undoped), $Pr_2Ni_{1-x-0.05}In_xGa_{0.05}O_4$ (st) and $Pr_2Ni_{1-x}In_xGa_{0.05}O_4$ (nonst) (x=0.1, 0.2, 0.3).

Ga^{3+} ion added stoichiometrically and nonstoichiometrically to $Pr_2Ni_{1-x}In_xO_4$ affects on higher capability to accommodate excess oxygen. The mechanism is not clear for the declining permeability after In-doping and increasing after Ga-doping. Considering the ionic size ($r_{Ga^{3+}}$ = 0.76 Å, $r_{In^{3+}}$ = 0.94 Å), doped Ga might be

introduced at the vacancy site of Ni in Pr_2NiO_4 or interstitial site, due to the excess amount of cations, interstitial oxygen is easily formed. Since the interstitial oxygen as well as oxygen vacancy is introduced, the oxide ion conductivity seems to be much improved.

Thus, $Pr_2Ni_{1-x-0.05}In_xGa_{0.05}O_4$ and $Pr_2Ni_{1-x}In_xGa_{0.05}O_4$ showed the higher amount of oxygen desorbed.

3.3.4.6 Oxygen desorption of $Pr_2Ni_{0.9}Mg_{0.1}O_4$ and Ga doped $Pr_2Ni_{0.9}Mg_{0.1}O_4$ compounds

$Pr_2Ni_{0.9}Mg_{0.1}O_4$ showed four O_2 desorption peaks. The oxygen desorption peak α, α', β and γ with the values of 0.090, 0.039, 0.101 and 0.418 mmol/g, respectively. $Pr_2Ni_{0.9}Mg_{0.1}O_4$ has total oxygen desorption 0.230 mmol/g reveals the slightly higher oxygen desorption than that of Pr_2NiO_4 (0.224 mmol/g) in the range of 100-700°C.

The effect of Ga doped $Pr_2Ni_{0.9}Mg_{0.1}O_4$ were studied. The amount of total oxygen desorbed (100-700°C) of $Pr_2Ni_{0.9}Mg_{0.1}O_4$ compared with $Pr_2Ni_{0.85}Mg_{0.1}Ga_{0.05}O_4$ and $Pr_2Ni_{0.9}Mg_{0.1}Ga_{0.05}O_4$, were shown in Table 3.21 and Figure 3.38.

Table 3.22 The amount of total oxygen desorbed (100-700°C) of $Pr_2Ni_{1-x}Mg_xO_4$, $Pr_2Ni_{1-x-0.05}Mg_xGa_{0.05}O_4$ and $Pr_2Ni_{1-x}Mg_xGa_{0.05}O_4$ (x=0.1).

	Total oxygen desorption (α, α', β) 100-700°C (mmol/g)		
	$Pr_2Ni_{1-x}Mg_xO_4$	$Pr_2Ni_{1-x-0.05}Mg_xGa_{0.05}O_4$	$Pr_2Ni_{1-x}Mg_xGa_{0.05}O_4$
x = 0.1	0.230	0.249	0.299

Oxygen (mmol/g)
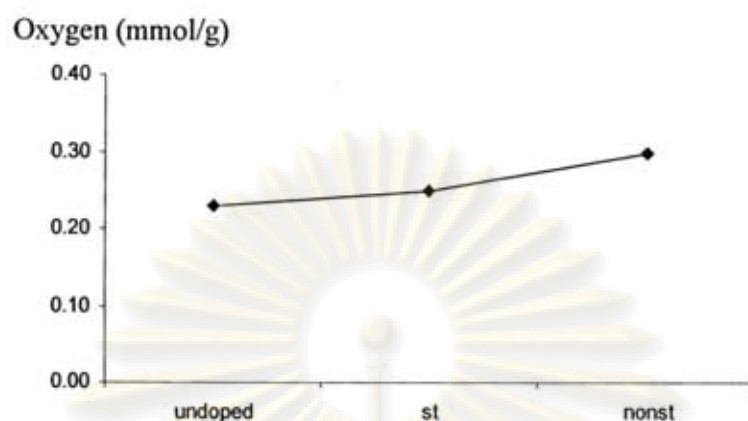
Figure 3.38 The amount of oxygen desorbed of $Pr_2Ni_{0.9}Mg_{0.1}O_4$ (undoped), $Pr_2Ni_{0.85}Mg_{0.1}Ga_{0.05}O_4$ (st) and $Pr_2Ni_{0.9}Mg_{0.1}Ga_{0.05}O_4$ (nonst).

Ga-doped in $Pr_2Ni_{0.9}Mg_{0.1}O_4$ exhibited the increase amount of oxygen in stoichiometric and nonstoichiometric compounds more than Ga–undoped oxide.

For $Pr_2Ni_{0.9}Mg_{0.1}O_4$, the addition of excess Ga^{3+} seems to improve the oxygen–desorption property which is contradicted to the other Ga–doped oxides.

It is concluded that the oxygen desorption property as well as oxygen permeability of Pr_2NiO_4 depend significantly on the doped metals and their composition in the material. The increasing order of the values of oxygen desorption of $Pr_2Ni_{1-x}M_xO_4$ (M = Cu, Co, Zn, In, Mg) is summarized as follows:

$Pr_2Ni_{0.9}In_{0.1}O_4 < Pr_2NiO_4 < Pr_2Ni_{0.7}Co_{0.3}O_4 < Pr_2Ni_{0.9}Mg_{0.1}O_4 < Pr_2Ni_{0.7}Cu_{0.3}O_4 < Pr_2Ni_{0.7}Zn_{0.3}O_4$. For Ga doped $Pr_2Ni_{1-x}M_xO_4$, $Pr_2Ni_{0.65}Zn_{0.3}Ga_{0.05}O_4$ shows the highest oxygen desorption value.

3.3.5 Electrical conductivity

For perovskite MIECs, the co-presence of electronic holes and oxygen vacancies makes them simultaneously exhibit both electronic and ionic conductivity. As electronic conductivity is at least one order higher than ionic conductivity, the measured values (total conductivity) can be mainly referred to electronic conductivity [54].

The total conductivity measured by the dc four-probe method can be regarded as the representative of electronic conductivity. After sintered at 1,300°C, the temperature dependence of the electrical conductivity was measured in the temperature range of 25-800°C in air.

Electronic conductivity of the Pr_2NiO_4, $Pr_2Ni_{1-x}M_xO_4$ (M = Cu, Co, Zn, In; x = 0.1-0.3 and Mg; x = 0.1) and $Pr_2Ni_{1-x-0.05}M_xGa_{0.05}O_4$, $Pr_2Ni_{1-x}M_xGa_{0.05}O_4$ (M = Cu, Zn; x = 0.1-0.3 and Mg; x = 0.1) cathodes has been investigated.

3.3.5.1 Electrical conductivity of Pr_2NiO_4 compounds

The electrical conducting property of Pr_2NiO_4 was investigated as a function of measuring temperature.
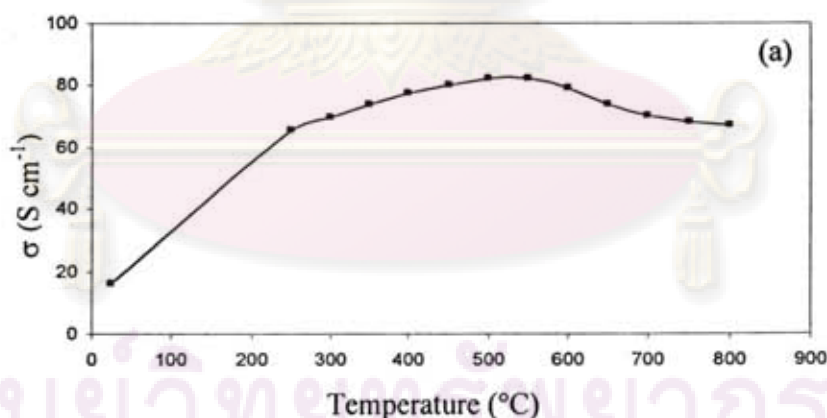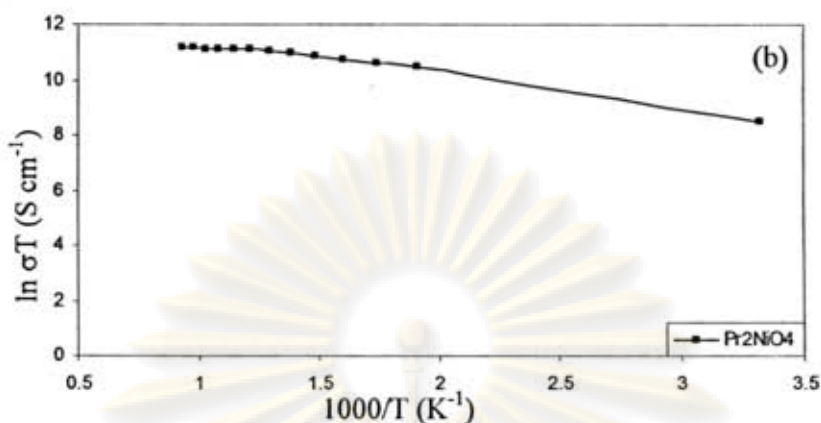
Figure 3.39 (a) Temperature dependence of the electrical conductivity (σ) for
Pr_2NiO_4.

(b) Arrhenius plot of the electrical conductivity of Pr_2NiO_4.

Figure 3.39 (a) shows the temperature dependence of the electrical conductivity (σ) for Pr_2NiO_4 ceramic. The electrical conductivity increases with measuring temperature through a maximum value of 82.5 Ω^{-1} cm^{-1} at 550 °C and then decreases. In the intermediate temperature range (600–800 °C), the specimen gives electrical conductivities of 79–67 Ω^{-1} cm^{-1}, roughly near to the application requirement ($\geq$100 Ω^{-1} cm^{-1}) for a cathode material of SOFC. The Arrhenius plot of Pr_2NiO_4 is given in Figure 3.39 (b). The linear part can be described by the small polaron conduction mechanism, following the formula: $\sigma = (A/T) \exp(-Ea/kT)$, where A is material constant including the carrier concentration term, Ea the activation energy, k the Boltzmann's constant and T is the absolute temperature. The activation energy calculated from the linear part of figure 3.39 (b) was 8.98 kJ/mol. The specimen displays an obvious transition in electrical conduction characteristic semiconductor-type.

It has been reported that the electrical conducting property of $Pr_2NiO_{4+\delta}$ can be further modified by substitution. The research is being carried out in our lab, aiming at enhancing the electrical conductivities of the material at intermediate temperatures by B site substitution (Cu, Co, Zn, In, Mg and Ga).

3.3.5.2 Electrical conductivity of $Pr_2Ni_{1-x}Cu_xO_4$ and Ga doped $Pr_2Ni_{1-x}Cu_xO_4$ compounds (x=0.1, 0.15, 0.3)

The temperature dependence of the electrical conductivity of the $Pr_2Ni_{1-x}Cu_xO_4$ (x=0.1, 0.15, 0.3) samples is shown in Figure 3.40 and Table 3.23.
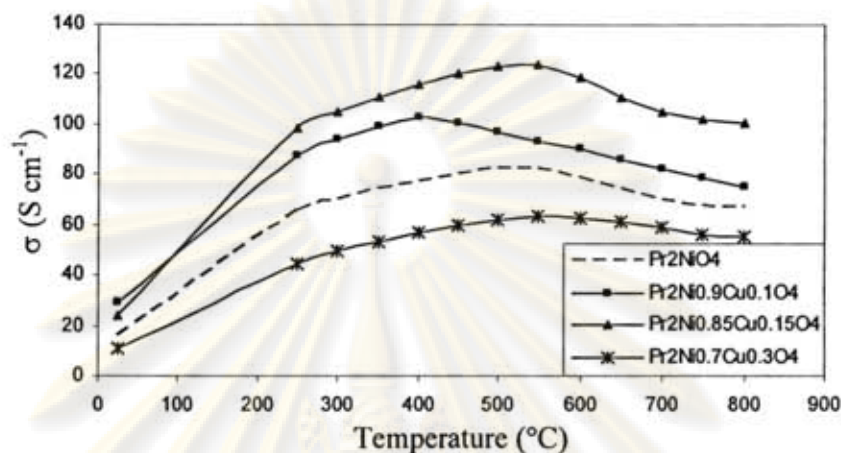
Figure 3.40 Temperature dependence of the electrical conductivity (σ) for Pr_2NiO_4 and $Pr_2Ni_{1-x}Cu_xO_4$ (x=0.1, 0.15, 0.3).

Table 3.23 The specific conductivity of Pr_2NiO_4 and $Pr_2Ni_{1-x}Cu_xO_4$ (x=0.1, 0.15, 0.3).

Sample	Specific conductivity, σ (S/cm)						
	300°C	400°C	500°C	600°C	700°C	800°C	σ_{max} (T,°C)
Pr_2NiO_4	69.9	77.5	82.4	79.1	70.1	67.2	82.5 (550)
$Pr_2Ni_{0.9}Cu_{0.1}O_4$	93.8	102.5	97.2	90.6	82.6	75.2	102.5 (400)
$Pr_2Ni_{0.85}Cu_{0.15}O_4$	104.7	116.2	123.6	118.6	105.1	100.7	123.7 (550)
$Pr_2Ni_{0.7}Cu_{0.3}O_4$	49.4	56.9	61.8	63.0	59.0	55.2	63.1 (550)

It can be found in Figure 3.40 and Table 3.23 that, upon heating, the conductivity increases with the increasing of temperature (semi-conductivity) and $Pr_2Ni_{0.85}Cu_{0.15}O_4$ reaches the maximum value of 123.74 S cm^{-1} at about 550 °C, after which, the conductivity begins to decrease (pseudometallic behavior). The decrease of the conductivity is mainly associated with the loss of the lattice oxygen and the reduction of the B-site iron ions at elevated temperature [54]. The conductivity of the sample significantly increased by the substitution of Cu for Ni up to 15 mol%, while a

further increase in the Cu amount caused a decrease in the conductivity. This decrease in conductivity can be explained by the formation of the secondary phases of Pr_6O_{11} (see sections 3.3.1.2 figure 3.2)

The activation energy of $Pr_2Ni_{1-x}Cu_xO_4$ (x=0.1, 0.15, 0.3) specimens calculated from the linear part of figure 3.40 were shown in table 3.24. The activation energy of $Pr_2Ni_{1-x}Cu_xO_4$ (x=0.1, 0.15) were lower than that of Pr_2NiO_4, but $Pr_2Ni_{0.7}Cu_{0.3}O_4$ was higher than Pr_2NiO_4.
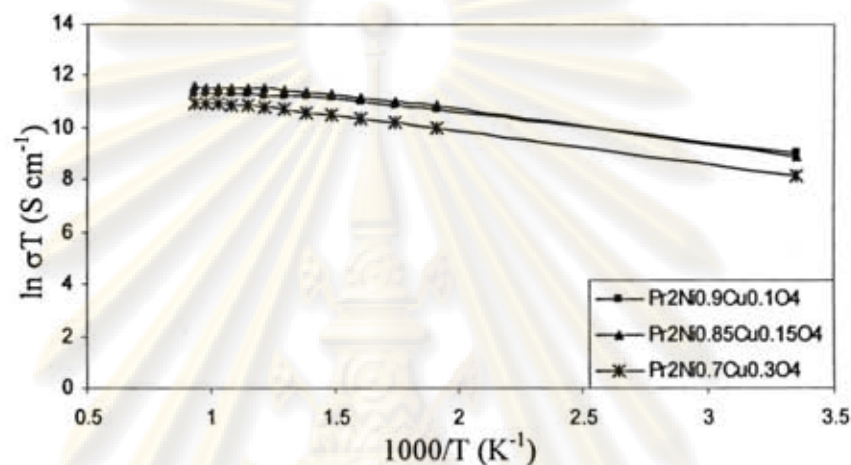
Figure 3.41 Arrhenius plot of the electrical conductivity of $Pr_2Ni_{1-x}Cu_xO_4$ (x=0.1, 0.15, 0.3).

Table 3.24 Activation energy of Pr_2NiO_4 and $Pr_2Ni_{1-x}Cu_xO_4$ (x=0.1, 0.15, 0.3).

Sample	E_a (kJ/mol)
Pr_2NiO_4	9.80
$Pr_2Ni_{0.9}Cu_{0.1}O_4$	9.35
$Pr_2Ni_{0.85}Cu_{0.15}O_4$	9.45
$Pr_2Ni_{0.7}Cu_{0.3}O_4$	10.11

Fig. 3.42 the temperature dependence of the electrical conductivity for $Pr_2Ni_{0.9}Cu_{0.1}O_4$ doped with Ga.
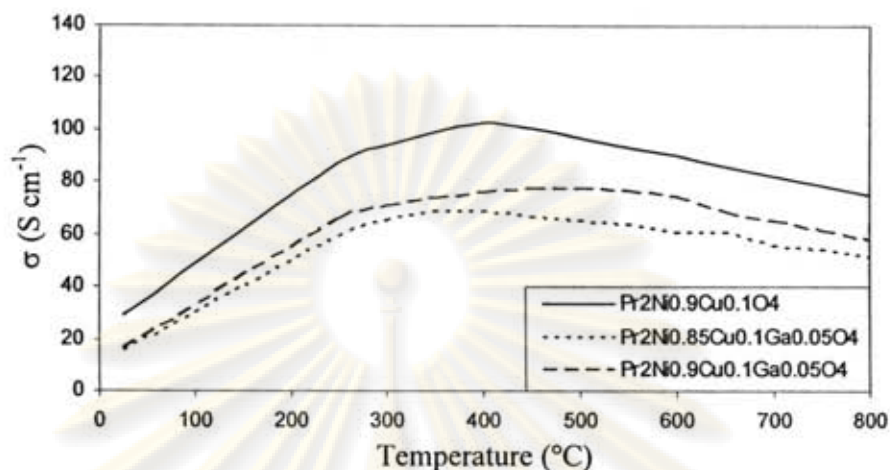
Figure 3.42 Temperature dependence of the electrical conductivity (σ) for $Pr_2Ni_{0.9}Cu_{0.1}O_4$, $Pr_2Ni_{0.85}Cu_{0.1}Ga_{0.05}O_4$ and $Pr_2Ni_{0.9}Cu_{0.1}Ga_{0.05}O_4$.

Ishihara *et al.* [52] mentioned that total conductivity in $Pr_2Ni_{1-x}Cu_xO_4$ can be decreased by doping Ga nonstoichiometric and further decreased by doping Ga stoichiometric composition. Since the oxygen desorption which related to oxygen permeation is much improved by doping excess amount of Ga, the oxygen permeation in this material is controlled by oxide ion conductivity and the electrical hole conductivity is much higher than that of the oxide ion conduction. Considering the ionic size and valence number, doped Ga may be enter at the vacancy site of Ni in Pr_2NiO_4 or interstitial site and it works primarily as the donor and generated electron. The formed electron decrease the hole concentration by the charge neutralization reaction resulting in the decreased electronic conductivity. In fact, total conductivity of $Pr_2Ni_{1-x}Cu_xO_4$ (x = 0.1, 0.15, 0.3) decreased by doping Ga. For example Ga doped $Pr_2Ni_{0.9}Cu_{0.1}O_4$ were shown in Figure 3.42.

3.3.5.3 Electrical conductivity of $Pr_2Ni_{1-x}Co_xO_4$ (x=0.1, 0.2, 0.3)

Figure 3.43 and Table 3.25 shows the temperature dependence of electrical conductivity of dense $Pr_2Ni_{1-x}Co_x O_4$ (x=0.1, 0.2, 0.3) in air.
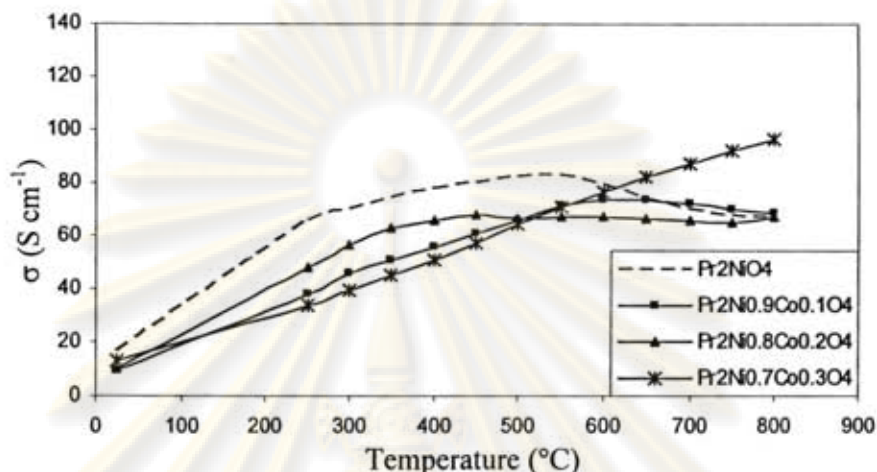
Figure 3.43 Temperature dependence of the electrical conductivity (σ) for Pr_2NiO_4 and $Pr_2Ni_{1-x}Co_x O_4$(x=0.1, 0.2, 0.3).

Table 3.25 The specific conductivity of Pr_2NiO_4 and $Pr_2Ni_{1-x}Co_xO_4$ (x=0.1, 0.2, 0.3)

Sample	Specific conductivity, σ (S/cm)						
	300°C	400°C	500°C	600°C	700°C	800°C	σ_{max} (T,°C)
Pr_2NiO_4	69.9	77.5	82.4	79.1	70.1	67.2	82.5 (550)
$Pr_2Ni_{0.9}Co_{0.1}O_4$	45.8	55.6	65.8	73.6	72.0	68.4	73.6 (600)
$Pr_2Ni_{0.8}Co_{0.2}O_4$	56.3	66.0	66.6	67.1	65.8	67.0	67.2 (550)
$Pr_2Ni_{0.7}Co_{0.3}O_4$	39.3	50.7	64.1	76.7	87.4	96.4	96.4 (800)

The conductivity of $Pr_2Ni_{1-x}Co_xO_4$ is relative low, the formation of oxide ion vacancies can cause a decrease in electrical conductivity. The vacancies also can act as random traps for electrons, resulting in the decrease of the carrier mobility [54], which will lead to the significantly decrease in charge carriers concentration. The conductivity increases with the increasing of temperature (semi-conductivity).

Shown in table 3.26, the activation energies of Co specimens were calculated from the linear part of figure 3.44. The activation energy of $Pr_2Ni_{1-x}Co_xO_4$ (x=0.1, 0.2, 0.3) was more than that of Pr_2NiO_4.
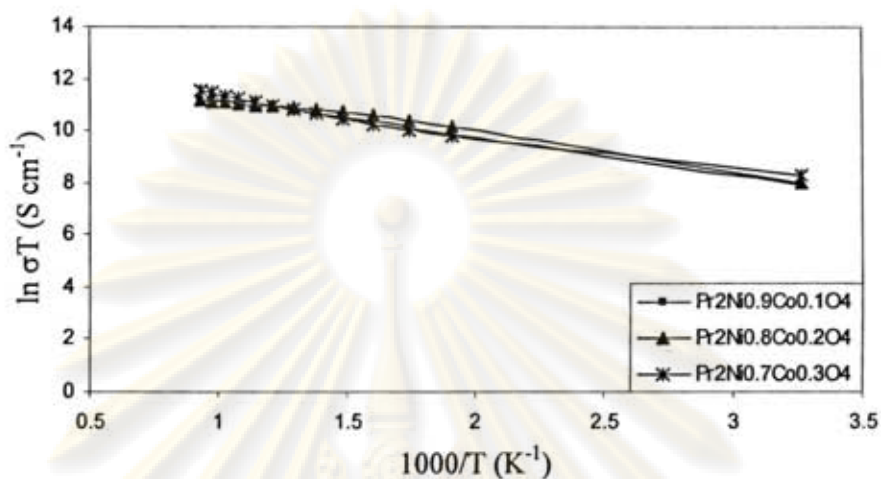
Figure 3.44 Arrhenius plot of the electrical conductivity of $Pr_2Ni_{1-x}Co_xO_4$ (x=0.1, 0.2, 0.3).

Table 3.26 Activation energy of Pr_2NiO_4 and $Pr_2Ni_{1-x}Co_xO_4$ (x=0.1, 0.2, 0.3).

Sample	E_a (kJ/mol)
Pr_2NiO_4	9.80
$Pr_2Ni_{0.9}Co_{0.1}O_4$	12.22
$Pr_2Ni_{0.85}Co_{0.2}O_4$	12.28
$Pr_2Ni_{0.7}Co_{0.3}O_4$	11.86

3.3.5.4 Electrical conductivity of $Pr_2Ni_{1-x}Zn_xO_4$ and Ga doped $Pr_2Ni_{1-x}Zn_xO_4$ compounds (x=0.1, 0.2, 0.3)

Figure 3.45 and Table 3.27 shows the temperature dependence of electrical conductivity of dense $Pr_2Ni_{1-x}Zn_x O_4$ (x=0.1, 0.2, 0.3) in air.
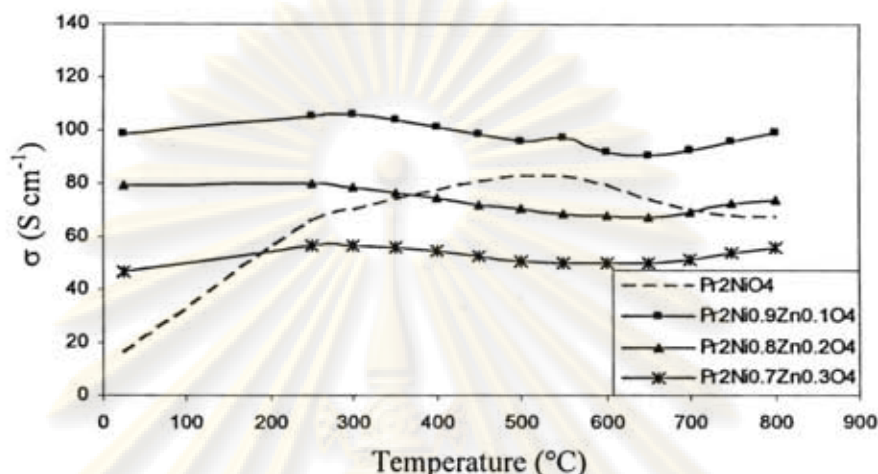
Figure 3.45 Temperature dependence of the electrical conductivity (σ) for Pr_2NiO_4 and $Pr_2Ni_{1-x}Zn_x O_4$ (x=0.1, 0.2, 0.3).

Table 3.27 The specific conductivity of Pr_2NiO_4 and $Pr_2Ni_{1-x}Zn_xO_4$ (x=0.1, 0.2, 0.3).

Sample	Specific conductivity, σ (S/cm)						
	300°C	400°C	500°C	600°C	700°C	800°C	σ_{max} (T,°C)
Pr_2NiO_4	69.9	77.5	82.4	79.1	70.1	67.2	82.5 (550)
$Pr_2Ni_{0.9}Zn_{0.1}O_4$	105.8	101.6	96.2	91.8	92.7	99.6	105.8 (300)
$Pr_2Ni_{0.8}Zn_{0.2}O_4$	79.0	74.4	70.3	68.1	69.4	74.3	80.0 (250)
$Pr_2Ni_{0.7}Zn_{0.3}O_4$	56.9	54.5	50.8	50.1	51.1	56.1	56.9 (300)

From Figure 3.45 and Table 3.27, $Pr_2Ni_{0.9}Zn_{0.1}O_4$ reaches the maximum value of 105.8 S cm^{-1} at about 300°C, the conductivity decreased with increasing Zn contents. The decrease in conductivity of $Pr_2Ni_{1-x}Zn_xO_4$ is largely due to firstly, high vacancy concentration in $Pr_2Ni_{1-x}Zn_xO_4$ lattice. As discussed above (see section 3.3.3.4 and 3.3.4.4), there is large concentration of oxygen vacancy, which will lead to the significantly decrease in charge carriers concentration. Because of the vacancies also can act as the scattering centers, or as random traps for electrons,

resulting in the decrease of the carrier mobility [54].The second reason can be ascribed to the fact that zinc holds fixed bivalent state, which will not contribute to conductivity. With zinc doping in B-sites, the conductivity will decrease as expected, due to the decrease of the total concentration of B-sites that participate in the electronic transport processes.

The activation energy of $Pr_2Ni_{1-x}Zn_xO_4$ (x=0.1, 0.2, 0.3) specimens calculated from the linear part of Figure 3.46 were shown in Table 3.28. The activation energy of $Pr_2Ni_{1-x}Zn_xO_4$ (x=0.1, 0.2, 0.3) were lower than that of Pr_2NiO_4.
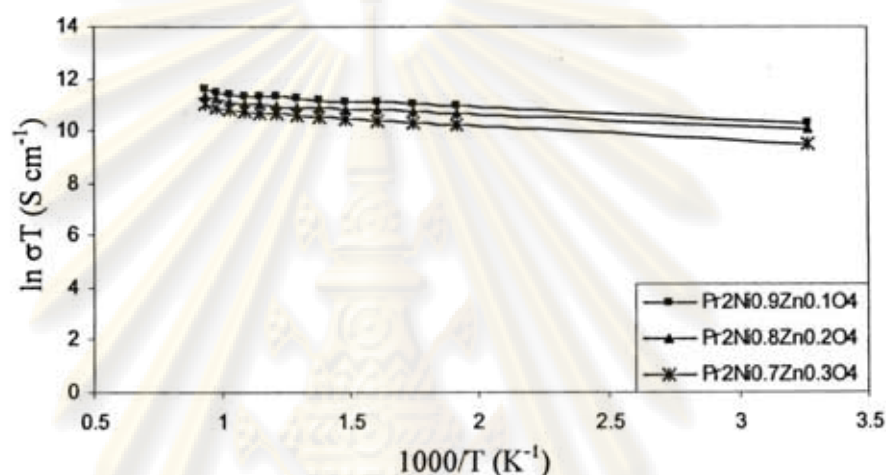
Figure 3.46 Archeries plot of the electrical conductivity of $Pr_2Ni_{1-x}Zn_xO_4$ (x=0.1, 0.2, 0.3).

Table 3.28 Activation energy of Pr_2NiO_4 and $Pr_2Ni_{1-x}Zn_xO_4$ (x=0.1, 0.2, 0.3).

Sample	E_a (kJ/mol)
Pr_2NiO_4	9.80
$Pr_2Ni_{0.9}Zn_{0.1}O_4$	3.84
$Pr_2Ni_{0.8}Zn_{0.2}O_4$	3.85
$Pr_2Ni_{0.7}Zn_{0.3}O_4$	4.39

The temperature dependence of the electrical conductivity of $Pr_2Ni_{0.9}Zn_{0.1}O_4$ and Ga doped $Pr_2Ni_{0.9}Zn_{0.1}O_4$ compounds at temperature in range 100-800°C are shown in Figure 3.47.
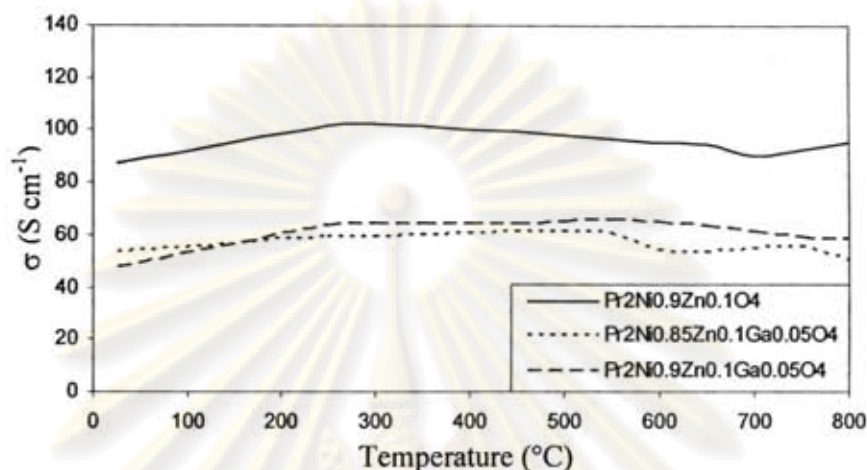
Figure 3.47 Temperature dependence of the electrical conductivity (σ) for $Pr_2Ni_{0.9}Zn_{0.1}O_4$, $Pr_2Ni_{0.85}Zn_{0.1}Ga_{0.05}O_4$ and $Pr_2Ni_{0.9}Zn_{0.1}Ga_{0.05}O_4$.

Figure 3.47 show the result of Ga doped $Pr_2Ni_{0.9}Zn_{0.1}O_4$, Ga doped at B-site of $Pr_2Ni_{1-x}Zn_xO_4$ which is similar to that of Ga doped $Pr_2Ni_{1-x}Cu_xO_4$. It exhibited the lower value of electrical conductivity in Ga–doped and Ga excess doped $Pr_2Ni_{1-x}Zn_xO_4$ more than that of Ga–undoped oxide. When Ga^{3+} ion substituted Ni^{2+} ion, it generated electron. The formed electron decrease the hole concentration by the charge neutralization reaction resulting in the decreased electrical conductivity.

3.3.5.5 Electrical conductivity of $Pr_2Ni_{1-x}In_xO_4$ and Ga doped $Pr_2Ni_{1-x}In_xO_4$ compounds (x=0.1, 0.2, 0.3)

The temperature dependence of the electrical conductivity of the $Pr_2Ni_{1-x}In_xO_4$ (x=0.1, 0.2, 0.3) samples is shown in Figure 3.48 and Table 3.29.
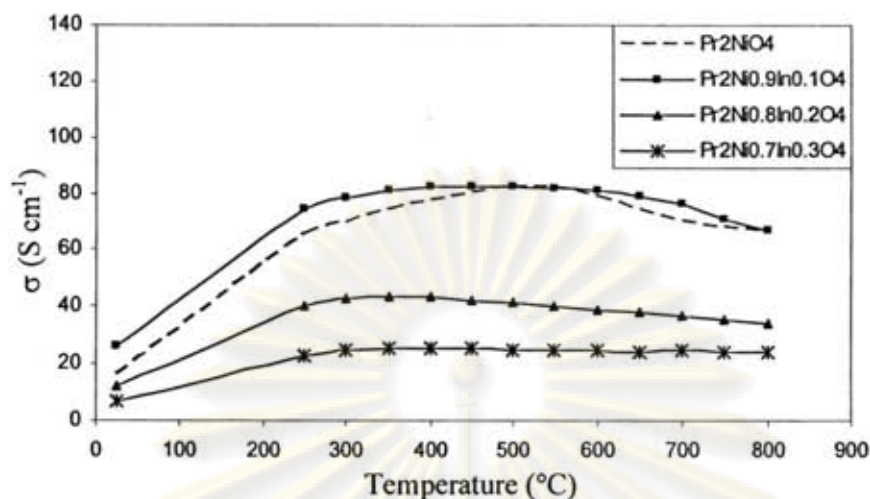
Figure 3.48 Temperature dependence of the electrical conductivity (σ) for Pr_2NiO_4 and $Pr_2Ni_{1-x}In_x O_4$ (x=0.1, 0.2, 0.3).

Table 3.29 The specific conductivity of Pr_2NiO_4 and $Pr_2Ni_{1-x}In_xO_4$ (x=0.1, 0.2, 0.3).

Sample	Specific conductivity, σ (S/cm)						
	300°C	400°C	500°C	600°C	700°C	800°C	σ_{max} (T,°C)
Pr_2NiO_4	69.9	77.5	82.4	79.1	70.1	67.2	82.5 (550)
$Pr_2Ni_{0.9}In_{0.1}O_4$	78.7	82.1	82.2	80.8	76.1	67.1	82.2 (500)
$Pr_2Ni_{0.8}In_{0.2}O_4$	42.7	43.5	41.3	39.0	37.0	34.4	43.6 (350)
$Pr_2Ni_{0.7}In_{0.3}O_4$	24.8	25.7	24.9	24.8	24.6	24.0	25.7 (400)

Table 3.29 shows the negative impact of In–doped Pr_2NiO_4. The conductivity of the perovskite–like oxide decrease with the increasing of In.

The reason can be ascribed to the fact that In holds fixed trivalent state, which will not contribute to conductivity. Similar results were observed in Zn doped Pr_2NiO_4 system; the conductivity decreased with the increase of the Zn content. With indium doping in B-sites, the conductivity will decrease as expected, due to the decrease of the total concentration of B-sites that participate in the electronic transport processes. The conductivity increases with the increasing of temperature (semi-conductivity), afterwards, the conductivity begins to decrease (pseudometallic behavior).

In Table 3.30, the activation energies of In doped Pr_2NiO_4 were calculated from linear part of Arrhenius plots in Figure 3.49. Similar to $Pr_2Ni_{1-x}Cu_xO_4$ specimens, the activation energy increased with increasing the amount of In.
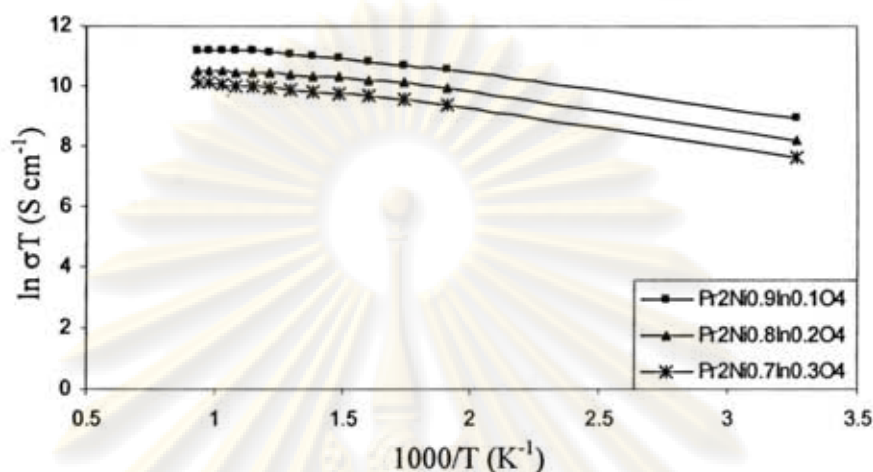
Figure 3.49 Arrhenius plot of the electrical conductivity of $Pr_2Ni_{1-x}In_xO_4$ (x=0.1, 0.2, 0.3).

Table 3.30 Activation energy of Pr_2NiO_4 and $Pr_2Ni_{1-x}In_xO_4$ (x=0.1, 0.2, 0.3).

Sample	E_a (kJ/mol)
Pr_2NiO_4	9.80
$Pr_2Ni_{0.9}In_{0.1}O_4$	8.58
$Pr_2Ni_{0.8}In_{0.2}O_4$	9.54
$Pr_2Ni_{0.7}In_{0.3}O_4$	9.72

3.3.5.6 Electrical conductivity of $Pr_2Ni_{0.9}Mg_{0.1}O_4$ and Ga doped $Pr_2Ni_{0.9}Mg_{0.1}O_4$ compounds

The temperature dependence of the electrical conductivity of the $Pr_2Ni_{0.9}Mg_{0.1}O_4$ samples is shown in Figure 3.50 and Table 3.31.
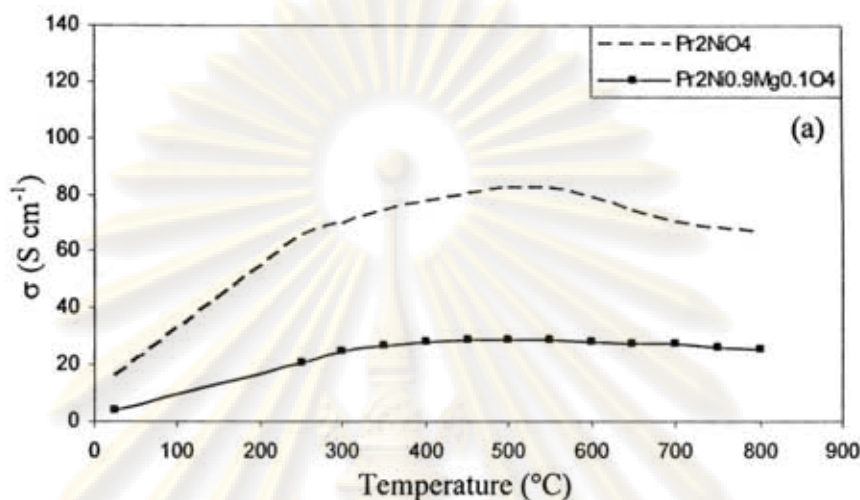
Figure 3.50 Temperature dependence of the electrical conductivity (σ) for Pr_2NiO_4 and $Pr_2Ni_{0.9}Mg_{0.1}O_4$.

Table 3.31 The specific conductivity of Pr_2NiO_4 and $Pr_2Ni_{0.9}Mg_{0.1}O_4$.

Sample	Specific conductivity, σ (S/cm)						
	300°C	400°C	500°C	600°C	700°C	800°C	σ_{max} (T,°C)
Pr_2NiO_4	69.9	77.5	82.4	79.1	70.1	67.2	82.5 (550)
$Pr_2Ni_{0.9}Mg_{0.1}O_4$	24.6	28.2	28.6	28.2	27.2	25.6	28.6 (500)

The decrease in conductivity observed at higher temperatures for the magnesium compositions could be due to the formation of significant amount of oxide ion vacancies at higher temperatures as indicated by the TGA (see section 3.3.3.6) and TPD data (see section 3.3.4.6). The formation of oxide ion vacancies can cause a decrease in electrical conductivity due to a decrease in the charge carrier concentration [53]. The conductivity of Pr_2NiO_4 was reported as about 82.54 S cm^{-1} at 550 °C. With magnesium doping in B-sites, the conductivity will decrease as expected. The conductivity increases with the increasing of temperature (semi-

conductivity) after which, the conductivity begins to decrease (pseudometallic behavior).

The activation energy calculated from the linear part of figure 3.51 was 13.10 kJ/mol. The activation energy of $Pr_2Ni_{0.9}Mg_{0.1}O_4$ was higher than that of Pr_2NiO_4.
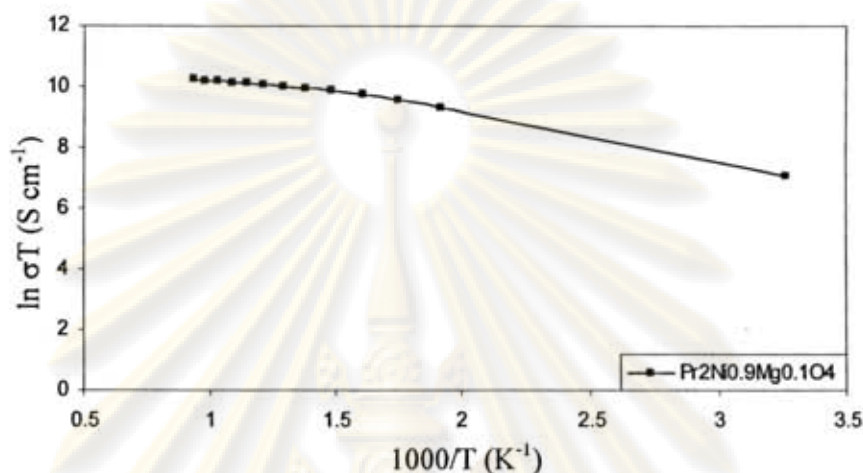
Figure 3.51 Arrhenius plot of the electrical conductivity of $Pr_2Ni_{0.9}Mg_{0.1}O_4$.

Figure 3.51 exhibited the effect of Ga doped $Pr_2Ni_{0.9}Mg_{0.1}O_4$ on the electrical conductivity. The temperature dependence of the electrical conductivity of $Pr_2Ni_{0.9}Mg_{0.1}O_4$ was compared to $Pr_2Ni_{0.85}Mg_{0.1}Ga_{0.05}O_4$ and $Pr_2Ni_{0.9}Mg_{0.1}Ga_{0.05}O_4$.
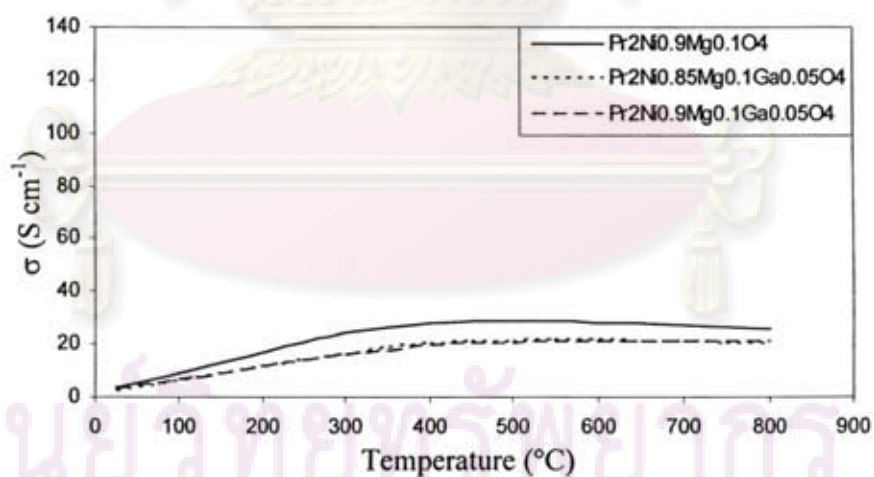
Figure 3.52 Temperature dependence of the electrical conductivity (σ) for $Pr_2Ni_{0.9}Mg_{0.1}O_4$, $Pr_2Ni_{0.85}Mg_{0.1}Ga_{0.05}O_4$ and $Pr_2Ni_{0.9}Mg_{0.1}Ga_{0.05}O_4$.

As mentioned previously, when Ga^{3+} ion substituted Ni^{2+} ion, it generated electron. The formed electron decrease the hole concentration by the charge neutralization reaction resulting in the decreased electronic conductivity. In the case of $Pr_2Ni_{0.9}Mg_{0.1}O_4$, it exhibited that total conductivity of the sample decreased by doping Ga as shown in Figure 3.52.

After examining the effect of doping various metal ions with different contents at B site of Pr_2NiO_4, the study reveals that $Pr_2Ni_{0.85}Cu_{0.15}O_4$ achieved highest values of electrical conductivity at intermediate temperature (123.7 S/cm at 550°C). $Pr_2Ni_{0.9}Zn_{0.1}O_4$ and $Pr_2Ni_{0.9}Cu_{0.1}O_4$ also show the satisfactory results. Interestingly, the electrical conductivity of Pr_2NiO_4 can be improved by doping metal with +2 oxidation state. Doping B site with second metal (Ga^{3+}) cause the negative effect to the conductivity of the material.

CHAPTER IV

CONCLUSIONS

4.1 Conclusions

The perovskite K_2NiF_4-type oxides in the system $Pr_2Ni_{1-x}M_xO_4$, $Pr_2Ni_{1-x-0.05}M_xGa_{0.05}O_4$ and $Pr_2Ni_{1-x}M_xGa_{0.05}O_4$ doped with various compositions of Cu, Co, Zn, In and Mg ions at B site were synthesized by modified citrate method.

XRD patterns of $Pr_2Ni_{1-x}M_xO_4$ except $Pr_2Ni_{1-x}Mg_xO_4$ (x= 0.2, 0.3), $Pr_2Ni_{1-x-0.05}Co_xGa_{0.05}O_4$ and $Pr_2Ni_{1-x}Co_xGa_{0.05}O_4$ (x=0.2, 0.3) revealed that the main phase of K_2NiF_4-type structure. The trace amount of impurity phase (Pr_6O_{11}) formation was also observed at $2\theta=28°$. It is seen that the amount of the Pr_6O_{11} phase increased with the increasing amount of metal substituted at Ni site. The ionic radius of Cu^{2+}, Co^{2+} Zn^{2+}, In^{3+} and Mg^{2+}, were higher than that of Ni^{2+}, so the substitution of metal ions for Ni^{2+} in B-site of Pr_2NiO_4 induce a little slightly shift to lower angle of 2θ and slightly expansion of lattice crystal. On the other hand, the substitution of Ga^{3+} ions for Ni^{2+} in B-site of Pr_2NiO_4 induce a little slightly shift to high angle of 2θ because the ionic radius of Ga^{3+} was lower than that of Ni^{2+} leading to shrinkage of the lattice.

The morphologies of the perovskite membranes were characterized by SEM. The results of the perovskite disc except $Pr_2Ni_{1-x}Mg_xO_4$ (x = 0.2, 0.3) appear uniform, crack–free and high density after sintered at 1300°C. The grain size slightly increased with the increasing content of Cu, Co and slightly decreased with the increasing content of In. It is shown that Ga contents in $Pr_2Ni_{1-x}M_xO_4$ did not affect the density and morphology of membrane.

Oxygen permeation property was determined by thermogravimetric analysis (TGA) and oxygen temperature-programmed desorption (O_2-TPD). TGA results showed that the weight loss of oxygen of $Pr_2Ni_{1-x}M_xO_4$ especially $Pr_2Ni_{0.9}Mg_{0.1}O_4$ was higher than that of Pr_2NiO_4. The extent of oxygen loss except In contents increases with increasing metal ions contents in $Pr_2Ni_{1-x}M_xO_4$. In the case of Ga–doped $Pr_2Ni_{1-x}M_xO_4$, it is observed that Ga^{3+} ion addition has an effect on higher capability to accommodate excess oxygen. It exhibited gain weight of oxygen in stoichiometric more than nonstoichiometric composition. It indicated that the weight

loss of Ga–doped less than Ga–undoped $Pr_2Ni_{1-x}M_xO_4$. For O_2-TPD measurement, the results show that the amounts of the β oxygen desorption of $Pr_2Ni_{1-x}M_xO_4$ except In contents increased with the increasing amount of metal doped at Ni site. $Pr_2Ni_{0.7}Zn_{0.3}O_4$ has total oxygen desorption 0.280 mmol/g in the range of 100-700°C which show the highest oxygen desorption property. Ga-doped in $Pr_2Ni_{1-x}M_xO_4$ exhibited the increase amount of oxygen desorption more than that of Ga-undoped composition. From TGA and O_2-TPD, It is concluded that the amounts of the oxygen permeation increased with the increasing amount of metal doped at Ni site, except $Pr_2Ni_{1-x}In_xO_4$ and Ga–doped $Pr_2Ni_{1-x}M_xO_4$ stoichiometric compositions show the highest increase of oxygen desorption value.

The electrical conductivity of Pr_2NiO_4 was improved by doping Cu and Zn at Ni site, especially doping 15% Cu. The conductivity property decreased with increasing the amount of Zn and In. The $Pr_2Ni_{0.85}Cu_{0.15}O_4$ ceramic exhibits an electrical conductivity of 123.7 $S^{-1}cm^{-1}$ at 550°C, which is about 50% higher than that of Pr_2NiO_4 (82.5 $S^{-1}cm^{-1}$ at 550°C). However, Ga–doped at the B site ions decreased the electrical conductivity in stoichiometric and nonstoichiometric compositions. When Ga^{3+} ion enter at the vacancy site of Ni in Pr_2NiO_4 or interstitial site, it generated electron. The formed electron decrease the hole concentration by the charge neutralization reaction resulting in the decreased electronic conductivity.

In conclusion, $Pr_2Ni_{0.85}Cu_{0.15}O_4$ (electrical conductivity is 123.7 S/cm at 550°C and the oxygen desorption from 100°C up to 700°C is 0.180 mmolO_2/g) is a good candidate for SOFC cathode material.

4.2 Suggestions

From experiment results, the future work should be focused on the follwing:

1. To determine thermal expansion coefficient (TEC) of $Pr_2Ni_{0.85}Cu_{0.15}O_4$ specimen by dilatometer technique for fuel cell application.
2. To study of the performance of $Pr_2Ni_{0.85}Cu_{0.15}O_4$ specimen used as a cathode on the single cell.

REFERENCES

[1] Neophytides, S. G.; Paloukis, F. Numerical simulation of methane fuelled cogenerative SOFCs for the production of synthesis gas and electrical energy. *Chemical Engineering Science* 62(2007): 3868-3881.

[2] Serra, J. M.; Buchkremer, H. P. On the nanostructuring and catalytic promotion of intermediate temperature solid oxide fuel cell (IT-SOFC) cathodes. *Journal of Power Source* 172(2007): 768-774.

[3] Zhu, J. H.; Goodenough, J. B.; Wan, J. $Nd_{2-x}La_xNiO_{4+\delta}$, a mixed ionic/electronic conductor with interstitial oxygen, as a cathode material. *Solid State Ionics* 178(2007): 281–286.

[4] Aguadero, A.; Perez M.; Alonso, J. A.; Daza, L. Neutron powder diffraction study of the influence of high oxygen pressure treatments on $La_2NiO_{4+\delta}$ and structural analysis of $La_2Ni_{1-x}Cu_xO_{4+\delta}$ ($0 \leq x \leq 1$). *Journal of Power Source* 151(2005): 52-56.

[5] Ullmann, H.; Daroukh, M. A.; Vashook, V.V.; Tietz, F.; Raj, I. A. Oxides of the AMO_3 and A_2MO_4-type: structural stability, electrical conductivity and thermal expansion. *Solid State Ionics* 158(2003): 141-150.

[6] Yang, X.; Zhu, J.; Zhao, Z.; Xiao, D.; Li, J.; Wu, Y. Study of $La_{2-x}Sr_xCuO_4$ (x = 0.0, 0.5, 1.0) catalysts for NO+CO reaction from the measurements of O_2-TPD, H_2-TPR and cyclic voltammetry. *Journal of Molecular catalysis A: Chemical* 238(2005): 35–40.

[7] Bhide, S. V., Meng, W., and Virkar, A. V. *Stability of Mixed Perovskite Proton Conductors*. Department of Materials Science & Engineering, University of Utah, 1999.

[8] Yakokawa, H.; Sakia, N.; Kawada, T.; Dokiya, M. Thermodynamic Stabilities of Perovskite Oxides for Electrodes and other Electrochemical Materials. *Solid State Ionics* 52(1992): 43-56.

[9] Yakokawa, H.; Kawada, T.; Dokiya, M. Thermodynamic Regularities in Perovskite and K_2NiF_4 Compounds. *Journal of American Ceramic Society* 72(1989): 152-157.

[10] Gschneider, K. A. Jr., and Eyring, L. *Handbook of the Physics and Chemistry of Rare Earths*, Amsterdam: North-Holland Publishers, p553, 1979.

[11] Rao, C. N. R.; Gopalakrishnan, J.; Vidyasagar, K. Superstructure, ordered defects and nonstoichiometry in metal oxides of perovskite and related structure. *Indian Journal of Chemistry* 23A(1984): 265-284.

[12] Teraoka, Y.; Nobunaga, T.; Yamazoe, N. Effect of cation substitution on the oxygen semipermeability of perovskite-type oxide. *Chemistry Letters* (*1988*): 503-506.

[13] Goodenough, J. B., and Longo J. M. *Crystallographic and Magnetic Properties of Perovskite and Perovskite-related Compounds*. Landholt-Bornstein Numerical Data and Functional Relationships in Science and Technology New Series Group III/vol. 4a, Spinger-Verlag, Berlin-Heiderberg, 1970.

[14] Yeyongchaiwat, J. *Synthesis and Characterization of $La_{1-x}Sr_xGa_{1-y}Fe_yO_{3-\delta}$ Perovskite Membrane*. Doctoral dissertation, Department of Chemical Technology, Faculty of Science, Chulalongkorn University, 2002.

[15] Peña, M. A.; Fierro, J. L. G. Chemical Structures and Performance of Perovskite Oxides. *Chemical Reviews* 101(2001): 1981-2017.

[16] Tejuca, L. G., and Fierro, J. L. G. *Properties and Applications of Perovskite-type Oxides*. New York: Marcel Dekker, Inc., 3p, 1993.

[17] Yamazoe, N.; Teraoka, Y.; Seiyama, T. TPD and XPS Study on Thermal Behavior of Adsorbed Oxygen in $La_{1-x}Sr_xCoO_3$. *Chemistry Letters* (1981): 1767.

[18] Yokoi, Y.; Uchida, H. Catalytic Activity of Perovskite-Type Oxide Catalysts for Direct Decomposition of NO: Correlation Between Cluster Model Calculations and Temperature-Programmed Desorption Experiments. *Catalysis Today* 42(1998): 167-174.

[19] Wu Y.; Yang X.; Zhao Z. Comparative study of Nickel-based perovskite-like mixed oxide catalysts for direct decomposition of NO. *Applied Catalysis B: Environmental* 8(1996): 281-297.

[20] Yang, X.; Zhu, J.; Zhao, Z.; Xiao, D.; Li, J.; Wu, Y. Study of $La_{2-x}Sr_xCuO_4$ ($x = 0.0, 0.5, 1.0$) catalysts for NO+CO reaction from the measurements of O_2-TPD, H_2-TPR and cyclic voltammetry. *Journal of Molecular catalysis A: Chemical* 238(2005): 35–40.

[21] Yang, N.; Li, C.; Hu, T.; Zhang, H.; Chen, Y.; Jin, J. Preparation and characterization of supported dense oxygen permeating membrane of mixed conductor $La_2NiO_{4+\delta}$. *Journal of Membrane Science* 226(2003): 1-7.

[22] Reed, J. S. *Introduction of the Principles of Ceramic Processing*. John-Wiley & Sons, New York, 1985.

[23] Pechini, M. *Method of Preparing Lead and Alkaline-earth Titanates and Niobates and Coating Method Using the Same to Form a Capacitor*. U. S., 1976.

[24] Nagamoto, H.; Hayashi, K.; Inoue, H. Methane Oxidation by Oxygen Transported Through Solid Electrolyte. *Journal of Catalysis* 126 (1990): 671-673.

[25] Gellings, P. J.; Bouwmeester, H. J. M. Ion and Mixed Conducting Oxides as Catalysts. *Catalysis Today* 12(1992): 1-91.

[26] Richerson, D. W. *Modern Ceramic Engineering, Properties, Processing, and Use in Design*, 2nd ed., p378-381, 1992.

[27] Ordier, P.; Allancon, Ch.; Bassat J.M. Oxygen Exchange in $Pr_2NiO_{4+\delta}$ at High Temperature and Direct Formation of $Pr_4Ni_3O_{10-x}$. *Journal of Solid State Chemistry* 153(2000): 381-385.

[28] Kharton, V.V.; Viskup, A.P.; Kovalevsky, A.V.; Naumovich, E.N.; Marques, F.M.B. Ionic transport in oxygen-hyperstoichiometric phases with K_2NiF_4-type structure. *Solid State Ionics* 143(2001): 337-353.

[29] Kilner, J.A.; Shaw C. K. M. Mass transport in $La_2Ni_{1-x}Co_xO_{4+\delta}$ oxides with the K_2NiF_4 structure. *Solid State Ionics* 154-155(2002): 523-527.

[30] Skinner, S.J. Characterisation of $La_2NiO_{4+\delta}$ using in-situ high temperature neutron powder diffraction. *Solid State Sciences* 5(2003): 419-426.

[31] Whitfield, P.S.; Amow, G.; Davidson, I.J.; Hammond R.P.; Munnings C.N.; Skinner S.J. Structural and sintering characteristics of the $La_2Ni_{1-x}Co_xO_{4+\delta}$ series. *Ceramics International* 30(2004): 1635–1639.

[32] Kharton, V.V.; Yaremchenko, A. A.; Shaula, A. L.; Patrakeev, M. V.; Naumovich, E. N.; Logvinovich, D. I.; Frade, J. R.; Marquesa F. M. B. Transport properties and stability of Ni-containing mixed conductors with perovskite- and K_2NiF_4-type structure. *Journal of Solid State Chemistry* 177(2004): 26–37.

[33] Fontaine, M.L.; Laberty-Robert, C.; Ansart, F.; Tailhades P. Composition and porosity graded $La_{2-x}NiO_{4+\delta}$ ($x \geq 0$) interlayers for SOFC: Control of the microstructure via a sol–gel process. *Journal of Power Sources* 156(2006): 33–38.

[34] Xu, Q.; Huang, D.; Zhang, F.; Chen, W.; Liu, H.; Zhou, J. Synthesis and electrical conductivity of $La_2NiO_{4+\delta}$ derived from a polyamino-carboxylate complex precursor. *Materials Letters* 60(2006): 1892–1895.

[35] Ishihara, T.; Miyoshi, S.; Furuno,T.; Sanguanruang, O,; Matsumoto, H. Mixed conductivity and oxygen permeability of doped Pr_2NiO_4-based oxide. *Solid State Ionics* 177(2006): 3087–3091.

[36] Vashook, V.; Zosel, J.; Wen, T.; Guth, U. Transport properties of the $Pr_{2-x}Sr_xNiO_{4\pm\delta}$ ceramics with x=0.3 and 0.6. *Solid State Ionics* 177(2006): 1827–1830.

[37] Miyoshi, S.; Furuno, T.; Matsumoto, H.; Ishihara, T. Conductivity and oxygen permeability of a novel oxide$Pr2Ni_{0.8-x}Cu_{0.2}Fe_xO_4$ and its application to partial oxidation of CH_4.*Solid State Ionics* 177(2006): 2269–2273.

[38] Wen, T.-L.; Nie, H.W.; Wang, S.R.; Wang Y.S.; Guth, U.; Vashook, V. Preparation, thermal expansion, chemical compatibility, electrical conductivity and polarization of $A_{2-\alpha}A'_\alpha MO_4$ (A=Pr, Sm; A'=Sr; M=Mn, Ni; α=0.3, 0.6) as a new cathode for SOFC. *Solid State Ionics* 177(2006) 1929–1932.

[39] Kharton, V.V.; Tsipis, E.V.; Naumovich, E.N.; Patrakeev, M.V.; Waerenborgh, J.C.; Pivak, Y.V.; Gaczynski, P. Oxygen non-stoichiometry and defect thermodynamics in $La_2Ni_{0.9}Fe_{0.1}O_{4+\delta}$. *Journal of Physics and Chemistry of Solids* 68(2007): 1443–1455.

[40] Kovalevsky, A.V.; Kharton, V.V.; Yaremchenko,A.A.; Pivak, Y.V.; Naumovich, E.N.; Frade, J.R. Stability and oxygen transport properties of $Pr_2NiO_{4+\delta}$ ceramics. *Journal of the European Ceramic Society* 27 (2007): 4269–4272.

[41] Aguadero, A.; Alonso, J.A.; Fern´andez-D´ıaz, M.T.; Escudero, M.J.; Dazaa,L. In situ high temperature neutron powder diffraction study of $La_2Ni_{0.6}Cu_{0.4}O_{4+\delta}$ in air: Correlation with the electrical behaviour. *Journal of Power Sources* 169(2007): 17–24.

[42] Ishihara, T.; Miyoshi, S.; Matsumoto, H.; Furuno, T.; Sangoanruang, O. Mixed Conductivity and Oxygen Permeability of Doped Pr_2NiO_4-Based Oxides. *Journal of The Electrochemical Society* 154(1)(2007): B57-B62.

[43] Rodríguez-Martínez, L. M.; Vidal, K.; Ortega-San-Martín, L.; Díez-Linaza, E.; Nó, M. L.; Rojo, T.; Laresgoiti, A.; Arriortua, M. I. Isolating the effect of doping in the structure and conductivity of $(Ln_{1-x}M_x)FeO_{3-\delta}$ perovskites. *Solid State Ionics* 178(2007): 1310–1316.

[44] Kharton, V.V.; Shaulo, A.L.; Viskup, A.P.; Avdeev, M.; Yaremchenko, A.A.; Patrakeev, M.V.; Kurbakov, A.I.; Naumovich, E.N.; Marques,F.M.B. Perovskite-like system $(Sr,La)(Fe,Ga)O_{3-\delta}$: structure and ionic transport under oxidizing conditions. *Solid State Ionics* 150(2002): 229– 243.

[45] Manthiram, A.; Lee, K.T. Characterization of $Nd_{0.6}Sr_{0.4}Co_{1-y}Fe_yO_{3-\delta}$ ($0\leq y\leq0.5$) cathode materials for intermediate temperature solid oxide fuel cells. *Solid State Ionics* 176(2005): 1521 – 1527.

[46] Kharton, V.V.; Naumovich, E.N.; Patrakeev, M.V.; Yaremchenko, A.A.; Logvinovich, D.I.; Marques F.M.B. Oxygen nonstoichiometry in $La_2Ni(M)O_{4+\delta}$ (M = Cu, Co) under oxidizing conditions. *Solid State Sciences* 7(2005): 1353–1362.

[47] Aguadero, A.; Perez M.; Alonso, J. A.; Daza, L. Neutron powder diffraction study of the influence of high oxygen pressure treatments on $La_2NiO_{4+\delta}$ and structural analysis of $La_2Ni_{1-x}Cu_xO_{4+\delta}$ ($0 \leq x \leq 1$). *Journal of Power Source* 151(2005): 52-56.

[48] Manthiram, A.; Lee, K.T. Effect of cation doping on the physical properties and electrochemical performance of $Nd_{0.6}Sr_{0.4}Co_{0.8}M_{0.2}O_{3-\delta}$ (M=Ti, Cr, Mn, Fe, Co, and Cu) cathodes. *Solid State Ionics* 178(2007): 995–1000.

[49] Lee, M.-D.; Ling, T.-R., Chen, Z.-B. Catalytic behavior and electrical conductivity of $LaNiO_3$ in ethanol oxidation. *Applied Catalysis A: General* 136(1996): 191-203.

[50] Moseley, P.T., Norris J.O.W., and Williams, D.E. *Techniques and Mechanism in Gas Sensing* Adam Hilger, Bristol, p. 53,1990.

[51] Dai, H.; Niu, J.; Deng, J.; Liu, W.; Zhang, L.; Wang, G.; He, H.; Zi, X. Nanosized perovskite-type oxides $La_{1-x}Sr_xMO_{3-\delta}$ (M = Co, Mn; x = 0, 0.4) for the catalytic removal of ethylacetate. *Catalysis Today* 126(2007): 420–429.

[52] Ishihara, T.; Nakashima, K.; Okada, S.; Enoki, M.; Matsumoto, H. *Defect chemistry and oxygen permeation property of $Pr_2Ni_{0.75}Cu_{0.25}O_4$ oxide doped with Ga* [online]. 2007. Available from: http://www.sciencedirect.com

[53] Manthiram, A.; Lee, K.T. Synthesis and characterization of $Nd_{0.6}Sr_{0.4}Co_{1-y}Mn_yO_{3-\delta}$ ($0 \leq y \leq 1.0$) cathodes for intermediate temperature solid oxide fuel cells. *Journal of Power Sources* 158(2006): 1202–1208.

[54] Wei, B.; Lu, Z.; Huang, X.; Liu, M.; Li, N. Su,W. Synthesis, electrical and electrochemical properties of $Ba_{0.5}Sr_{0.5}Zn_{0.2}Fe_{0.8}O_{3-\delta}$ perovskite oxide for IT-SOFC cathode. *Journal of Power Sources* 176(2008): 1–8.

APPENDICES

ศูนย์วิทยทรัพยากร
จุฬาลงกรณ์มหาวิทยาลัย

APPENDICES

APPENDICE A
Tolerance number

Goldschmidt (1926) defined the tolerance limits of the size of ions through a tolerance factor, t as Equation (A.1)

$$t = (r_A + r_O)/ [\sqrt{2}\, (r_B + r_O)] \qquad (A.1)$$

where r_A, r_B, and r_O are the radii of respective ions. For the substituted perovskite at A and B site, $A_{1-x}A'_xB_{1-y}B'_yO_{3-\delta}$, r_A and r_B were calcuated from the sum of each metal at A site and B site, respectively, time its compostition. The atomic weight, ionic charge, coordination number, and ionic radius of all concerned metals were shown in Table A.1
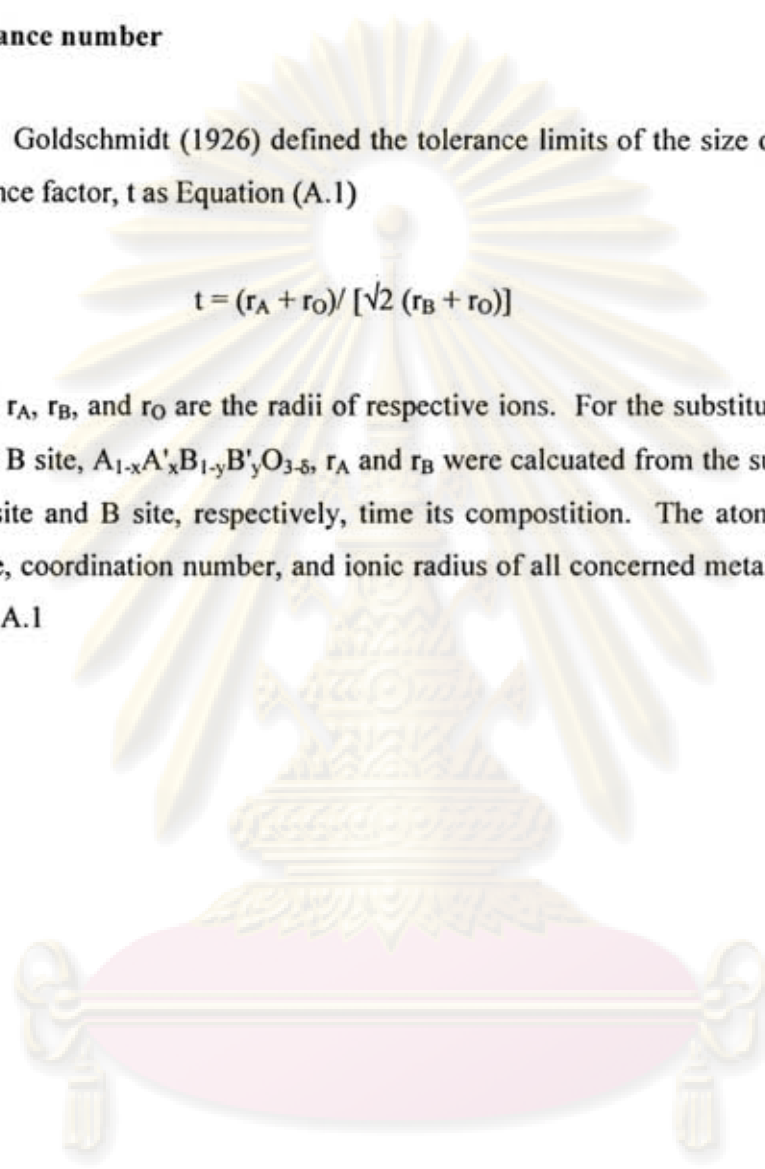
Table A.1 Atomic weight, ionic charge, coordination number, and ionic radius of concerned metals [55].

Ion	Ionic charge	Coordination No.	Ionic radius(Å)
Pr	3+	9	1.319
Ni	2+	6	0.830
Ni	3+	6	0.700
Ni	4+	6	0.620
Cu	1+	6	0.910
Cu	2+	6	0.870
Cu	3+	6	0.680
Co	2+	6	0.890
Co	3+	6	0.750
Co	4+	6	0.670
Zn	2+	6	0.880
In	3+	6	0.940
Mg	2+	6	0.860
Ga	3+	6	0.760
O	2-	6	1.260

Therefore, as Equation A.1 the tolerance number of perovskite compounds such as $Pr_2Ni_{0.9}Cu_{0.1}O_4$ was calculated as below.

$$\text{Tolerance number of } Pr_2Ni_{0.9}Cu_{0.1}O_4 = \frac{(1.319 \times 1) + 1.260}{\sqrt{2}\,[(0.83 \times 0.9) + (0.87 \times 0.9) + 1.260]}$$

$$= 0.871$$

APPENDICE B

Activation Energy (E_a)

Arrhenius plot of $Pr_2Ni_{0.7}Cu_{0.3}O_4$ is given in Figure B.1. The linear part can be described by the small polaron conduction mechanism, following the formula:

$$\sigma = (A/T) \exp(-Ea/kT) \qquad (B.1)$$

$$\sigma T = A \exp(-Ea/kT)$$

$$\ln \sigma T = -Ea/kT + \ln A \qquad (B.2)$$

A is material constant including the carrier concentration term,

Ea the activation energy

k the Boltzmann's constant

T is the absolute temperature.

From Equation B.2 Arrhenius plot of $\ln \sigma T$ versus $1000/T$ gives a straight line, whose slope and intercept can be used to determine E_a and A.
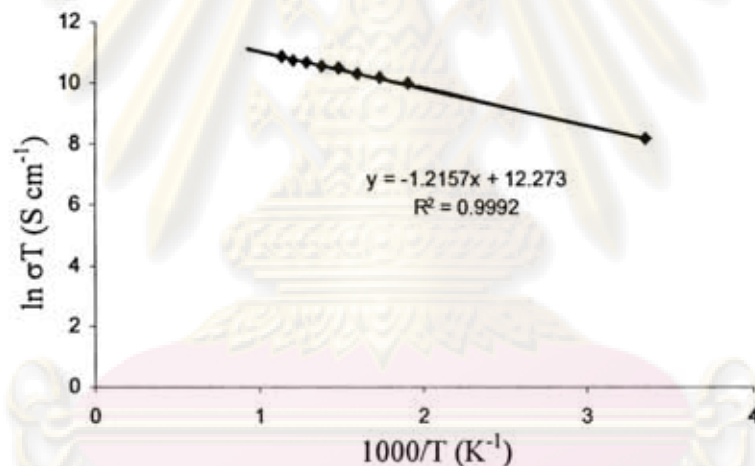
Figure B.1 Arrhenius plot of the electrical conductivity of $Pr_2Ni_{0.7}Cu_{0.3}O_4$.

The activation energy calculated from the slope of the straight line of figure B.1 For example, the activation energy (Ea) of $Pr_2Ni_{0.7}Cu_{0.3}O_4$, was calculated as below:

$$\text{Slope} = -Ea/k$$

$$\text{Slope} = -Ea/8.314472$$

$$Ea = -\text{slope} \times 8.314472$$

$$Ea = -(-1.2157) \times 8.314472$$

$$Ea = 10.11 \text{ kJ/mol}$$

APPENDICE C
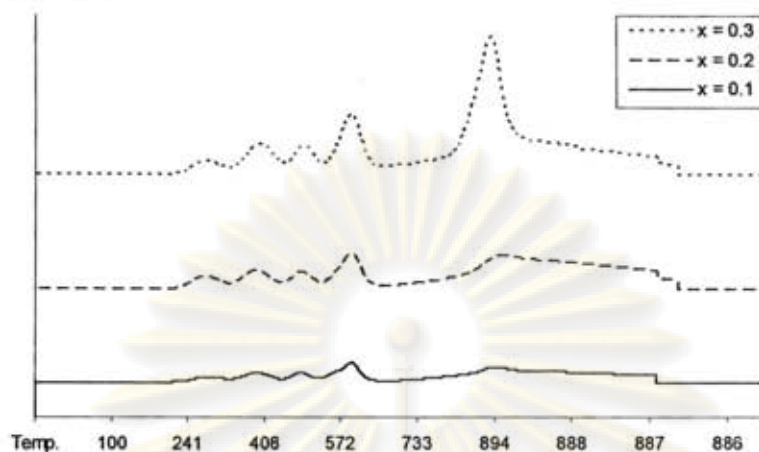
Figure C.1 O_2-TPD chromatogram of $Pr_2Ni_{1-x}Co_xO_4$ (x=0.1, 0.2, 0.3).
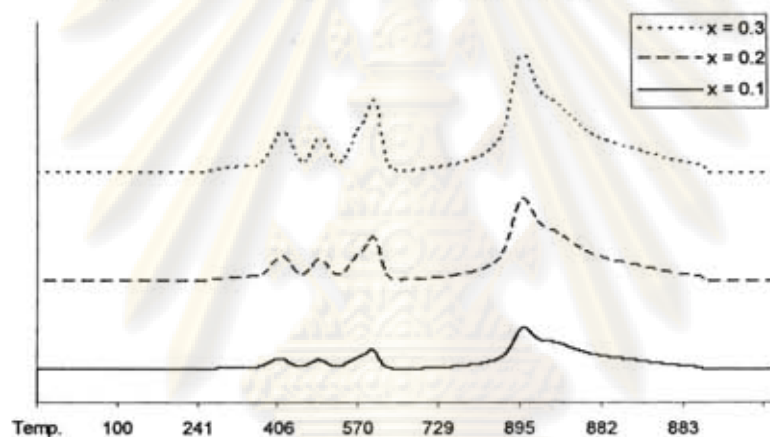
Figure C.2 O_2-TPD chromatogram of $Pr_2Ni_{1-x}Zn_xO_4$ (x=0.1, 0.2, 0.3).
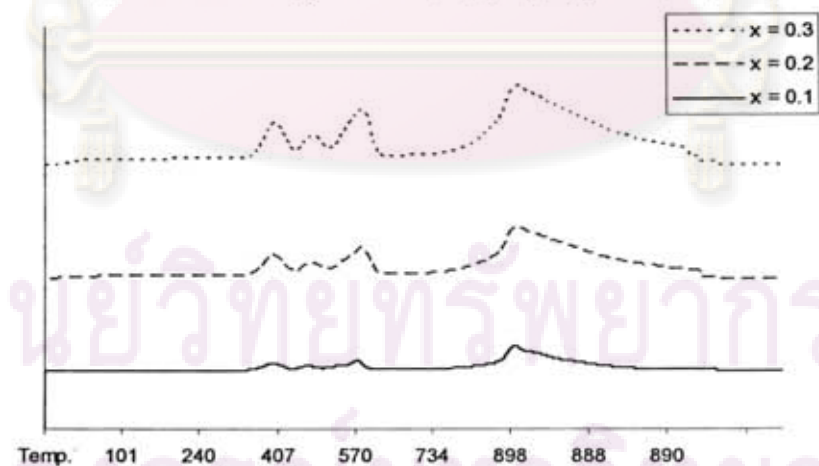
Figure C.3 O_2-TPD chromatogram of $Pr_2Ni_{1-x}In_xO_4$ (x=0.1, 0.2, 0.3).
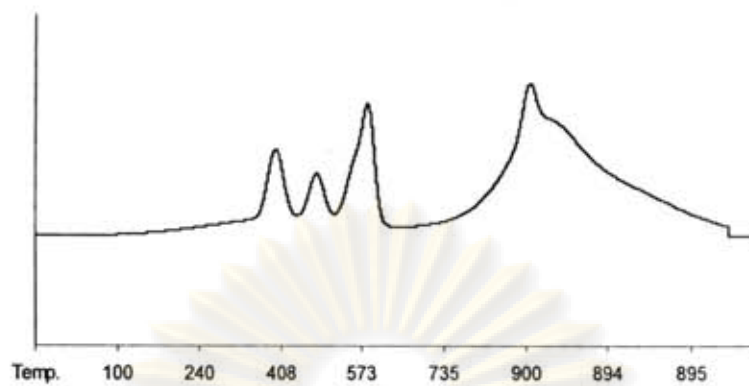
Figure C.4 O_2-TPD chromatogram of $Pr_2Ni_{0.9}Mg_{0.1}O_4$.
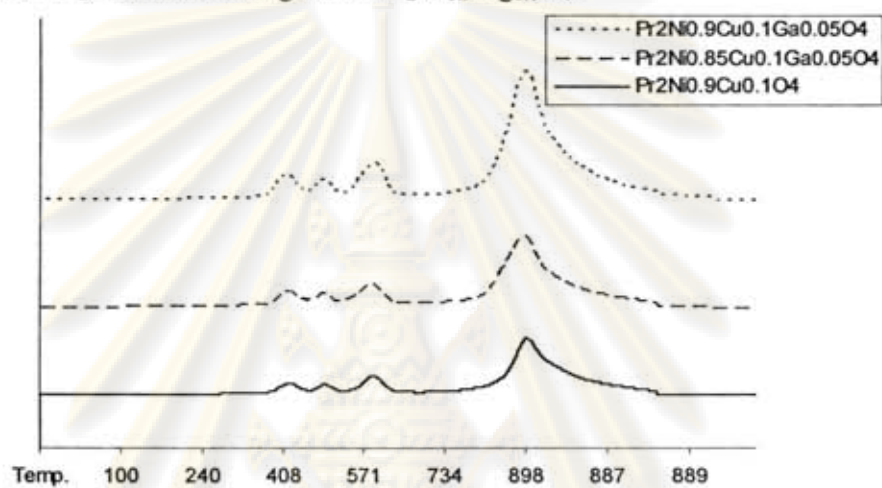
Figure C.5 O_2-TPD chromatogram of $Pr_2Ni_{0.9}Cu_{0.1}O_4$, $Pr_2Ni_{0.85}Cu_{0.1}Ga_{0.05}O_4$ and $Pr_2Ni_{0.9}Cu_{0.1}Ga_{0.05}O_4$.
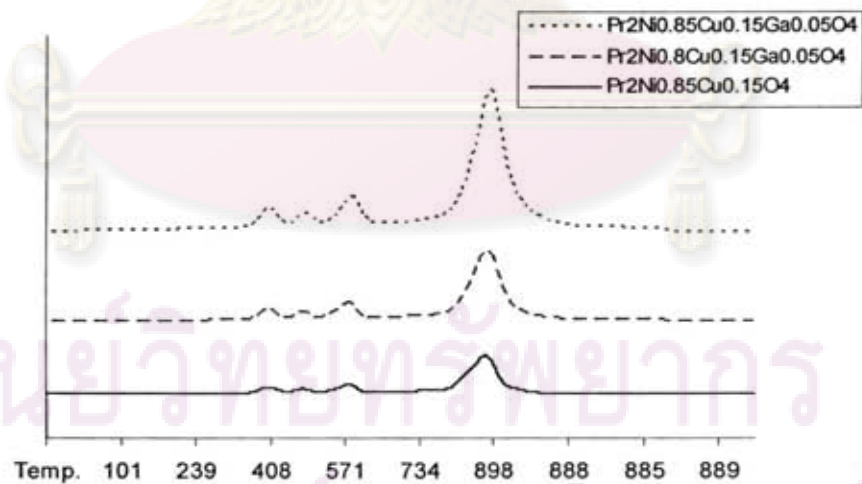
Figure C.6 O_2-TPD chromatogram of $Pr_2Ni_{0.85}Cu_{0.15}O_4$, $Pr_2Ni_{0.8}Cu_{0.15}Ga_{0.05}O_4$ and $Pr_2Ni_{0.85}Cu_{0.15}Ga_{0.05}O_4$.

Temp. 102 241 407 572 733 895 887 887
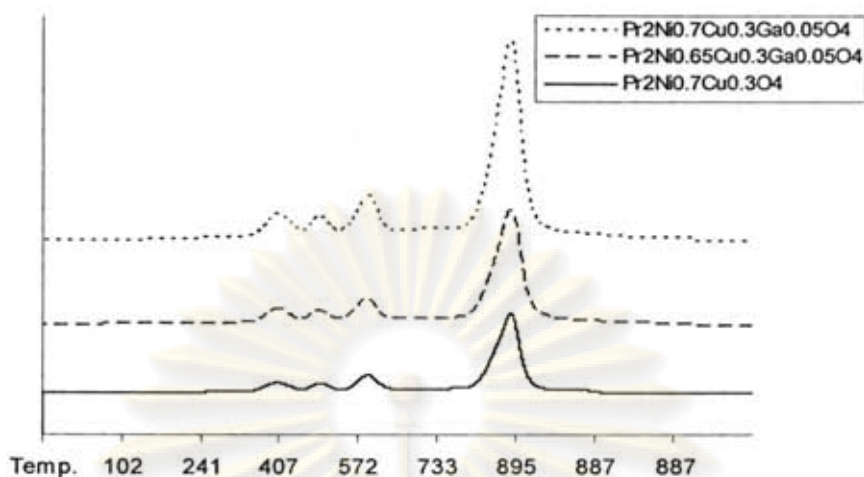
Figure C.7 O_2-TPD chromatogram of $Pr_2Ni_{0.7}Cu_{0.3}O_4$, $Pr_2Ni_{0.65}Cu_{0.3}Ga_{0.05}O_4$ and $Pr_2Ni_{0.7}Cu_{0.3}Ga_{0.05}O_4$.

Temp. 99 239 407 569 730 896 885 883 884
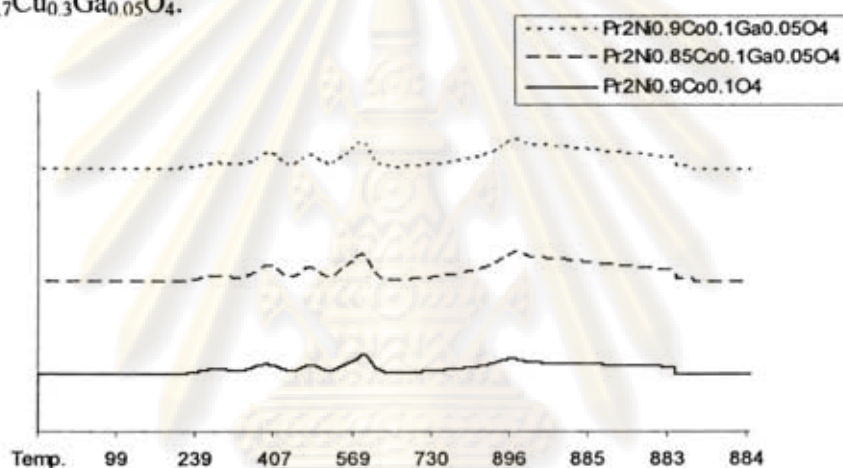
Figure C.8 O_2-TPD chromatogram of $Pr_2Ni_{0.9}Co_{0.1}O_4$, $Pr_2Ni_{0.85}Co_{0.1}Ga_{0.05}O_4$ and $Pr_2Ni_{0.9}Co_{0.1}Ga_{0.05}O_4$.

Temp. 100 241 408 572 733 897 884 886
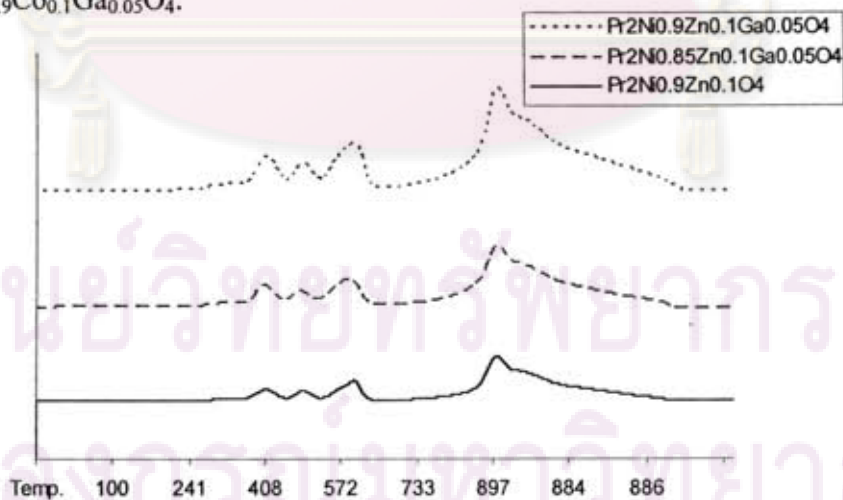
Figure C.9 O_2-TPD chromatogram of $Pr_2Ni_{0.9}Zn_{0.1}O_4$, $Pr_2Ni_{0.85}Zn_{0.1}Ga_{0.05}O_4$ and $Pr_2Ni_{0.9}Zn_{0.1}Ga_{0.05}O_4$.
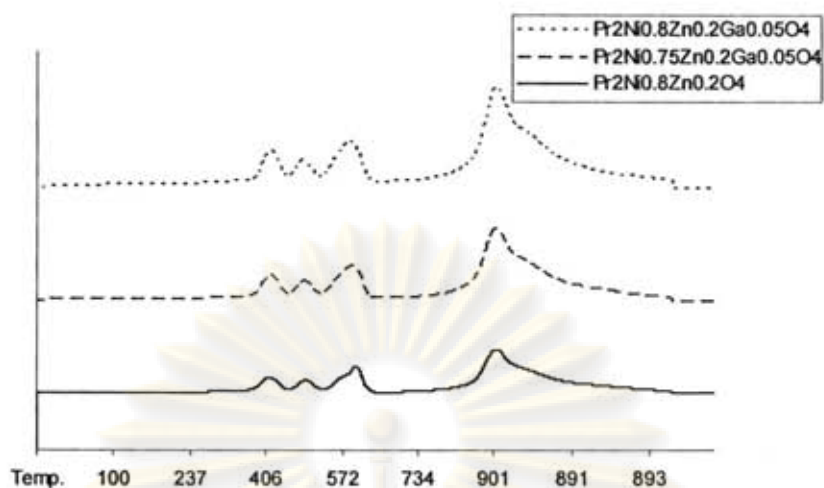
Figure C.10 O_2-TPD chromatogram of $Pr_2Ni_{0.8}Zn_{0.2}O_4$, $Pr_2Ni_{0.75}Zn_{0.2}Ga_{0.05}O_4$ and $Pr_2Ni_{0.8}Zn_{0.2}Ga_{0.05}O_4$.
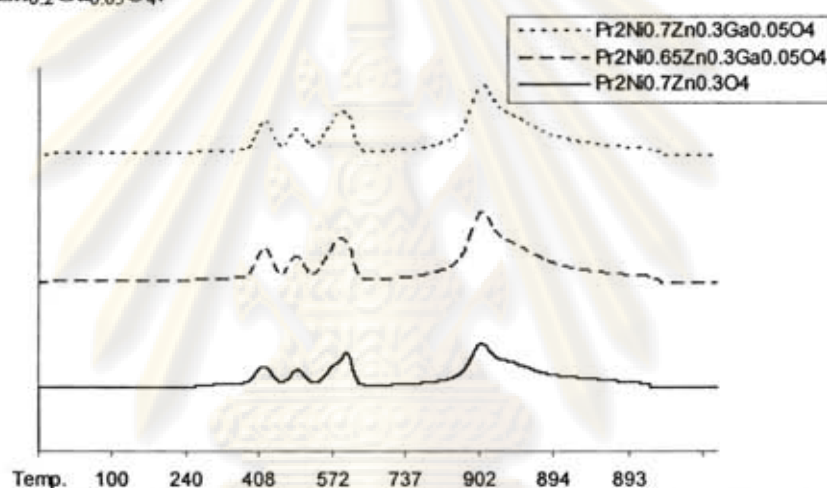
Figure C.11 O_2-TPD chromatogram of $Pr_2Ni_{0.7}Zn_{0.3}O_4$, $Pr_2Ni_{0.65}Zn_{0.3}Ga_{0.05}O_4$ and $Pr_2Ni_{0.7}Zn_{0.3}Ga_{0.05}O_4$.
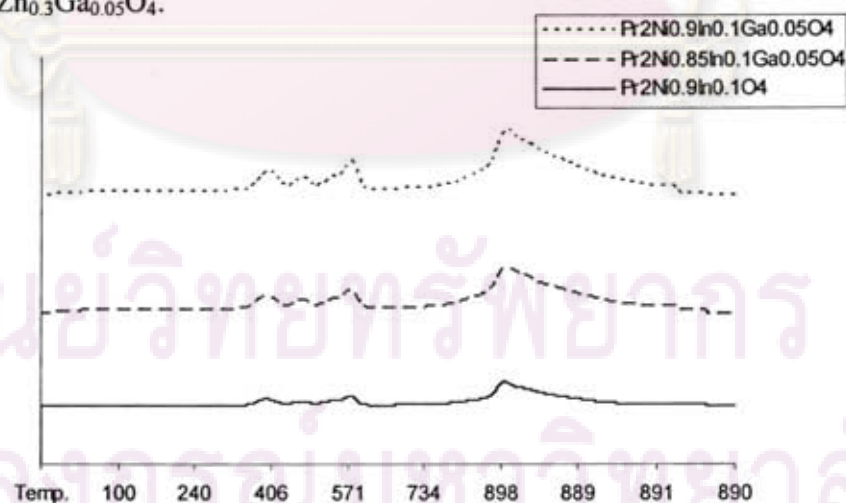
Figure C.12 O_2-TPD chromatogram of $Pr_2Ni_{0.9}In_{0.1}O_4$, $Pr_2Ni_{0.85}In_{0.1}Ga_{0.05}O_4$ and $Pr_2Ni_{0.9}In_{0.1}Ga_{0.05}O_4$.
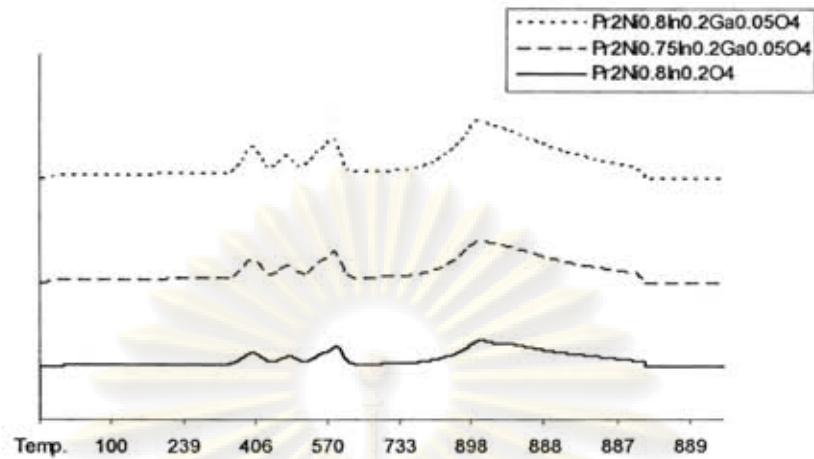
Figure C.13 O_2-TPD chromatogram of $Pr_2Ni_{0.8}In_{0.2}O_4$, $Pr_2Ni_{0.75}In_{0.2}Ga_{0.05}O_4$ and $Pr_2Ni_{0.8}In_{0.2}Ga_{0.05}O_4$.
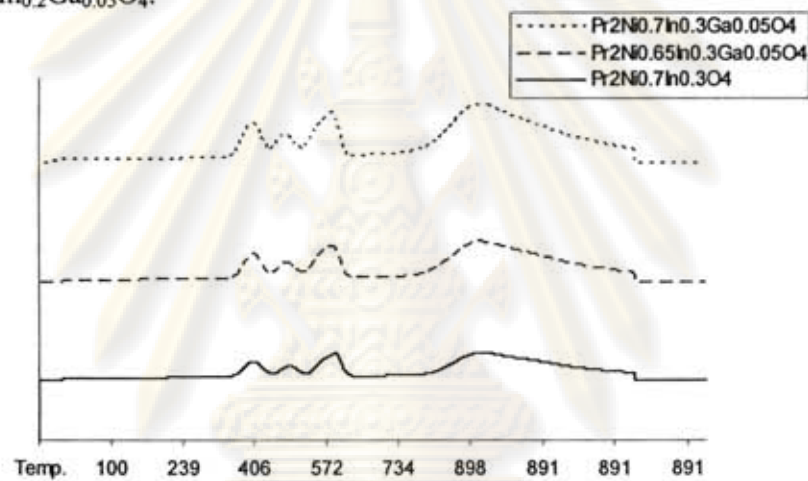
Figure C.14 O_2-TPD chromatogram of $Pr_2Ni_{0.7}In_{0.3}O_4$, $Pr_2Ni_{0.65}In_{0.3}Ga_{0.05}O_4$ and $Pr_2Ni_{0.7}In_{0.3}Ga_{0.05}O_4$.
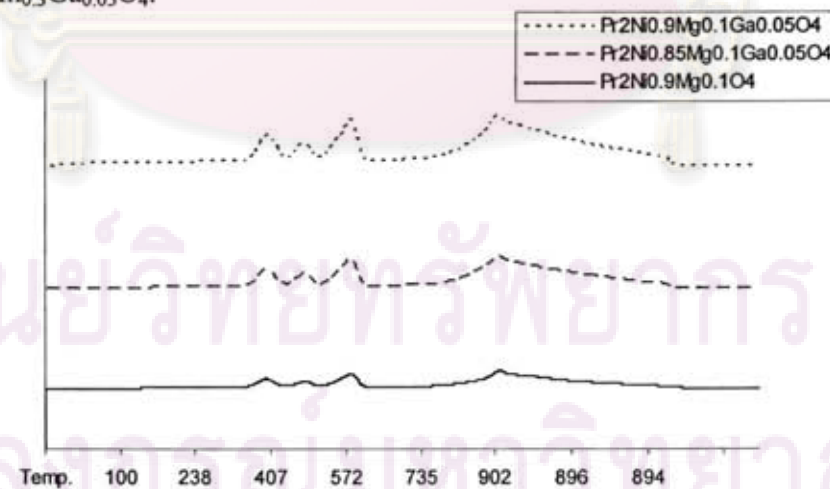
Figure C.15 O_2-TPD chromatogram of $Pr_2Ni_{0.9}Mg_{0.1}O_4$, $Pr_2Ni_{0.85}Mg_{0.1}Ga_{0.05}O_4$ and $Pr_2Ni_{0.9}Mg_{0.1}Ga_{0.05}O_4$.

APPENDICE D
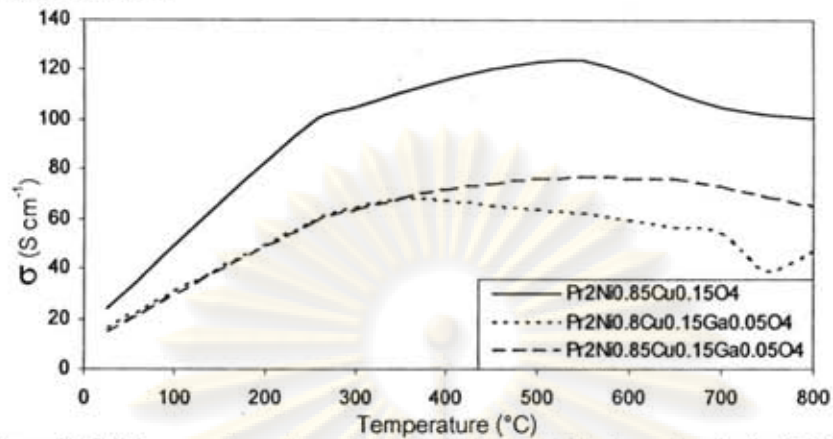
Figure D.1 Temperature dependence of the electrical conductivity (σ) for $Pr_2Ni_{0.85}Cu_{0.15}O_4$, $Pr_2Ni_{0.8}Cu_{0.15}Ga_{0.05}O_4$ and $Pr_2Ni_{0.85}Cu_{0.15}Ga_{0.05}O_4$.
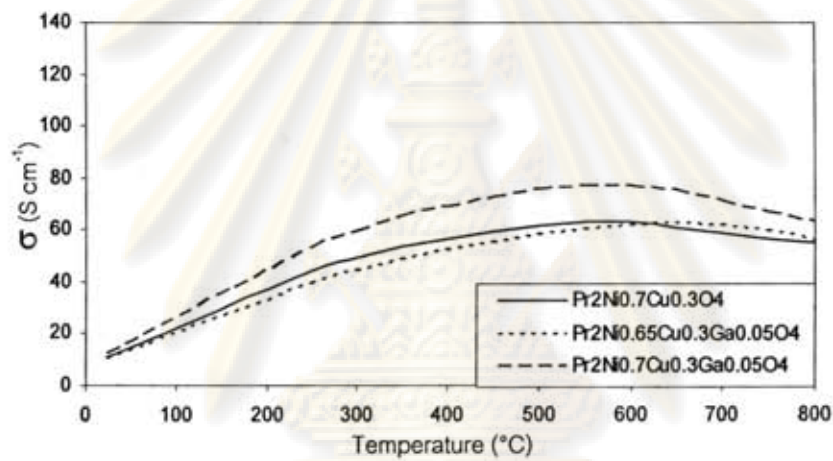
Figure D.2 Temperature dependence of the electrical conductivity (σ) for $Pr_2Ni_{0.7}Cu_{0.3}O_4$, $Pr_2Ni_{0.65}Cu_{0.3}Ga_{0.05}O_4$ and $Pr_2Ni_{0.7}Cu_{0.3}Ga_{0.05}O_4$.
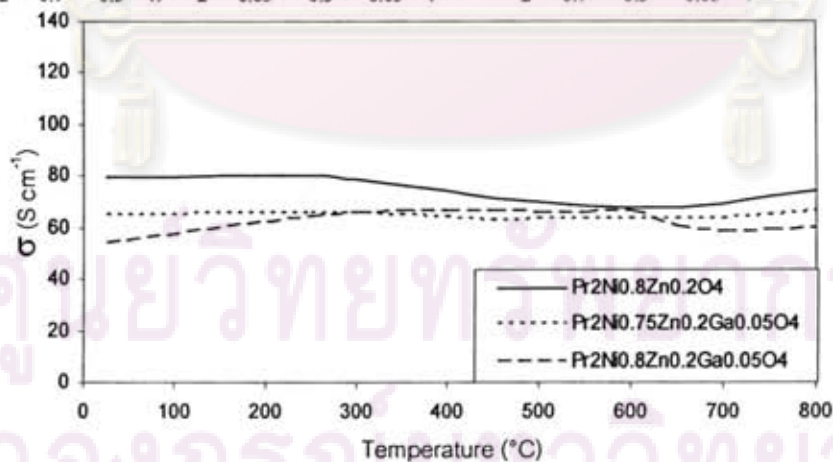
Figure D.3 Temperature dependence of the electrical conductivity (σ) for $Pr_2Ni_{0.8}Zn_{0.2}O_4$, $Pr_2Ni_{0.75}Zn_{0.2}Ga_{0.05}O_4$ and $Pr_2Ni_{0.8}Zn_{0.2}Ga_{0.05}O_4$.
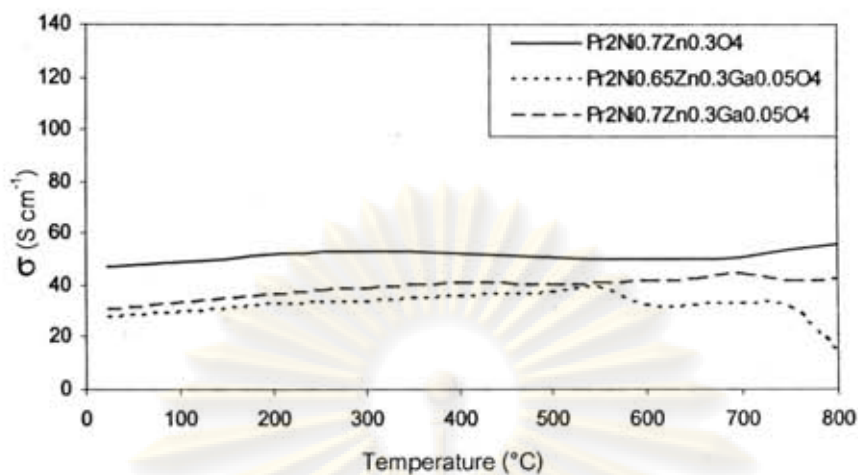
Figure D.4 Temperature dependence of the electrical conductivity (σ) for $Pr_2Ni_{0.7}Zn_{0.3}O_4$, $Pr_2Ni_{0.65}Zn_{0.3}Ga_{0.05}O_4$ and $Pr_2Ni_{0.7}Zn_{0.3}Ga_{0.05}O_4$.

VITA

Miss Siraprapa Thaitaworn was born on August 27, 1983 in Udontani, Thailand. She graduated with Bachelor's Degree in Chemistry from Faculty of Science, Kasetsart University in 2005. She continued her study in Petrochemistry and Polymer Science Program, Faculty of Science, Chulalongkorn University in 2005 and completed in 2008.

Her present address is 11/199 Soi Chulakasem 18, Ngamwongwan, Bangken, and Bangkok, Thailand 11000.